

# Influencing the microstructure of polycrystalline materials by magnetic fields

A phase field crystal approach

Dissertation

zur Erlangung des akademischen Grades

Doctor rerum naturalium

(Dr. rer. nat.)

vorgelegt

dem Bereich Mathematik und Naturwissenschaften

der Technischen Universität Dresden

von

Rainer Backofen

geboren am 1. September 1969 in Nürnberg

Eingereicht am 14. Oktober 2021

Die Dissertation wurde in der Zeit von Januar/2014 bis Oktober/2021 im  
Institut für Wissenschaftliches Rechnen angefertigt.



# Abstract

The ability to use external magnetic fields to influence the microstructure in polycrystalline materials has potential applications in microstructural engineering. To explore this potential and to understand the complex interactions between electromagnetic fields and solid-state matter transport we consider a phase-field-crystal (PFC) model that captures the basic physics of magnetocrystalline interactions. After investigations of a PFC model to study grain growth without an external magnetic field, the thesis concentrates on the influence of magnetic fields in the PFC model, to understand the basic phenomena. The second part considers a coarse graining of the PFC model towards an amplitude expansion (APFC) model to enable 3D simulations. The coupling with magnetic fields allows together with efficient and scalable numerical algorithms to examine the role of external magnetic fields on the evolution of defect structures and grain boundaries, on diffusion time scales. Large scale simulations in 2D and 3D also allow to obtain statistical data on grain growth under the influence of external fields and to validate with experimental data.





# Kurzfassung

Die Möglichkeit externe Magnetfelder zu nutzen um die Mikrostruktur in polykristallinen Materialien zu beeinflussen, hat potentielle Anwendungen in der Mikrostrukturierung. Um dieses Potential zu nutzen und die komplexen Interaktionen zwischen elektromagnetischen Feldern und Stofftransport in kondensierter Materie zu verstehen, wird ein Phasenfeldkristall(PFC)-Modell verwendet, welches die wesentlichen physikalischen Gesetzmäßigkeiten der magnetokristallinen Interaktionen berücksichtigt. Nach der Untersuchung des PFC Modelles zur Modellierung von Kornwachstum ohne externes Magnetfeld, konzentriert sich die Dissertation auf den Einfluß eines Magnetfeldes in dem PFC Modell, um die grundlegenden Phänomene zu verstehen. Der zweite Teil behandelt ein vergrößertes Modell der PFC Modelles, die Amplituden Gleichungen (APFC), welche auch 3D Simulationen ermöglichen. Die Kopplung mit Magnetfeldern erlaubt mittels effizienter und skalierbarer numerischer Algorithmen die Rolle von Magnetfeldern auf die Entwicklung von defektbehafteten Strukturen und Korngrenzen auf diffusiven Zeitskalen zu untersuchen. Großskalige Simulationen in 2D und 3D erlauben außerdem statistische Daten über Kornwachstum unter dem Einfluß externer Magnetfelder zu erhalten und die Simulationsergebnisse mit experimentellen Daten zu validieren.



# Acknowledgment

I gratefully acknowledge the funding of my thesis provided by the Institute of Scientific Computing at TU Dresden and the SPP 1959 project of the German Research Foundation (DFG). I would also thank the Centre for Information Services and High Performance Computing at TU Dresden and the Jülich Supercomputing Centre for providing the high performance cluster infrastructures, which I have extensively used for the simulations of this thesis.



# Statement on previously published results

To a large extent this thesis contains material which has been published already. Chapters 1 - 4 are taken from [6, 7, 9, 70] with small modifications to unify the notation and avoid redundancy. Other contributions of the author to the broader field of the thesis are [8, 10–14, 69, 70, 77]. These results are not discussed in detail in the thesis. In most of these papers the author is the corresponding author. Chapter 5 has not been published before. It introduces a new extended magnetic coupling and extends work from [69, 70] to the magnetic case.



# Contents

<b>1</b>	<b>Introduction</b>	<b>1</b>
1.1	Grain growth . . . . .	1
1.2	Atomistic modeling on diffusive time scales . . . . .	3
1.2.1	Phase field crystal model . . . . .	3
1.2.2	Amplitude expansion . . . . .	3
<b>2</b>	<b>Modeling grain growth</b>	<b>5</b>
2.1	Atomic considerations . . . . .	5
2.2	Phase field crystal model . . . . .	6
2.3	Results . . . . .	7
2.3.1	Scaling results . . . . .	8
2.3.2	Grain-size distribution . . . . .	8
2.4	Conclusions . . . . .	11
<b>3</b>	<b>Controlling grain boundaries by magnetic fields</b>	<b>13</b>
3.1	Influence of magnetic fields . . . . .	13
3.2	Modeling . . . . .	14
3.2.1	Coupled equations . . . . .	14
3.2.2	Model properties . . . . .	16
3.3	Simulation . . . . .	20
3.3.1	Coarsening . . . . .	20
3.3.2	Single grain . . . . .	22
3.3.3	Planar grain boundary . . . . .	22
3.4	Conclusion . . . . .	24
<b>4</b>	<b>Magnetically induced/enhanced coarsening in thin films</b>	<b>27</b>
4.1	Model and numerical approach . . . . .	27

4.2	Coarsening . . . . .	29
4.2.1	Scaling . . . . .	29
4.2.2	Orientation selection . . . . .	30
4.2.3	Grain size distribution . . . . .	33
4.2.4	Grain coordination and shape . . . . .	34
4.3	Discussion . . . . .	35
4.4	Conclusion . . . . .	37
<b>5</b>	<b>Controlling magnetic anisotropy in PFC</b>	<b>39</b>
5.1	Introduction . . . . .	39
5.2	Amplitude expansion of PFC (APFC) . . . . .	41
5.3	Magneto-structural coupling and minimum energy surface (MES)	48
5.4	Magneto-structural interaction in magnetic PFC . . . . .	53
5.4.1	Basic model of magnetic coupling . . . . .	53
5.4.2	Extended model . . . . .	65
5.4.3	Summary . . . . .	70
5.5	Magneto-structural coupling in APFC . . . . .	72
5.6	Summary . . . . .	77
<b>6</b>	<b>Conclusion</b>	<b>79</b>
	<b>References</b>	<b>81</b>



# 1 Introduction

## 1.1 Grain growth

Most metals, ceramics and minerals are polycrystalline materials containing grains of different crystal orientation. The size, shapes and arrangements of these grains strongly affect macroscale material properties, such as fracture, yield stress, coercivity and conductivity. In magnetic systems, for example, the coercivity (or magnetic 'hardness') can change by four or five orders of magnitude with a change in grain size [45]. Thus, understanding and controlling polycrystalline structures is of great importance in the production of many engineering materials and has motivated numerous experimental and theoretical studies of grain growth.

Grain growth in thin metallic films is one example where extensive research has been conducted. One very interesting experimental finding in such systems is that the grain size distributions and topological characteristics appear to be independent of many experimental conditions [15]. More specifically, it has been found that for a large collection of Al and Cu thin films a universal grain size distribution emerges that is independent of the substrate, annealing temperature, purity, thickness and annealing time. Unfortunately the universal distribution is qualitatively and quantitatively different from the results of extensive computational studies on grain growth, e.g. [33], which are based on the original Mullins model [59]. In this model the problem is reduced to the evolution of a two-dimensional grain boundary network by relating the normal velocity  $v_n$  to the curvature  $\kappa$  of the grain boundary,  $v_n = M\gamma\kappa$ , with mobility  $M$  and surface tension  $\gamma$ , and specifying the Herring condition [44] at triple junctions. Various attempts have been made to extend the original Mullins model and to include more realistic effects, such as interactions of the film with the substrate,

anisotropy in the grain boundary energy and mobility, grain boundary grooving, and solute and triple junction drag, see [15] and the references therein. While these extensions have in some cases been shown to significantly alter the grain statistics no single cause has been able to explain all experimental measured quantities as discussed in [15]. This discrepancy raises the question if the underlying picture of an evolving smooth grain boundary network of the Mullins curvature driven models is maybe oversimplified.

In addition to the grain size distribution, the rate of growth of the average grain size has also been examined in detail. The original Mullins model and its extensions all seem to predict that the average grain size, represented by its radius  $r(t)$  has a power law behavior of the form  $\sim t^{1/2}$ , which follows immediately from the linear relationship between grain boundary velocity and curvature. Experimentally a much slower coarsening or even stagnation of grain growth in thin films is observed. This may be due to the fact that the original Mullins model and its extensions ignore the crystalline structure of the grains, the dissipation due to lattice deformations and the Peierls barriers for dislocation motion. It is difficult to reconcile Mullins type models with the atomistic features of grain boundaries, which (for low angles) can be seen as an alignment of dislocations where the driving force for grain growth is the stress associated with dislocation motion. The differences of the description are shown schematically in Fig. 1.1.

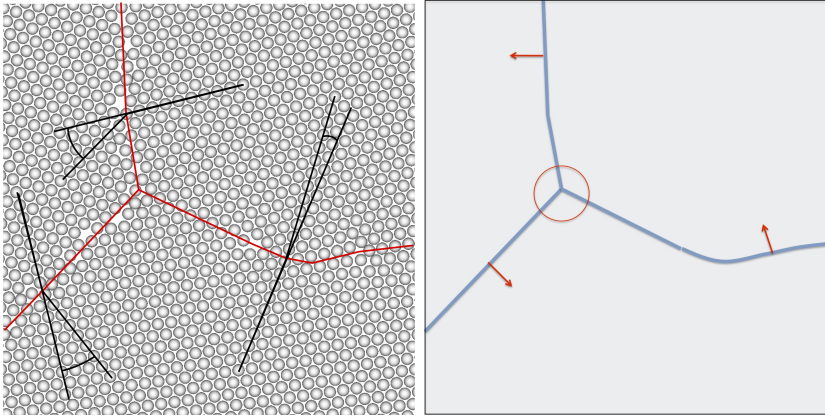


Figure 1.1: Schematic comparison between atomistic description of polycrystalline material and coarse grained picture of a smooth grain boundary network. Shown is a low angle grain boundary with aligned dislocations and two high angle grain boundaries in an otherwise hexagonal lattice.

## 1.2 Atomistic modeling on diffusive time scales

### 1.2.1 Phase field crystal model

A phase field crystal (PFC) model [30, 31], which considers the essential atomic details but operates on diffusive time scales, was able to reproduce the universal grain size distribution and showed similar scaling properties and stagnation as in the experiments [6], which will be discussed in Chapter 2. With the achieved agreement for various geometrical and topological properties it is time to use the PFC model as a predictive tool to control grain growth in thin films under the influence of external fields.

External magnetic fields during processing influence grain growth and as such have been proposed as an additional degree of freedom to control the grain structure, see [40, 66] for reviews. The PFC model has been extended to include magnetic interactions in [35, 72] and was used in [7] to explain the complex interactions between magnetic fields and solid-state matter transport. These results are explained in Chapter 3 in detail. An applied magnetic field influences the texture during coarsening due to the anisotropic magnetic properties of the single grains. Grains with their easy axis aligned to the external field are energetically preferred. They grow preferably at the expense of the other grains. The mobility of grain boundaries in this model is found to be anisotropic with respect to the applied magnetic field. Magnetostriction is naturally included in the extended PFC model. All these effects already change texture on small time scales. In [9] the long time scaling behavior and various geometrical and topological properties in grain growth under the influence of a strong external magnetic field are analysed. This is described in detail in Chapter 4.

### 1.2.2 Amplitude expansion

To overcome the length scale limitation of PFC models, the amplitude expansion, also referred to as renormalization-group reduction, of the PFC model (APFC) [4, 5, 37, 38] was developed. It is based on the idea that the continuous density in PFC models can be described by the amplitude of the minimum set of Fourier modes or wave vectors needed for a given crystal symmetry. To

allow for crystals in arbitrary orientations, strained systems, and/or defects, the amplitudes are complex functions. Roughly speaking, the magnitude of the amplitudes accounts for the liquid and solid phases, while the phase incorporates elasticity and crystal rotations. The combination of the magnitude and phase allows for defects. In this approach, a coarser spatial resolution than standard PFC can be used, thus allowing for the simulation of much larger systems. Simulations of the APFC model have been shown to be very useful for studying a wide variety of phenomena. The method has been applied to the study of polycrystalline films and the motion of grain boundaries (GBs) [5, 37, 38, 88], the study of heteroepitaxial ordering of ultrathin films [28, 29], structural phase transitions [60], and grain-boundary energies in graphene [46]. While the original APFC model was introduced for twodimensional systems with triangular symmetry, the method has been extended to fcc and bcc systems in three dimensions [26, 27]. Most of these investigations were performed with simulations using simple numerical methods on a fixed grid. Improvements on the numerics, i.e., an adaptive finite-element method (FEM) with a semi-implicit integration scheme has been introduced in [63, 70]. In Chapter 5 we will extend this approach to study the influence of magnetic fields.

## 2 | Modeling grain growth

This chapter is taken from [6]. Modifications are only made to unify notation and avoid redundancy.

### 2.1 Atomic considerations

Atomistic descriptions can incorporate the important physical features missing in the Mullins type models and have led to some important observations. It has been shown that the complex dislocation structure along curved grain boundaries gives rise to a misorientation-dependent mobility [83]. Further studies indicate that grain boundaries undergo thermal roughening associated with an abrupt mobility change, leading to smooth (fast) and rough (slow) boundaries [47], which can eventually lead to stagnation of the growth process. The defect structure at triple junctions can lead to a sufficiently small mobility limiting the rate of grain boundary migration [74, 81]. Also tangential motion of the lattices are possible. For low-angle grain boundaries, normal and tangential motion are strongly coupled as a result of the geometric constraint that the lattices of two crystals change continuously across the interface while the grain boundary moves [23]. As a consequence of this coupling, grains rotate as they shrink which leads to an increase in the grain boundary energy per unit length, although the overall energy decreases since the size of the boundary decreases [73, 79, 80]. Each of these phenomena can be simulated using molecular dynamics (MD), see [52] for a review. However, to study the effect of these phenomena on scaling laws, grain size distributions or stagnation of growth requires a method which operates on diffusive time scales. For this reason we choose to study the phase field crystal model (PFC) which incorporates atomistic details on diffusive time scales.

## 2.2 Phase field crystal model

The phase field crystal (PFC) method [31] was introduced to model elasticity, dislocations and grain boundaries in polycrystalline systems in a simple and natural fashion. The model has been shown to successfully model grain boundary energies as a function of misorientation [48] and non-classical grain rotation during grain shrinkage and drag of triple junctions [85]. In addition lower coarsening exponents were already observed for hexagonal lattices [1, 22, 61] and even stagnation of grain growth could be seen [21]. The aim of this paper is to use the PFC model on large scales to obtain statistical data for grain size distributions and to compare them with prior experimental data for thin metallic films. Since the experimental results in [15] seem to be universal, we do not fit the PFC parameters to a specific material but consider an artificial setting within the simplest PFC model introduced in [31]. In dimensionless form the equation reads

$$\frac{\partial \varphi}{\partial t} = \Gamma \nabla^2 \frac{\delta \mathcal{F}}{\delta \varphi}, \quad (2.1)$$

where the order parameter  $\varphi$ , is related to the time-averaged atomic density,  $t$  is time,  $\Gamma$  is the mobility and  $\mathcal{F}$  is the free energy given by,

$$\mathcal{F} = \int \varphi (-\epsilon + (\nabla^2 + 1)^2) \frac{\varphi}{2} + \frac{\varphi^4}{4} dr. \quad (2.2)$$

where  $\epsilon$  is a parameter related to temperature. The free energy functional is constructed so that in the liquid state it is minimized by  $\varphi = \text{constant}$  and in the solid crystalline state by a periodic function that has triangular symmetry in two dimensions and a dimensionless lattice constant  $4\pi/\sqrt{3}$ . The precise phase diagram can be found in reference [31] and a small portion is shown in Fig. 2.2. In the crystalline state  $\mathcal{F}$  is minimized by a periodic function of arbitrary orientation, making the model ideal for the study of polycrystalline materials. Elasticity is naturally incorporated in this model as any deviation from the equilibrium triangular structure increases the energy. The specific elastic constants are controlled by the average density of  $\varphi$ ,  $\bar{\varphi}$ , and  $\epsilon$  and can be written  $C_{12} = C_{44} = C_{11}/3$ , where  $C_{12} = [(3\bar{\varphi} + \sqrt{15\epsilon - 36\bar{\varphi}^2})/75]$ . This model and the parameters that enter it can be related to more fundamental approaches

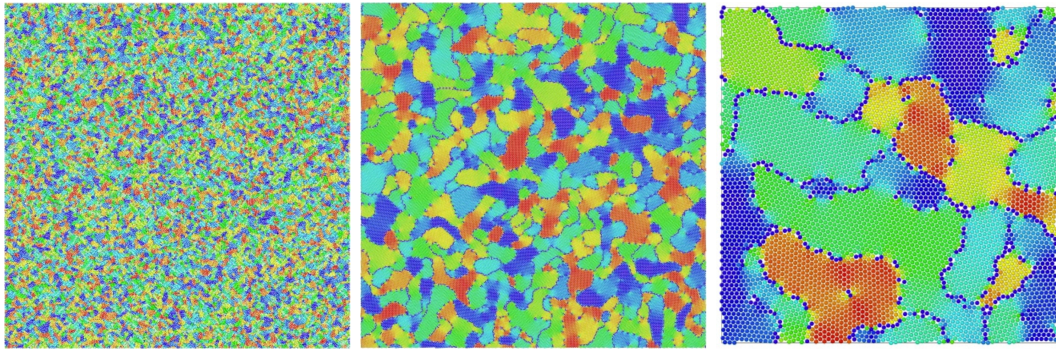


Figure 2.1: Grain structure obtained from postprocessing a PFC simulation at an intermediate time. The color coding indicates the averaged local lattice orientation for each of the maxima in the density field. An enlargement by a factor of four is used for each figure. Animations of the grain growth process for the three enlargements are provided in the supplementary materials of [6], as movie 1-3, corresponding to case "A1" in Fig. 2.2.

such as classical dynamic density functional theory (DDFT) [32, 48, 77, 84].

## 2.3 Results

Fig. 2.1 shows a snapshot of a typical simulation, the corresponding animations of the growth process are shown in the supplementary material of [6], as movie 1-3. The movies allows to identify all mentioned effect resulting from the atomistic description, in particular fast and slow moving grain boundaries, pinned triple junctions, rotating grains, elastic deformations within single grains and the movement of isolated dislocations.

All simulations are performed in a periodic domain of square size  $L = 8,192$  starting from a randomly perturbed constant value of the particle density  $\varphi$ . After an initiation phase in which the white noise is damped rapidly, grains nucleate, grow and impinge on one another. Thereafter the number of maxima in the particle density  $\varphi$  remains mainly constant and coarsening starts. Statistical results are collected after grains have reached a minimal size of 100 atoms.

### 2.3.1 Scaling results

Fig. 2.2 shows the obtained scaling results for the average domain area as a power law in times, i.e.,  $t^q$ , where  $q$  is  $1/2$  in the Mullins type curvature driven models. In our simulations it is not clear that this relationship is valid as the value of  $q$  can be seen to change in time and be dependent on the parameters of the simulation and initial conditions. For case "A", we either obtain an initial value of  $q = 1/3$ , which turns into  $q = 1/5$ , or a constant value of  $q = 1/5$ , depending on the initial grain size. The constant scaling exponent is observed for larger initial grains. For case "B", corresponding to a softer material, the growth exponent increases to a value of  $q = 2/5$ , whereas for case "C", a harder material it decreases to  $q = 1/20$ . For all three cases, the growth exponent is significantly lower than the expected value  $q = 1/2$  for the Mullins type models. Similar low coarsening exponents have been found for hexagonal lattices in [22, 61] and in experiments for thin films of CoPt and FePt [65]. Extensive computational studies in [1, 61] further show a strong dependency of the scaling exponent on additional noise, which enhances the coarsening process. It has also been noted [1] that the addition of higher order time derivatives can change the growth exponent, which may be appropriate for three-dimensional samples. In two-dimensional thin films (i.e., films with columnar grain structures), however, it is expected that the substrate/film coupling provides an effective friction for rotation or translation that eliminates the need for such corrections. In either case, it is likely that the growth exponents are transient, because for very large grain sizes the Peierls-Nabarro barriers are likely to inhibit further coarsening. This effect already occurs at early times for quenches to lower temperatures, as confirmed for points in the phase diagram in the solid region at  $(\varphi_0, \epsilon) = (-0.31, -0.25)$ , and  $(\varphi_0, \epsilon) = (-0.29, -0.18)$ , which show a frozen configuration.

### 2.3.2 Grain-size distribution

While it is not entirely clear if there is a single, well-established dynamical exponent, the grain size distribution functions appear to be much more robust. Fig. 2.3 shows the averaged grain size distribution of the PFC simulations for the considered points in the phase diagram, together with the experimental results



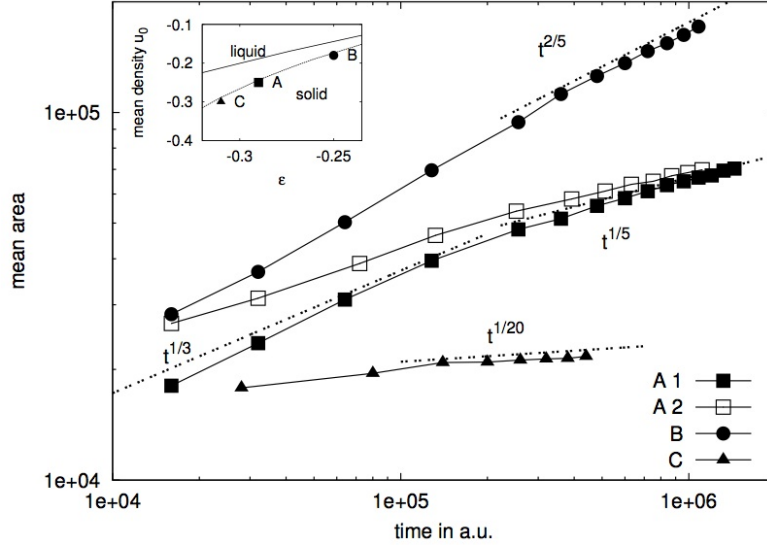


Figure 2.2: Mean area as a function of time together with the fitted scaling exponents for various points in the phase diagram depicted in the inset. "A1" and "A2" have different initial grain sizes ( $A1 < A2$ ), the parameters are "A":  $(\varphi_0, \epsilon) = (-0.29, -0.25)$ ; "B":  $(\varphi_0, \epsilon) = (-0.25, -0.18)$ ; "C":  $(\varphi_0, \epsilon) = (-0.31, -0.30)$ .

and the results of the Mullins type model taken from [15].

A considerable discrepancy between the experimental results and the Mullins type models is already discussed in [15, 16]. They differ in two important respects. First, the experimental grain structures have a larger number of small grains as evidenced by the peak of the experimental reduced area probability density residing to the left of that for the simulations based on the Mullins type models, a feature that has been termed the "ear". Second, the experimental grain structures have "tails" that extend to significantly larger sizes than those seen in simulations based on the Mullins type models. While only very few grains seen in simulations exceed 4 times (and only rarely do they exceed 5 times) the mean area, the experimental grain structures exhibit maximum grain areas that are between 8 and 42 times the mean, with a sizable fraction of grains whose areas exceed 4 times the mean grain area ( $\sim 3\%$  by number, representing  $\sim 18\%$  of the total area). Various closed form distributions have been proposed to fit the results of the Mullins type models, e.g. the Louat, Hillert, Rios and Weibull distribution (see [33] and the references therein). They all not only differ

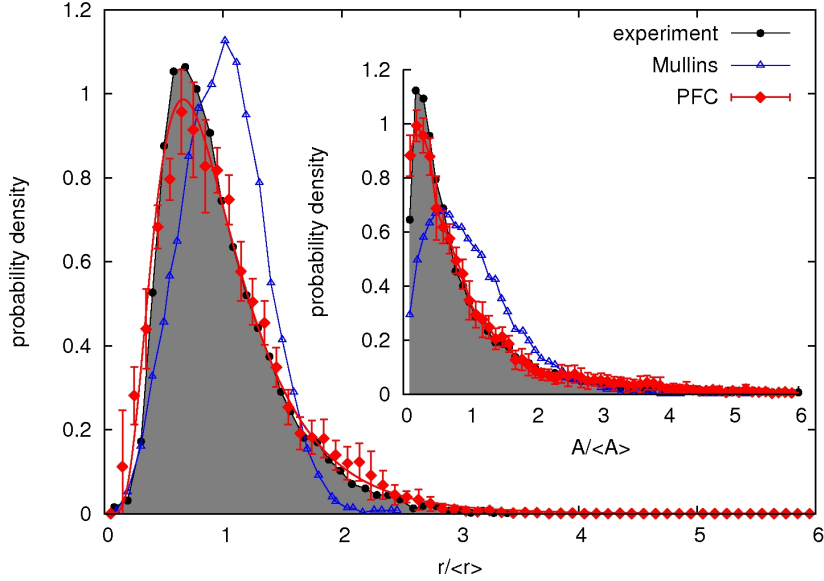


Figure 2.3: Grain size distribution with reference to radius (area in inlet). Shown is the mean distribution, obtained as the average of the last time steps for cases "A1", "A2" and "B" in Fig. 2.2. Case "C" was not included as it still may contain remnants of the initial condition. The curve is fitted to a lognormal distribution with parameters  $(\mu, \sigma) = (-0.13, 0.53)$ . The experimental data and the results of the Mullins model are taken from [15]

in the "ear" and "tail" region, but they also peak at  $r/\langle r \rangle > 1$ , again in disagreement with the experimental results. The PFC simulations not only recover the qualitative behaviour of the experimental results, they almost perfectly fit the distribution, and can be very well described by a log-normal distribution. The grain size distribution appears to be self-similar which is analysed in detail for case "A1" in Fig. 2.4. All results are obtained without additional noise. However, simulations that included noise (not shown) produced grain distributions consistent with the zero noise case. Further analysis indicates that, also in agreement with the experimental data, small grains are primarily 3 and 4-sided, whereas large grains have primarily more than 6 sides.

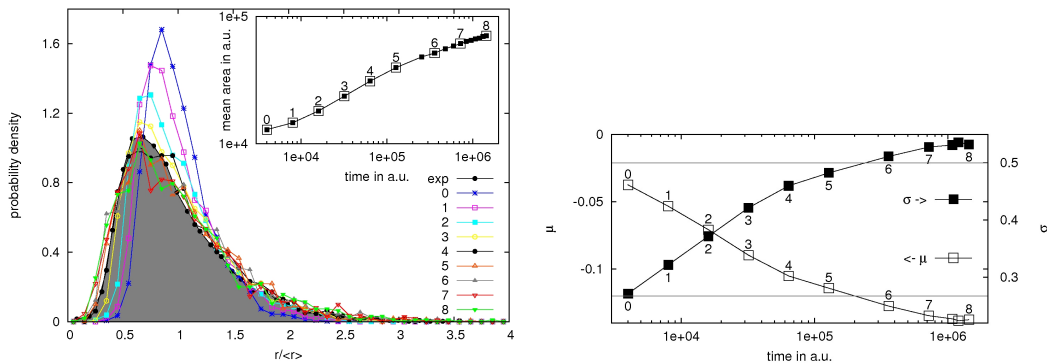


Figure 2.4: top) Grain size distribution with reference to radius at the labeled times in the inlet, coresponding to case "A1" in Fig. 2.2 in comparison with the experimental results from [15]. We choose the case with a "fast" coarsening rate, to rule out any dependency on the initial conditions. The evolution for case "A2", "B" and "C" are similar. The initially narrow distribution broadens rapidly and its peak shifts towards smaller grains. For large times the grain size distribution appears to be self-similar which is further illustrated in (bottom) showing the time evolution of the parameters  $\sigma$  and  $\mu$  of a log-normal distribution fitted to the considered snapshots, again in comparison with the experimental results from [15] shown as the horizontal solid lines.

## 2.4 Conclusions

The importance and prevalence of the formation and properties of polycrystalline materials has lead to an enormous amount of theoretical and experimental research. Unfortunately theoretical progress has been hindered by the lack of computational methods that can capture the essential physics on the time and lengths that are appropriate for such phenomena. While MD simulations are currently unable to reach time scales required to observe self-similar growth regimes, coarse grained descriptions based on the Mullins model seem to lack the essential atomistic features allowing for bulk dissipation during grain growth. In this work large scale numerical simulations of the PFC model were used to examine the phenomenon of grain growth in two dimensional systems. The results of these simulations are in remarkable agreement with universal aspects of the geometric and topological characteristics of the grain structures in thin metallic films. Among other features they capture both the "ear" and "tail" characteristics of grain distributions that have proven difficult to obtain with previous

models and methods. Thus the PFC model provides a key resource for future research in which realistic grain structures are required. Although not examined in this work, the model also incorporates mechanical properties of the system and thus can be used to study, for example, the relationship between growth conditions and the structural stability of polycrystalline materials.

# 3 | Controlling grain boundaries by magnetic fields

This chapter is taken from [7]. Modifications are only made to unify notation and avoid redundancy.

## 3.1 Influence of magnetic fields

The use of external magnetic fields offers additional degrees of freedom to synthesize materials and to tailor the grain structure and thus material properties. Although evidence for the interactions between external magnetic fields, diffusion and irreversible deformation mechanisms have been gathered over the years, see the review [40], a global yet detailed understanding of the interactions between magnetic fields and solid-state matter transport is far from being reached. In this Letter we analyze the properties of a theoretical model, which allows the description of the basic physics of magnetocrystalline interactions in a multiscale approach, combining the dynamics of defects, dislocation networks and grain boundaries with experimentally accessible microstructure evolution on diffusive time scales.

The basic mechanisms of this interaction can be understood on thermodynamic arguments. In magnetic materials the magnetic moments are aligned with a sufficiently strong external magnetic field. If the magnetic properties of the material are anisotropic, the bulk free energy differs for differently oriented grains and the energy difference can influence grain boundary (GB) movement.

The dynamics of the GB can be described by Mullins-type models [59]

$$v = -M(\gamma\kappa - \Delta f) \quad (3.1)$$

extended by the bulk energy difference [3, 76], where  $v$  is the normal velocity of the GB,  $M$  a mobility function,  $\kappa$  the mean curvature and  $\Delta f$  the energy density difference of the grains. Assuming two differently oriented grains in a strong magnetic field in a circular and planar setting, see SI for details, the total energy of the system and (3.1) lead to a critical grain size  $r_c = -\gamma/\Delta f$  in the circular and a constant  $v \propto \Delta f$  in the planar setting. Both cases demonstrate the possibility to influence GB movement by external magnetic fields. However, the description ignores the underlying crystalline lattice which can influence the process.

It has been shown that the complex dislocation structure along curved GB gives rise to a misorientation-dependent mobility [83]. Further studies indicate that grain boundaries undergo thermal roughening associated with an abrupt mobility change, leading to smooth (fast) and rough (slow) boundaries [47], which can eventually lead to stagnation of the growth process. The defect structure at triple junctions can lead to a sufficiently small mobility limiting the rate of GB migration [74, 81]. Also, tangential motion of the lattices is possible. For low-angle GB, normal and tangential motion are strongly coupled as a result of the geometric constraint that the lattices of two crystals change continuously across the interface while the GB moves [23]. As a consequence of this coupling, grains rotate as they shrink, which leads to an increase in the GB energy per unit length, although the overall energy decreases since the size of the boundary decreases [43, 73, 79, 80, 85].

## 3.2 Modeling

### 3.2.1 Coupled equations

The phase field crystal (PFC) model [30–32, 77], captures all these complex features and numerical simulations of the model have been shown to recover the

characteristic grain size distribution in agreement with detailed experimental results [6]. Numerous publications have shown the model to capture the essential physics of atomic-scale elastic and plastic effects that accompany diffusive phase transformations, such as solidification, dislocation kinetics and solid-state precipitation, see [34] for a review.

In [35] the model is coupled with magnetization to generate a ferromagnetic solid below a density-dependent Curie temperature. In [72] this model is extended and used to demonstrate the influence of magnetic fields on the growth of crystal grains. These results indicate that a greater portion of grains evolve to become aligned along the easy direction of the crystal structure with respect to the orientation of the external magnetic field. In this Letter we use it to predict the influence of the magnetic field on grain coarsening in polycrystals. Consistent with the thermodynamic arguments we find that when the magnetic field is applied, the average grain size increases and the number of grain along the easy direction with respect to the field increases. However, it is also found that the grains become elongated when the field is applied. The elongation occurs due to an anisotropic GB mobility in the presence of an applied field.

The model in [35, 72] combines the rescaled number density  $\varphi$  with a mean field approximation for the averaged magnetization  $\mathbf{m}$ . The energy

$$\mathcal{F}[\varphi, \mathbf{m}] = \int f_{\text{PFC}}(\varphi) + \omega_B f_m(\mathbf{m}) + \omega_B f_c(\varphi, \mathbf{m}) \, \text{d}\mathbf{r} \quad (3.2)$$

with

$$\begin{aligned} f_{\text{PFC}}(\varphi) &= \frac{1}{2}\varphi(\mathbf{r})^2 - \frac{t}{6}\varphi(\mathbf{r})^3 + \frac{v}{12}\varphi(\mathbf{r})^4 \\ &\quad - \frac{1}{2}\varphi(\mathbf{r}) \int C_2(\mathbf{r} - \mathbf{r}')\varphi(\mathbf{r}') \, \text{d}\mathbf{r}' \\ f_m(\mathbf{m}) &= \frac{W_0^2}{2}(\nabla \cdot \mathbf{m})^2 + r_m \frac{\mathbf{m}^2}{2} + \gamma_m \frac{\mathbf{m}^4}{4} - \mathbf{m} \cdot \mathbf{B} + \frac{\mathbf{B}^2}{2} \\ f_c(\varphi, \mathbf{m}) &= -\omega_m \varphi^2 \frac{\mathbf{m}^2}{2} - \sum_{j=1}^2 \frac{\alpha_{2j}}{2j} (\mathbf{m} \cdot \nabla \varphi)^{2j}, \end{aligned} \quad (3.3)$$

consists of contributions related to local ordering of the crystal, to local orientation of the magnetic moment and to coupling between crystal structure and

magnetization.  $\omega_B$  is a parameter to control the influence of the magnetic energy. In order to maximize the anisotropy in the 2D setting, a square ordering of the crystal is preferred, which is realized within the XPFC formulation for  $f_{PFC}(\varphi)$ , see [39, 60].

Magnetization in an isotropic and homogenous material is modeled by  $f_m(\mathbf{m})$ . The first three terms define a mean field theory of a vector field which is minimized by  $\mathbf{m} = 0$  for  $r_m > 0$  and  $\mathbf{m} = -r_m/\gamma_m$  for  $r_m < 0$ . Thus, a negative  $r_m$  leads to ferromagnetic properties. The last two terms describe the interaction of the magnetization with an external and a self-induced magnetic field,  $\mathbf{B}_{ext}$  and  $\mathbf{B}_{ind}$ , respectively. The magnetic field is defined as  $\mathbf{B} = \mathbf{B}_{ext} + \mathbf{B}_{ind}$ , where  $\mathbf{B}_{ind}$  is defined with help of the vector potential:  $\mathbf{B}_{ind} = \nabla \times \mathbf{A}$  and  $\nabla^2 \mathbf{A} = -\nabla \times \mathbf{m}$ . The magnetic anisotropy of the material is due to the crystalline structure of the material. Thus, the magnetization has to depend on the local structure represented by  $\varphi$  and vice versa. The first term in  $f_c(\varphi, \mathbf{m})$ , changes the ferromagnetic transition in the magnetic free energy. On average  $\varphi^2$  is larger in the crystal than in the homogeneous phase. Thus,  $\omega_m$  and  $r_m$  can be chosen to realize a paramagnetic homogeneous phase and a ferromagnetic crystal. The second term depends on average on the relative orientation of the crystalline structure with respect to the magnetization. In our case, it lead to an energetic minimum if the magnetization is aligned with the diagonal of the square crystal. The number density  $\varphi$  evolve according to conserved dynamics and magnetization according to non-conserved dynamics,

$$\frac{\partial \varphi}{\partial t} = M_n \nabla^2 \frac{\delta \mathcal{F}[\varphi, \mathbf{m}]}{\delta \varphi}, \quad \frac{\partial m_i}{\partial t} = -M_m \frac{\delta \mathcal{F}[\varphi, \mathbf{m}]}{\delta m_i} \quad (3.4)$$

$i = 1, 2$ , respectively.

### 3.2.2 Model properties

To measure the magnetic anisotropy we consider a single crystal and vary  $\mathbf{B}_{ext}$ . The simulation domain perfectly fits the equilibrium crystal for  $\mathbf{B}_{ext} = 0$  and is small enough to prevent the appearance of magnetic domains. The parameters are chosen for a ferromagnetic material, see SI for details.



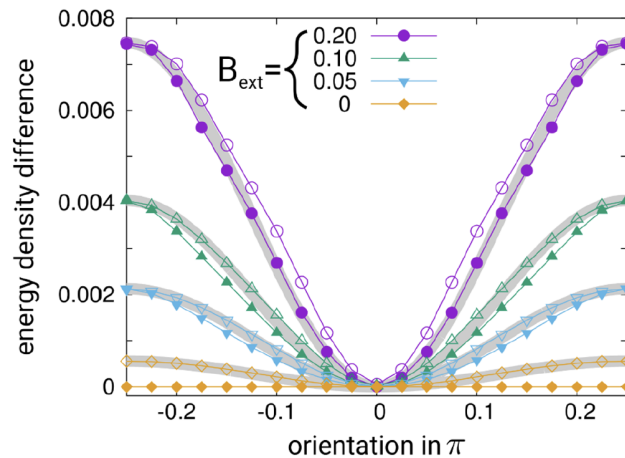


Figure 3.1: Energy density deviation in a single crystal induced by  $\mathbf{B}_{ext}$  and measured relative to a crystal preferably aligned with  $\mathbf{B}_{ext}$ . The orientation with respect to the crystal structure and strength of  $\mathbf{B}_{ext}$  is varied. Open symbols correspond to forced alignment of magnetic moments with  $\mathbf{B}_{ext}$ , closed symbols show computed magnetic moments, gray curves show fits by cosine-functions.

Fig. 3.1 shows the anisotropy of the bulk free energy with respect to the orientation of the magnetic moments with and without an external magnetic field. Restricting the magnetic moments to the direction of the external magnetic field, leads to slightly larger bulk energies for orientations not along hard and easy direction. This is due to the reduced degrees of freedom for energy minimization and shows that in the full model in these cases the magnetic moments are not perfectly aligned with  $\mathbf{B}_{ext}$ . However, the differences are small. The magnetic anisotropy for both cases follows the 4-fold symmetry of the crystal and the easy directions are along the  $\langle 11 \rangle$ -directions. Increasing  $\mathbf{B}_{ext}$  increases the anisotropy as well as the mean magnetization. The model also includes magnetostriction effects [35]. The crystal slightly tends to elongate along the easy direction aligned with  $\mathbf{B}_{ext}$ . Coupling local magnetization to the number density breaks the fourfold symmetry of the number density distribution. Aligning the magnetic moments along the easy direction of the crystal, the density tends to elongate along the direction of the magnetic field, see Fig. 3.2.

The elongation increases with the strength of magnetization. Thus, the fourfold symmetry of the crystal is broken by the magnetization induced by an external magnetic field. The symmetry breaking due to external magnetic fields also

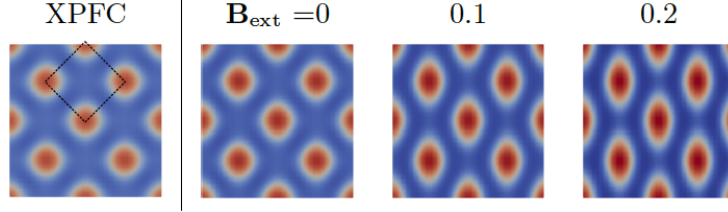


Figure 3.2: Density of square ordering. The XPFC model (left,  $\omega_B = 0$ ) is four fold symmetric. In the magnetic XPFC model of a ferromagnetic material the magnetization is aligned to a easy direction and the density peak becomes elongated in this direction ( $\mathbf{B}_{ext} = 0$ ).

influence the elastic response of single crystal. In Fig. 3.3 the energy density w.r.t to deformation of a single crystal is shown. The crystal is either compressed or stretched along the easy  $[1\ 1]$  directions. The easy direction is aligned to the external magnetic field. This leads to a deformed crystal. Due to the interaction with the magnetic moments, the crystal becomes softer along  $\mathbf{B}_{ext}$  and stiffer perpendicular to  $\mathbf{B}_{ext}$ . Thus, also the elastic properties are altered. A minimum of the energy density is found at an expansion of about 1% for  $B_0 = 0.1$ . This shows that the aligned crystal in our simulations introduces stress in the direction of the magnetic field and breaks the four fold symmetry. The effect increases with  $\mathbf{B}_{ext}$ , see Fig. 3.4.

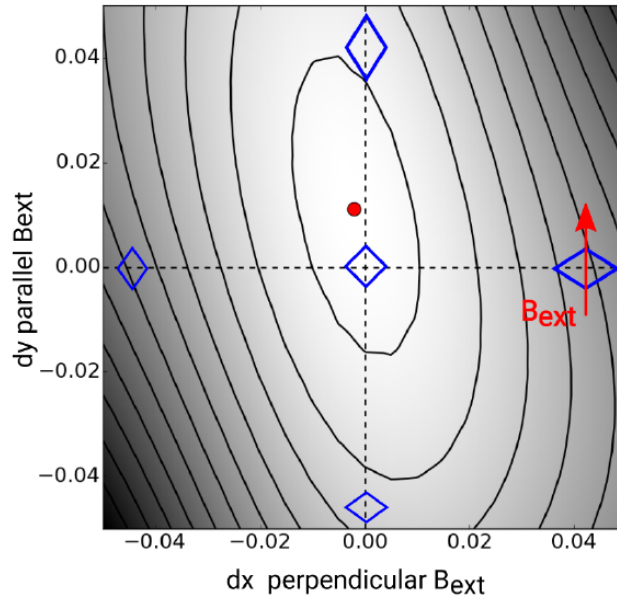


Figure 3.3: Energy density dependent on applied deformation of a single crystal. The deformation  $dx$  ( $dy$ ) is perpendicular (parallel) to  $\mathbf{B}_{ext}$  along a  $[11]$  direction. The blue shapes show the type of applied deformations. The circle indicate the minimum in the energy density. The crystal tends to elongate along  $\mathbf{B}_{ext}$ .

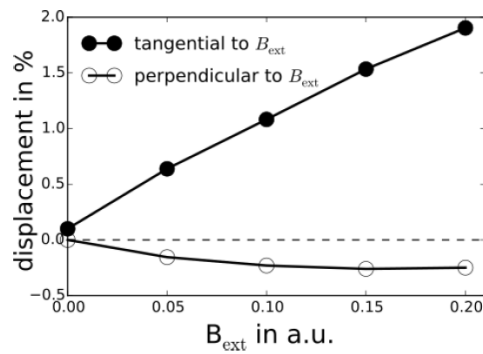


Figure 3.4: Deformation of minimum energy state dependent on  $\mathbf{B}_{ext}$ . With increasing  $\mathbf{B}_{ext}$  the crystal tends to elongate.

## 3.3 Simulation

### 3.3.1 Coarsening

To show the impact of external magnetic fields on the texture evolution during coarsening we prepared a polycrystalline sample, see Fig. 3.5. An initially randomly perturbed density field is evolved without magnetic interaction until the fine polycrystalline structure appears. Any particle with four neighbors is identified as a particle in a crystalline structure and the local orientation of the crystal with respect to the external magnetic field is calculated and visualized. Starting from this initial condition the evolution equations are solved with small random magnetization for different external magnetic fields, applied in x-direction. For  $B_{ext} = 0$  there is no energetically preferred orientation and coarsening is only due to minimization of GB energy. Small grains vanish and larger grains grow. The average grain size increases and the orientation distribution stays isotropic. Applying an external field leads to a preferred growth of grains which are aligned preferably with respect to the external magnetic field, the easy direction (green). Thus, the not aligned grains (blue and red) vanish and the orientation distribution peaks near the aligned grain orientation. This is in qualitative agreement with experiments, e.g. on Zn and Ti sheets [56], and classical grain growth simulations of Mullins type with an analytical magnetic driving force [17]. The additional driving force, due to the external magnetic field, also enhances the coarsening process, which can already be seen by comparing the final textures in Fig. 3.5 and which has also been observed experimentally, e.g. during annealing of FeCo under high steady magnetic fields [66]. Increasing  $\mathbf{B}_{ext}$  leads to more pronounced grain orientation selection.

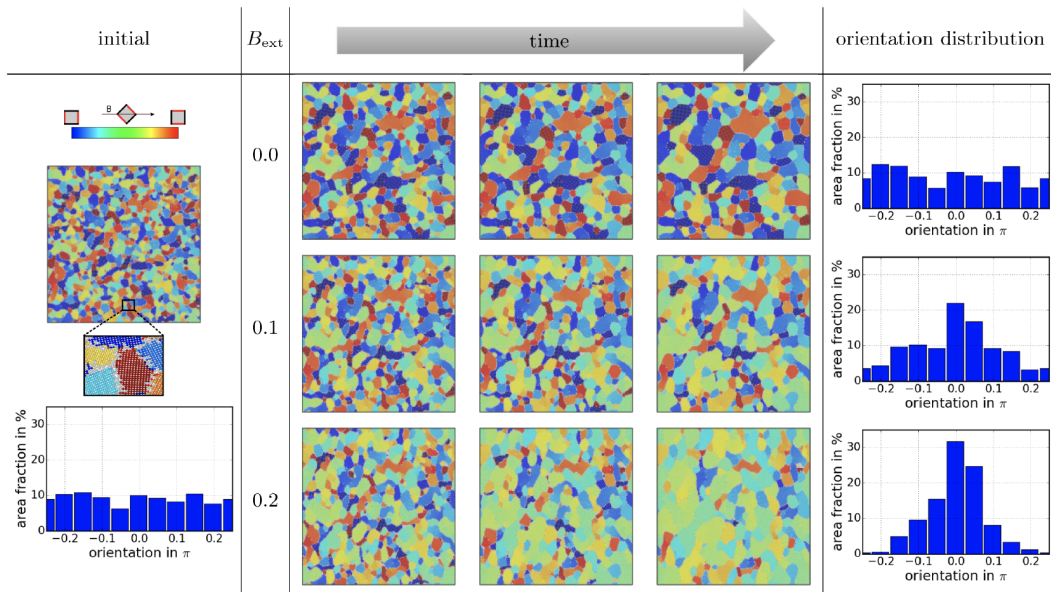


Figure 3.5: (left) Initial configuration for coarsening simulation. The color shows the local orientation of the crystal with respect to the external magnetic field. The direction of the external magnetic field is in x-direction and corresponds to grains oriented in the easy direction (green). For the inlet the maxima of  $\varphi$  are visualized as atoms. The orientation distribution is isotropic. (middle) Coarsening simulation for different  $B_{\text{ext}}$  (up-down) with snapshots in time (left-right). (right) Orientation distribution at final time of coarsening process. For the used parameters see Chapter 2. The computational domain is  $409.6 \times 409.6$ .

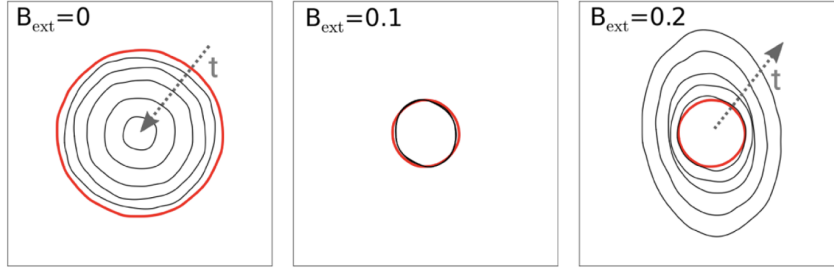


Figure 3.6: A circular grain embedded in a matrix (red isoline). The external magnetic field is aligned with the easy direction of the circular grain. Dependent on strength of  $\mathbf{B}_{ext}$  the grain shrinks, stagnates or grows.

### 3.3.2 Single grain

In order to analyze these results in more detail we consider the two settings of a circular and a planar GB. We start with a rotated crystal embedded in a matrix, see Fig. 3.6. For  $B_{ext} = 0$  the grain shrinks and vanishes in order to minimize GB energy.  $\mathbf{B}_{ext}$  aligned with the easy direction of the rotated grain induces an opposite driving force, which for  $B_{ext} = 0.1$  balances the GB energy, while increasing  $\mathbf{B}_{ext}$  above this threshold leads to growth of the grain. This is in accordance with the continuous description.

However, for  $B_{ext} = 0.2$  the evolution is anisotropic, first a square like shape is reached, resampling the 4-fold crystalline symmetry, while further growth breaks this symmetry, the grain becomes elongated perpendicular to  $\mathbf{B}_{ext}$ . This may be explained by thermodynamic or kinetic reasons [42, 71]. Within the continuous description of eq. (3.1) the shape reached for  $B_{ext} = 0.2$  requires either the GB energy  $\gamma$  parallel to  $\mathbf{B}_{ext}$  to be roughly twice the energy perpendicular to  $\mathbf{B}_{ext}$  or the mobility  $M$  of parallel and perpendicular GB has to vary by a factor of two or some combination of both.

### 3.3.3 Planar grain boundary

To separate thermodynamic ( $\gamma$ ) and kinetic effects ( $M$ ) of GB movement, we consider a planar GB. According to the continuum description the velocity of the planar GB is proportional to the driving force  $\Delta f$ . Thus, the decay of total energy is linear and the mobility can be extracted,  $M = -v/\Delta f$ . To maximize

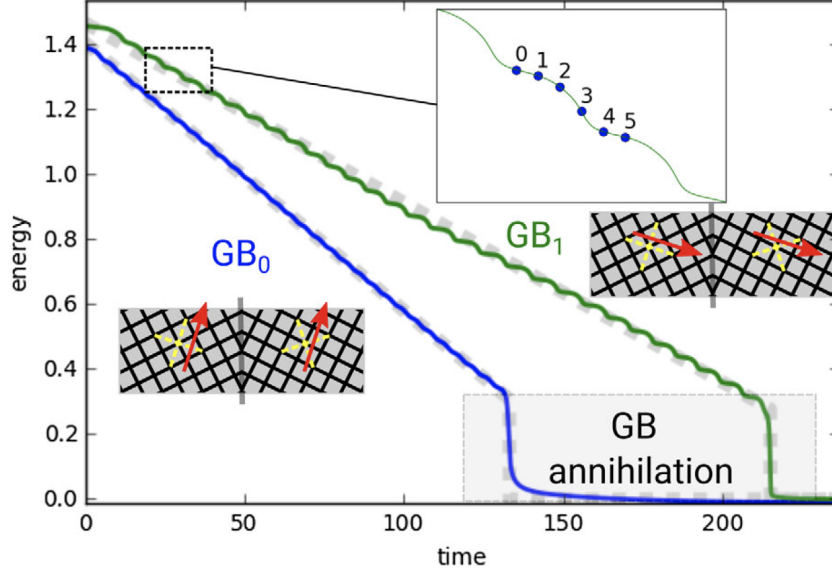


Figure 3.7: Two setups of a symmetric tilt GB in a periodic domain,  $B_{ext} = 0.1$  is aligned with the easy directions of the left grain. Both setups lead to the same driving force, but the energy decay differs.

the influence of  $\mathbf{B}_{ext}$  two symmetric high angle GB are placed in an elongated periodic domain.  $\mathbf{B}_{ext}$  is aligned with the easy direction of the left grain. Due to symmetry the magnetic field can be rotated by  $\pi/2$ . In one situation the magnetization is more aligned and in the other more perpendicular to the GB, see Fig. 3.7, which shows the setup and the energy decay for both situations.

The initial condition is achieved by a purely structural relaxation with  $\omega_B = 0$ . Then the coupling with  $\mathbf{B}_{ext}$  is switched on. After some initial reconfiguration, which adjusts the density field  $\varphi$ , the energy decays on average linearly. The GBs move with constant speed reducing the size of the grain not aligned with  $\mathbf{B}_{ext}$  until they vanish. The final annihilation of the GB leads to a sudden drop in energy, which is proportional to  $\gamma$  and equal in both cases. However, the energy decays faster in the case of a more aligned  $\mathbf{B}_{ext}$  with the GB, implying faster GB velocity and in turn a larger GB mobility.

A closer look at the energy decay shows a step like function. This reflects the crystalline structure of the GB. In order to move the GB by a unit length it has to pass some energetically unfavorable positions, see Fig. 3.8.

Varying the magnitude of  $\mathbf{B}_{ext}$  changes the driving force and the velocity of

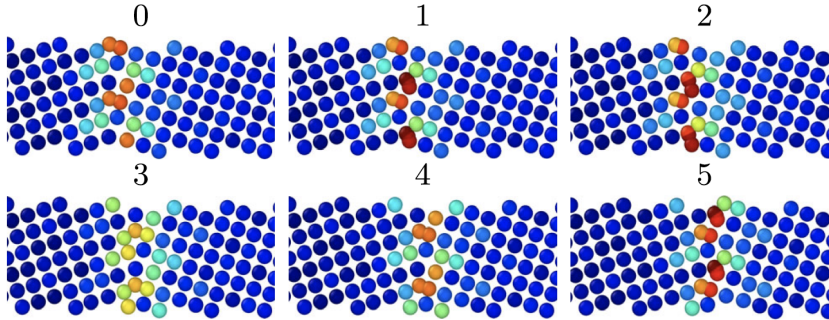


Figure 3.8: Particle picture of the GB during evolution over one unit length. The particles are located according to maxima in the density field  $\varphi$ . The color is the energy density at the position of the particle and serves as a measure of the local energy, see [50]. During the slow evolution (0-2) the energy of the particles at the GB increases until the energy barrier is overcome by the magnetic driving force leading to a speed up of the GB and a decrease of the energy at the GB (2-3), before the next barrier is reached (3-4) and the energy at the GB increases again (4-5).

the GB, see Fig. 3.9. For large driving forces the dependency of the velocity is linear for both cases but by a factor two smaller for the case of  $\mathbf{B}_{ext}$  more perpendicular to the GB. For a driving forces below a threshold the GB does not move, indicating the presence of an activation barrier, which has also been measured experimentally for planar GB in Zn bicrystals [41]. For intermediate regimes the mobility increases. As a consequence, the anisotropy seen in Fig. 3.6 can be attributed to kinetics and not thermodynamic effects, which was also claimed in [56] by interpreting the experiments on Zn and Ti.

### 3.4 Conclusion

In summary we have shown that an applied magnetic field can increase the coarsening rate in grain growth processes, due to the lower energy of grains with their easy axis in line with the applied field. We have also shown that the mobility of GB is anisotropic with respect to the applied magnetic field. This kinetic effect leads to elongated grains. Both of these influences are intimately related to the magnetically anisotropic nature of the model studied. That is,



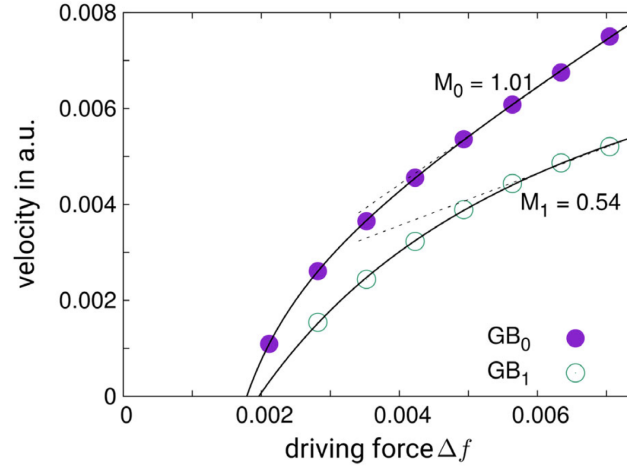


Figure 3.9: Velocity extracted for the setups defined in Fig. 3.7. For small external magnetic field the GB is pinned and does not move at all. High driving forces lead to a linear increase of velocity with  $\Delta f$  and an assumed mobility becomes constant. The mobility differs by a factor of two.

the crystal reacts elastically on applied magnetic fields (magnetostriction) and additionally changes in the density field reflecting the two fold symmetry of  $\mathbf{B}_{ext}$  may lead to preferred diffusion path and, thus, influence the mobility. It should be noted that the study examined the influence of an applied field on a ferromagnetic nano-crystalline system and did not examine the influence of magnetic field on the initial nucleation stage. This is left for future study.



# 4 | Magnetically induced/enhanced coarsening in thin films

This chapter is taken from [9]. Modifications are only made to unify notation and avoid redundancy.

## 4.1 Model and numerical approach

We consider the same model as in Chapter 3. However, in the limit of strong external magnetic fields,  $\mathbf{B}_{ext}$ , the magnetization,  $\mathbf{m}$ , can be assumed to be homogeneous in the crystal. As shown in [7] the magnetization becomes perfectly aligned with the external magnetic field and independent of the relative orientation of the crystal. For paramagnetic or ferromagnetic materials near the Curie temperature, the magnitude of the magnetization  $m = |\mathbf{m}|$  depends on the magnitude of the external magnetic field  $\mathbf{B}_{ext}$ . In this limit  $f_m(\mathbf{m})$  is constant and does not influence the dynamics. Furthermore, we are only concerned with the crystal phase and assume  $\omega_m = 0$ . The remaining parameters are chosen as in Table 4.1 and lead to a minimization of energy if the magnetization is aligned with the  $\langle 11 \rangle$ -directions of the crystal, the easy axis. The hard axis are the  $\langle 10 \rangle$ -directions. Thus, a preferably or perfectly aligned single crystal has a  $\langle 11 \rangle$ -direction aligned with the external magnetic field. Due to the direct relation between  $\mathbf{B}_{ext}$  and  $\mathbf{m}$ , only the evolution equation for  $\varphi$  remains and

t	v	$M_n$	$\bar{\varphi}$	$k_{0/1}$	$\xi_{1/2}$	$A_{0,1}$	$\omega_B$	$\alpha_{2,4}$
1	1	1	0.05	$(2\pi, \sqrt{2}2\pi)$	(1, 1)	(1, 1)	1	(-0.001, 0)

Table 4.1: Modeling parameters. The parameters are inspired by [60] and chosen to maximize the energetic difference between square and triangular phase.

reads:

$$\frac{\partial \varphi}{\partial t} = M_n \nabla^2 \left[ \varphi - \frac{t}{2} \varphi^2 + \frac{v}{3} \varphi^3 - \int C_2(\mathbf{r} - \mathbf{r}') \varphi(\mathbf{r}') d\mathbf{r}' + \omega_B \nabla \sum_{j=1}^2 \alpha_{2j} (\mathbf{m} \nabla \varphi)^{2j-1} \mathbf{m} \right], \quad (4.1)$$

where  $\mathbf{m}$  is considered as a parameter. Increasing  $\mathbf{m}$  leads to increasing anisotropy and magnetostriction [7]. The external magnetic field  $\mathbf{B}_{ext}$  and thus  $\mathbf{m}$  is assumed to be parallel to the thin film. Thus, in this limit of strong external magnetic fields we can use  $\mathbf{m}$  to vary the strength and direction of the influence of the external magnetic field on the thin film. The magnitude of  $\mathbf{m}$  is varied between  $[0; 0.8]$  and varies the magnetic anisotropy.

In order to increase numerical stability, short wavelength in the solutions of the density are gradually damped in k-space by adding  $-10^{-6}(2\mathbf{k}_1 - \mathbf{k})^2$  to  $C_k(\mathbf{k})$ . The evolution equation is solved semi-implicitly in time with a pseudo-spectral method. For numerical details we refer to [8, 64]. The reduced model eq. (4.1) is numerically more stable and less costly compared to the full model eq. (3.2)-(3.4). The timestep may be increased by an order of magnitude. Thus, coarsening simulations for large times become feasible.

Here, the thin film is modeled by a two dimensional slab perpendicular to the film height. The crystalline order is defined by the density wave,  $\varphi$ . The external magnetic field is assumed parallel to the film and induces a homogeneous magnetization. The magnetic driving force in the model is controlled by the magnitude of the magnetic moments.

We choose a parameter set, which shows stagnation in coarsening to include the effect of retarding forces and reflect the experimental findings. The simulation domain has size  $L^2 = 819.2^2$ . The mean distance of density peaks is one and

is resolved by ten grid points, ( $dx=0.1$ ). Thus, the whole systems consists of  $6.7 \cdot 10^5$  density peaks, representing particles. A time step of  $dt=0.1$  was used.

## 4.2 Coarsening

Eq. (4.1), is used to model magnetic assisted annealing of thin films. The texture of the polycrystalline structure is monitored during annealing in order to extract geometrical and topological properties over time and compare them for different magnitudes  $m$ . To generate an appropriate initial condition we set  $\mathbf{m} = 0$ , start with a randomly perturbed density field  $\varphi$ , and solve eq. (4.1) until we reach a polycrystalline structure with small crystallites with square symmetry. The perturbation is a random distortion at every grid point. The small wavelength perturbations are smoothed rapidly by the evolution equation, but long wavelength perturbation act as nucleation centers. Thus, at random positions grains with random orientation begin to grow until they touch and form a network of grain boundaries. After impingement we got about 1,600 randomly oriented grains. This configuration is used as initial condition for all simulations.

### 4.2.1 Scaling

Fig. 4.1 shows the evolution of the mean grain area,  $\langle A \rangle$ . Coarsening leads to an increase of the mean grain area over time. The coarsening is enhanced by increasing the magnetization and, thus, the magnetic anisotropy. We identify scaling regimes by a power law,  $\langle A \rangle \propto t^\alpha$ , with a scaling exponent  $\alpha$ . In all cases a first scaling regime Fig. 4.1(B) is reached after an initial phase Fig. 4.1(A). Without magnetization a scaling exponent of  $\alpha = 1/3$  is observed. Increasing the magnetic influence increases the scaling exponent. The maximum scaling exponent  $\alpha = 1$  is achieved for  $m = 0.8$ . However, this scaling regime ends. For small magnetic influence below some threshold, it turns into stagnation, Fig. 4.1(C). Above this threshold, here  $m \geq 0.5$ , the scaling becomes independent of magnetic interaction and we observe  $\alpha = 1/3$ , Fig. 4.1(D).

It has been shown before that without magnetic driving force the scaling ex-

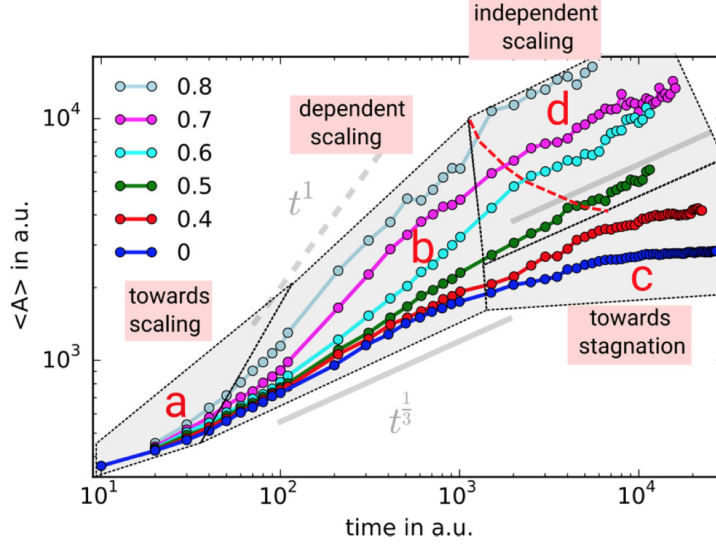


Figure 4.1: Long time evolution of mean grain area for different magnetization. Four different regimes are identified: (A) towards scaling, an initial phase; (B) dependent scaling, a magnetically enhanced scaling regime with the scaling exponent depending on  $m$ ; (C) towards stagnation, a regime which is only present without or with low magnetic fields; and (D) independent scaling, a regime reached at late times, with a scaling exponent independent of magnetic anisotropy.  $m$  is varied between  $[0; 0.8]$  and models the strength of magnetic influence and anisotropy.

ponent depend on initial conditions and modeling parameters [6]. This also remains if magnetic driving forces are included. The identified regimes (A), (B), (C) and (D) thus also depend on initial conditions and modeling parameters. Without magnetic driving force the texture becomes self similar during coarsening [6, 15]. This is not the case for magnetically enhanced coarsening due to grain selection. In the following we analyze texture evolution during coarsening in detail in order to understand the change of the scaling behavior.

### 4.2.2 Orientation selection

The magnetic driving force leads to preferable growth of grains, which are preferably aligned with respect to the external magnetic field. Fig. 4.2 shows typical orientation distributions and how they evolve over time dependent on the magnetic influence. The color represents the local crystal orientation,  $\theta$ . A preferably aligned crystal corresponds to  $\theta = 0$  and, due to symmetry, the  $\theta$  varies in the

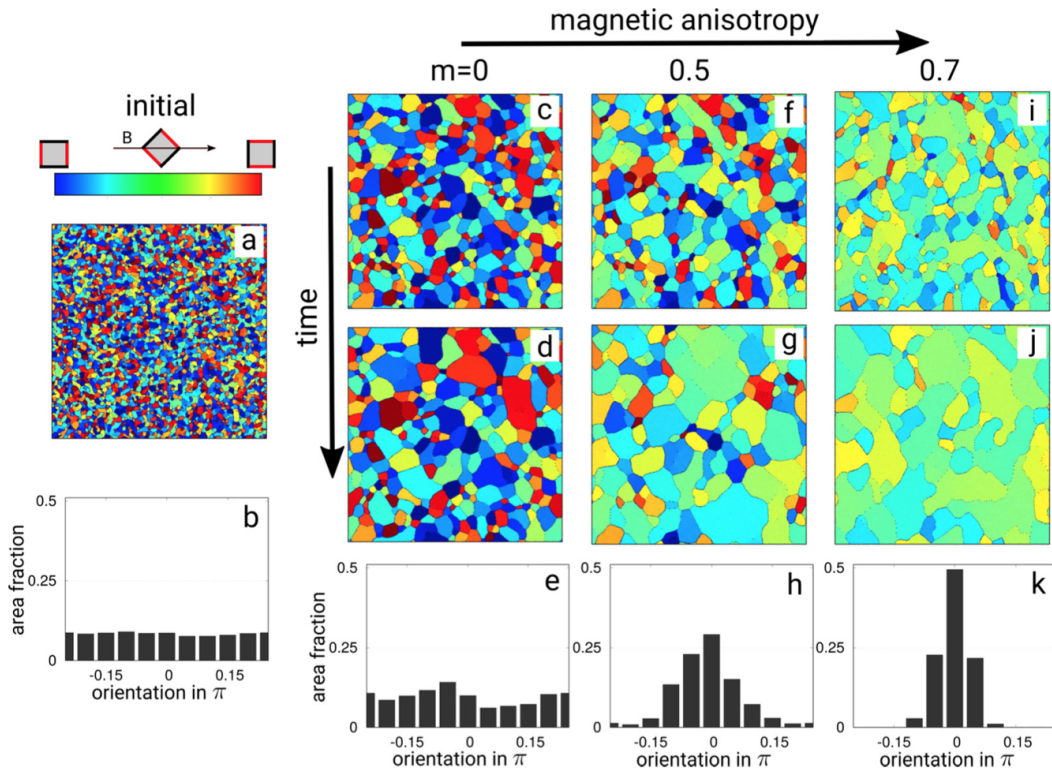


Figure 4.2: Grain structure during annealing. The color represents the local orientation of the easy axis with respect to the external magnetic field. The area fraction is shown as function of orientation for the initial and final configurations for different magnetic fields  $m$ . The times for the snapshots for  $m=0$ ,  $0.5$  and  $0.7$  are  $(9 \cdot 10^3, 2.7 \cdot 10^4)$ ,  $(1 \cdot 10^3, 1.1 \cdot 10^4)$  and  $(4.1 \cdot 10^3, 1.6 \cdot 10^4)$ , respectively.

range  $[-0.25\pi, 0.25\pi]$ .

The initial orientation distribution is constructed without magnetization. Thus, it is homogeneous, Fig. 4.2(a,b). There is no preferred orientation for the grains. Without a magnetic driving force,  $m = 0$ , the orientation distribution stays homogeneous, Fig. 4.2(c,d,e). With a magnetic driving force this changes and well aligned grains grow preferentially, Fig. 4.2(f,g,i,j). Grains with  $\theta \approx 0$  (green) grow at the expense of the other grains (blue, red). As already quantified in Fig. 4.1, the enhanced grain growth with increasing  $m$  can be seen also by larger grain sizes for increasing  $m$ , Fig. 4.2(d,g,j). However, we are here interested in the orientation distribution, which becomes sharply peaked at  $\theta = 0$ , Fig. 4.2(e,h,k). The effect increases with increasing magnetic driving force, as already analyzed for the full model in [7].

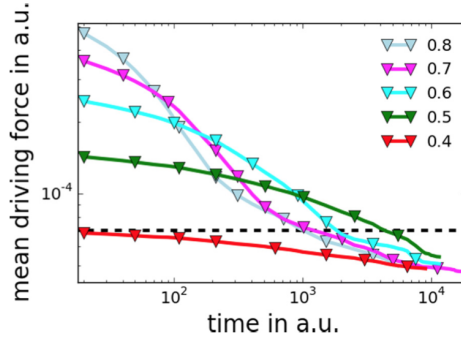


Figure 4.3: Mean magnetic force during coarsening for different applied magnetic fields  $m$ .

The narrowing in orientation distribution has an effect on the total impact of the external magnetic field. As it reduces the mean orientation difference of adjacent grains it also reduces the mean magnetic driving force. To measure this effect we define the mean magnetic driving force as the average energy difference due to magnetic anisotropy with respect to a perfectly aligned crystal. Fig. 4.3 shows this quantity over time. Initially the mean magnetic driving force strongly depends on the strength of the magnetic field. Large  $m$  lead to large magnetic anisotropy and, thus, large magnetic driving forces. But over time the mean magnetic driving force decreases as the mean orientation deviation from a perfectly aligned crystal decreases due to grain selection. The strength of this effect correlates with the strength of the magnetic field. At large times, the



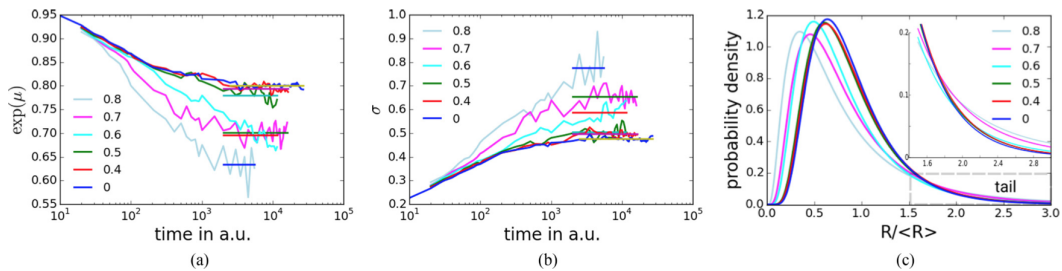


Figure 4.4: Log-normal distribution parameters  $\exp(\mu)$  (a) and  $\sigma$  (b) over time and GSD (c) for final averaged values for  $m$  between  $[0; 0.8]$ . The data for  $m = 0$  correspond with [6] and the experimentally found universal GSD in [15].

mean magnetic driving force falls below a threshold. This large time behavior correlates with the independent scaling regime in Fig. 4.1(D), which occurs, when the mean magnetic driving force falls below  $\approx 0.7 \cdot 10^{-4}$ . The time this threshold is reached depends on  $m$  and is indicated by the dashed (red) line in Fig. 4.1. Thus, orientation selection induced by the external magnetic field over time decreases the influence of the magnetic field, which explains the transition to the independent linear scaling (D) in Fig. 4.1. In the case of stagnation,  $m < 0.5$ , the mean magnetic driving force never exceeds the defined threshold.

### 4.2.3 Grain size distribution

The external magnetic field does not only change the orientation distribution but also the grain size distribution (GSD). Without external magnetic fields it was shown in [6] that the coarsening becomes self similar and the GSD is well described by a log-normal distribution:  $(\sqrt{2\pi}\sigma x)^{-1} \exp(-\frac{(\log x - \mu)^2}{2\sigma^2})$ , where  $x$  is the scaled radius  $\frac{R}{\langle R \rangle}$ . We calculate the GSD for all coarsening simulations and fit log-normal distributions to our results. In Fig. 4.4(a,b) the two values defining the log-normal distribution,  $\exp(\mu)$  and  $\sigma$  are shown over time. During the dependent (magnetically enhanced) scaling, Fig. 4.1(B),  $\exp(\mu)$  and  $\sigma$  change:  $\exp(\mu)$  decreases, while  $\sigma$  increases. Thus, the GSD is not constant over time and, thus, the coarsening is not self similar. Only within the independent scaling regime and towards stagnation, Fig. 4.1(C,D), the GSD becomes stationary on average. Thus, self similar growth is achieved.

As the number of grains is drastically decreased within this regime the GSD

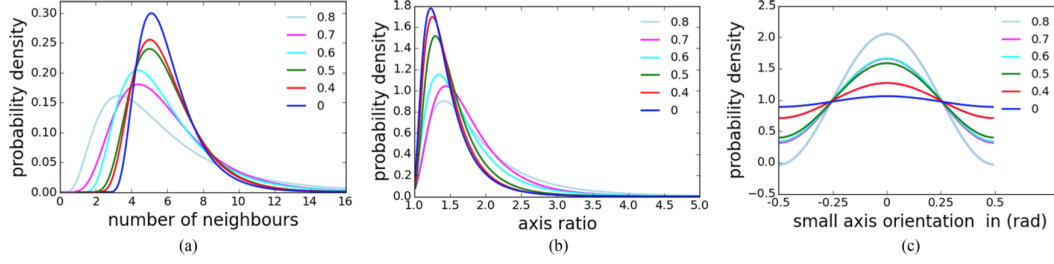


Figure 4.5: Log-normal description for next neighbor distribution (NND) (a), the smoothed distribution should of course be interpreted in a discrete setting, axis ratio distribution (ARD) (b) and cosine description for small axis orientation distribution (SAOD) (c), obtained from late time coarsening regime.  $m$  is varied between  $[0; 0.8]$ . Note: the NND has only discrete values and is represented by a smooth density distribution to show the influence on  $m$ .

statistics become more and more noisy. Fluctuations in the GSD approximation increase for larger times and higher magnetic influence. In order to compare the GSD for different external magnetic fields in the limit of large times, we average  $\exp(\mu)$  and  $\sigma$  for large times and use the averaged value to reconstruct the log-normal distribution, see Fig. 4.4(c). Large external magnetic fields,  $m > 0.5$  shift the maximum of the GSD towards smaller sizes. But the tail becomes wider. Thus, the number of large grains with respect to the average grain size is increased. For smaller external magnetic fields,  $m < 0.5$  the tendency is the same but the difference is minor.

#### 4.2.4 Grain coordination and shape

Various other geometrical and topological measures have been considered to define the grain structure. The next neighbor distribution (NND) or coordination number of grains counts the number of neighboring grains. The shape of grains can be quantified by approximating every grain by an ellipse. The ratio of the axis of the ellipse then measure the elongation of grains. This leads to the axis ratio distribution (ARD). Elongated grains may have preferred direction of elongation. This is measured here by the angle of the small axis with the external magnetic field and lead to a small axis orientation distribution (SAOD).

We concentrate on large times for which the coarsening is self similar. Fig. 4.5(a)

shows the NND, which is also fitted by a log-normal distribution. With increasing external magnetic field the distribution broadens and the maximum is shifted to smaller values. This can already be related to the faster growth, which leads to larger grains and thus also an increased difference in grain size. Classical empirical laws for topological properties in grain structures, such as the Lewis' law and the Aboav-Weair's law, see [24] for a review, show a linear relation between the coordination number and the area of the grains and postulate that grains with high (low) coordination number are surrounded by small (large) grains, respectively. These effects are further enhanced by the elongation of grains, which lead to more neighbors. Additionally, small grains between elongated grains have less neighbors.

The ARD can also be approximated by a log-normal distribution, Fig. 4.5. With increasing magnetic anisotropy the ratio increases and more and more elongated grains are present. The orientation of the elongation is correlated with the external magnetic field. In Fig. 4.5 the orientation distribution of the small axes with the direction of the external magnetic field (SAOD) is shown. Here the distribution is approximated by a cosine. The elongated grains become more and more oriented perpendicular to the external magnetic field.

### 4.3 Discussion

Classical Mullins-like models for grain growth predict self similar growth and a scaling law  $\langle A \rangle \propto t^\alpha$  with a scaling exponent  $\alpha = 1$  [58]. This also does not change if external magnetic fields are introduced as an additional driving force. In contrast to our simulation, see Fig. 4.1, no influence of the scaling behavior is observed. Even though the texture depends on strength and direction of the external magnetic field [2, 17, 36, 51, 54, 57]. In these simulations the increase of growth of well aligned grains is leveled by the decrease of growth of not well aligned grains. Thus, the scaling exponent is predicted to be independent of the additional driving force. In these models, smaller exponents and stagnation of grain growth, as observed in experiments [15], can only be achieved by introducing additional retarding or pinning forces.

Within the considered PFC model triple point and orientational pinning are

naturally present, which is one reason for the observed lower scaling exponent and the stagnation [6]. External magnetic fields introduce an additional driving force to the system. If large enough they can overcome the retarding forces and enhance growth. This explains the dependent growth regime with scaling exponents depending on the applied magnetic field. If the magnetic driving force is large enough all retarding forces are overcome and an exponent of  $\alpha = 1$  is reached.

Grain growth under an applied magnetic field leads to preferable growth of well aligned grains. It is this grain selection which decreased the mean magnetic driving force over time. If the texture is dominated by well aligned grains, the magnetic driving force is no longer a function of the applied field but is limited by the texture, see Fig. 4.3. Only parts of the retarding forces can be overcome and the scaling exponent becomes independent of the magnetic interaction. Turning off the magnetic field in this regime of well aligned grains leads to stagnation. It can only be speculated about the origin of this retarding forces and the mechanism they are overcome by the magnetic field. But, crystalline defects and elastic properties are known to be modified by the local magnetization [7] and lead to magnetization dependent mobilities. The same mechanism may also open new reaction paths for defect movement which might remove the retarding forces.

In the case of small magnetic field the coarsening stagnates. In this regime the magnetic driving force is not large enough to overcome the retarding force responsible for stagnation.

Within the independent scaling regime self similar growth is observed which allows to compute various geometrical and topological properties of the grain structure. Their dependence on the magnitude of the applied magnetic field has been analyzed. The considered grain size distribution (GSD), next neighbor distribution (NND) and axis ratio distribution (ARD) broaden with increasing magnetic anisotropy, leading to larger grains, more grains with very few and many neighbors, and more elongated grains, see Figs. 4.4 and 4.5. The shift in the NND to smaller coordination number has also been reported for simulations based on Mullins type models [54].

Even though, texture control by magnetic fields is of increasing interest [66] there

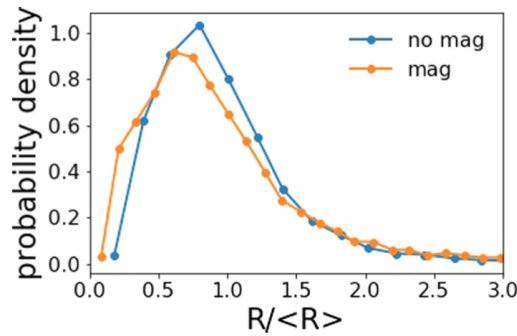


Figure 4.6: GSD of Zr sheet after annealing with and without magnetic fields of 19 T. Data is extracted from Fig. 14 in [55]. The mean grain size  $\langle R \rangle$  is  $10\mu\text{m}$  for the sample annealed without magnetic field and  $18\mu\text{m}$  for the sample annealed with magnetic field.

are not much data on the influence of magnetic fields on GSD in thin films available. In [55] the texture and grain size evolution of thin Zr sheets annealed with and without magnetic fields at different temperatures are studied. Increasing temperature and applying external magnetic fields lead to increasing mean size of the grains. The orientation of the final grains are influenced by the magnetic field and the orientation distribution becomes peaked at favorable orientations. The same tendency as predicted by our simulations, Fig. 4.2. In Fig. 4.6 the GSD are compared for these samples after annealing with and without magnetic field. The magnetic field shifts the peak of the GSD towards smaller values leading to an increase of relatively small grains and relatively large grains. The GSD also widens and the tail is increased by the magnetic field. Also these details in the evolution follow qualitatively our simulation results, Fig. 4.4. But we are not aware of an experimental study showing the increased elongation of the grains perpendicular to the external magnetic field.

## 4.4 Conclusion

We studied magnetically enhanced coarsening with an extended PFC model. The external magnetic field is assumed to be strong enough to prescribe the magnetization of the thin film. That is, the magnetization is constant and per-

fectly aligned with the external magnetic field. The anisotropy of the magnetic properties of the crystal lead to a magnetic driving force. Well aligned crystals grow at the expense of not well aligned crystals. Additionally, magnetostriction leads to deformation of crystal and defect structures.

The magnetic driving force leads to grain selection and a texture dominated by well aligned grains. As the amount of similar oriented grains increase, the mean orientation difference between grains decreases. Thus, the mean magnetic driving force also decreases with time due to texture change. The scaling exponent becomes independent for large times and for large enough magnetization. Stagnation and variation of scaling exponents is due to retarding and pinning forces for grain boundary movement. There are two mechanisms in magnetically enhanced coarsening, which change the effect of retarding forces. Firstly, the magnetic driving force helps to overcome the retarding forces during coarsening. This explains the scaling regime dependent on the magnetic anisotropy. Secondly, the change of structure of the crystal due to magnetostriction can decrease the energy barriers representing the retarding force. Then the driving force due to minimization of grain boundary energy may become large enough to overcome the retarding forces. This could explain the independent scaling regime.

But not only the scaling changes, characteristic geometric and topological properties are also influenced by the applied magnetic field. At least for GSD and NND experiments show the same tendency as predicted by our simulations.

# 5 | Controlling magnetic anisotropy in PFC

## 5.1 Introduction

In the preceding chapters a magnetic PFC model is used to study coarsening of thin films. This model already includes magnetic anisotropy and magnetostriction. Thus, an applied magnetic field can change coarsening due to grain selection [7, 9]. The model studied in the previous chapters have two main limitations, which will be addressed in this chapter: Size limitations due to the atomic resolution of the density wave defining PFC and efficient control of magnetic anisotropy.

PFC is based on the density wave  $\varphi$ , which resolves the crystalline structure of the material under consideration. Thus, the formation and dynamics of defects are naturally described [18, 19, 30]. This is the key accomplishment of PFC. But the spatial resolution on an atomic scale also limits its applicability. Even for strained single crystals, without any defects, the density wave has to be resolved numerically on the atomic scale. That is, a minimum of  $5^d$  grid points per particle is needed for the numerical representation of  $\varphi$ , where  $d$  is the dimension. Fortunately the main characteristics of grain growth in columnar thin films can be modeled by 2-D set ups. We showed in Chapter 2-4 grain coarsening and grain selection, but in 3 dimensions this approach becomes computationally very costly. Nevertheless, there is some work studying grain growth [75], grain shrinkage [87] and defect dynamics [20] in 3-D with PFC.

Additionally, a strained single crystal can be well described by a deformation field applied to an unstrained reference crystal. The deformation varies typically on scales larger than the atomic distance and quantifies the deviation from a

reference crystal. This is the basic idea, that leads to the amplitude expansion of PFC models (APFC) [4, 27, 60, 62]. APFC is shortly introduced in the following section 5.2.

The other limitation of the current model is the magneto structural coupling. The magneto structural interaction is modeled by energy terms coupling the density wave with the local magnetization field,  $\mathbf{m}$ . In Chapter 3 and 4 we used the simplest coupling approach originally proposed in [72]. This model has only one parameter,  $\alpha_2$ , in order to control the relevant magnetic phenomena: strength of magnetic anisotropy, hard and easy direction of magnetization and magnetostriction. Increasing the coupling strength  $\alpha_2$  just increases magnetostriction and magnetic anisotropy altogether, but does not control the easy and hard direction of magnetization. Thus, the applied model does not have the flexibility to adapt the magnetic anisotropy to different materials. That is, the approach does not allow to choose the easy direction freely. Unfortunately, in 3-D the easy and hard direction in BCC and FCC does not resemble typical magnetic materials: Iron and Nickel, see Chapter 5.4. In order to control the easy direction of magnetization Seymour [72] propose an extension to achieve better control of magnetic anisotropy. But this extension has highly nonlinear coupling terms between the magnetization and density wave. The proposed model is hard to interpret and becomes numerically more involved.

In section 5.3 we firstly introduce the few mode approximation to PFC (FMA) in order to analyze the basic magneto-structural coupling. The FMA is simplification of the amplitude expansion applicable for single crystals without any defects or grain boundaries. The analysis of the free energy allows us to identify the core term controlling the magneto-structural interaction. The contribution of this term to the total free energy can be visualized by the construction of the minimum energy surface (MES), which will be defined there.

The MES is used to discuss the magneto-structural coupling for BCC and FCC crystals in the simplest model for magneto-structural coupling in section 5.4.1. In section 5.4.2 an extended magnetic coupling in PFC is proposed and analyzed. Hard and easy directions of magnetization may be controlled in the extended model. That is, the model can be adapted to qualitatively model the magnetic properties of iron or nickel. It does not introduce highly nonlinear term and,



thus, can be interpreted in terms of the MES. It does not introduce further numerical difficulties.

In the next to last section of this Chapter 5.5 the amplitude expansion for the extended PFC model is used to examine the magnetic influence on the evolution of a spherical grain in 3-D.

We summarize our approach for controlling magneto-structural interaction in PFC and APFC in the last section of this Chapter 5.6.

## 5.2 Amplitude expansion of PFC (APFC)

For the amplitude expansion we start from a slightly different parameterization of the free energy for PFC than used in in Chapter 2-4. The free energy is assumed to be [27, 70]:

$$\mathcal{F}[\varphi] = \int_{\Omega} \frac{B_0^x}{2} \varphi (q_0^2 + \nabla^2)^2 \varphi + \frac{\Delta B_0}{2} \varphi^2 - \frac{t}{3} \varphi^3 + \frac{v}{4} \varphi^4 \mathrm{d}\mathbf{r}. \quad (5.1)$$

$q_0$  defines the lattice spacing in equilibrium.  $B_0^x$ ,  $\Delta B_0$ ,  $t$  and  $v$  are modeling parameter. Together with  $\bar{\varphi}$ , as  $\bar{\varphi}$  is conserved over time, they define crystal structure and properties [30, 49, 78]. The parameters used in this work are listed in table 5.1.

t	v	$\bar{\varphi}$	$B_0^x$	$\Delta B_0$
1	1	0	0.98	0.02

Table 5.1: Modeling parameters for APFC.

This parameterization is easily transformed to the PFC energy used in the previous chapters by rescaling,  $b$ , and shifting,  $a$ , the density:  $\varphi \rightarrow \frac{\varphi+a}{b}$ . Such a rescaling was used in the derivation of the PFC model from cDFT in order to compare to remove the cubic term and compare to previous studies [34]. In our amplitude expansion such a scaling is used to allow vanishing mean densities:  $\bar{\varphi} = 0$ . This will simplify the amplitude expansion without loss of generality in our case.

In APFC the density wave is expressed in terms of the deformation to an undisturbed reference crystal. The reference crystal is defined by a set of  $\mathbf{k}$  vectors,

$\{\mathbf{k}_j\}$ . Every  $\mathbf{k}_j$  defines a single density wave. The combination of all density waves lead to density peaks at the positions of the atoms in the reference crystal [27]:

$$\varphi_{ref}(\mathbf{r}) = \bar{\varphi} + \sum_j A_{ref,j} \exp^{i\mathbf{k}_j \cdot \mathbf{r}} + c.c., \quad (5.2)$$

where  $\bar{\varphi}$  is the mean density. The real amplitudes,  $A_{ref,j} \in \mathbb{R}$ , are chosen to minimize the free energy for the chosen crystal structure. The amplitudes describe the amount of ordering and vanish for homogeneous or liquid phases. In APFC, the  $\{\mathbf{k}_j\}$  are a priori chosen to represent a crystal, e.g. BCC or FCC. They are constant in space and time.

The local deviation from this reference structure can be described by extending to complex and space dependent amplitudes,  $A_j(\mathbf{r}) \in \mathbb{C}$ :

$$\begin{aligned} \varphi(\mathbf{r}) &= \bar{\varphi} + \sum_j A_j(\mathbf{r}) \exp^{i\mathbf{k}_j \cdot \mathbf{r}} + c.c. \\ &= \bar{\varphi} + \sum_j A_{ref,j} \frac{|A_j(\mathbf{r})|}{A_{ref,j}} \exp^{i(\mathbf{k}_j \cdot \mathbf{r} + \Phi_j(\mathbf{r}))} + c.c., \end{aligned} \quad (5.3)$$

where  $\Phi_j(\mathbf{r})$  is the phase of  $A_j$ . The phase encodes the deformation of the crystal and the norm of the amplitude,  $|A_j(\mathbf{r})|$ , the change in ordering. In this work we are only interested in bulk crystals and polycrystalline structures. Thus, we assume  $\bar{\varphi}$  to be constant in regions of interest. Then we can use rescaling of  $\varphi$  to have  $\bar{\varphi} = 0$ . An amplitude expansion including slowly varying mean density of  $\varphi$  is reported in [60, 88]. Further on, the explicit space dependence for  $\varphi(\mathbf{r})$  and  $A_j(\mathbf{r})$  will be omitted.

In order to derive the amplitude expansion of PFC, the ansatz, eq. 5.3, is plugged in to the PFC energy assuming  $A_{ref,j} = 1$ . If we assume that the amplitudes,  $A_j$ , vary on larger length scale, than the density wave,  $\varphi$ , the fluctuations on small scales can be averaged [60], treated by multi scale analysis [4, 27] or renormalization techniques [4, 62]. All techniques show that only resonant terms contribute to the energy eq. 5.1 in this limit. That is, only terms, where the phases of the reference density wave,  $\mathbf{k}_j \cdot \mathbf{r}$ , cancel each other remain. Then the

free energy reads:

$$\mathcal{F}[\{A_j\}] = \int_{\Omega} \sum_{j=1}^N \left( B_0^x A_j^* \mathcal{G}_j^2 A_j - \frac{3v}{2} |A_j|^4 \right) + \frac{\Delta B_0}{2} A^2 + \frac{3v}{4} A^4 + f^S(\{A_j\}) d\mathbf{r}, \quad (5.4)$$

where  $A^2 \equiv 2 \sum_{j=1}^N |A_j|^2$ ,  $A^4 = (A^2)^2$  and  $\mathcal{G}_j \equiv q_0^2 - \mathbf{k}_j^2 + \nabla^2 + 2i\mathbf{k}_j \cdot \nabla$ . Usually the equilibrium crystal is chosen as a reference, which leads to  $|\mathbf{k}_j| = q_0$ .  $f^S$  is a polynomial function in  $A_j$  and  $A_j^*$ . It depends on the reference crystal structure indicated by S, e.g. S=FCC or BCC. Dependent on the crystal structure different sets of  $\mathbf{k}_j$  sum up to zero. Only this resonant terms contribute to the free energy. For FCC and BCC the  $f^S$  is listed in [70] or in Chapter 5.4, where the magneto-structural interaction is analysed in detail.

The amplitude expansion of the free energy can be split in three characteristic parts: The first part acts directly on deformation:

$$\sum_{j=1}^N B_0^x A_j^* \mathcal{G}_j^2 A_j. \quad (5.5)$$

The second is independent on deformation and crystal structure:

$$\sum_{j=1}^N -\frac{3v}{2} |A_j|^4 + \frac{\Delta B_0}{2} A^2 + \frac{3v}{4} A^4, \quad (5.6)$$

and the third part is independent on deformation but depends on the crystal structure:

$$f^S(\{A_j\}) \quad (5.7)$$

The first term in eq. 5.5 solely defines the mean distance of the particles and depends on local deformation of the crystal. It is the only term directly dependent on the phases of  $A_j$ . It leads to the elastic properties of the model [30, 68]. This term is mainly<sup>1</sup> due to the approximation of the correlation function

---

<sup>1</sup>There is an ambiguity in the quadratic terms of  $\varphi$ . Such terms are due to approximation of entropic and excess free energy.

in PFC [32, 77].

The second part only depends on  $|A_j|$ , eq. 5.6, and, thus, are independent on crystal structure and deformation. The phases of  $A_j$  always annihilates with the phase of  $A_j^*$ . That is,  $A^2$  does not vary due to deformation unless  $A_j$ . That is,  $A_j^2$  does not vary due to the phase of  $A_j$ . It depends only on local ordering. This property of  $|A_j|$  is used to identify grain boundaries and defect networks in APFC [69, 70]. This term is due to the quadratic and higher order contribution of the density  $\varphi$  in PFC energy.

The third characteristic term, eq. 5.7, is due to the cubic and higher order contribution of the density  $\varphi$  in PFC energy. It depends on the reference crystal assumed for the amplitude expansion of the density, eq. 5.3. Every crystal structure has different sets of  $\mathbf{k}_j$ 's that combine for resonant terms. Thus, different combinations of  $A_j$ 's contribute to  $f^S$ .

The last two discussed parts of the energy does not change due to deformation directly, but their energy contribution varies indirectly, as stretch deformation breaks the symmetry w.r.t.  $A_j$  in the first characteristic term. That is,  $|A_j|$  changes under stretch deformation but pure rotation does not change  $A_j$ . The free energy eq. 5.4 is independent on rotation.

The time evolution of the amplitudes is:

$$\begin{aligned} \frac{\partial A_j}{\partial t} &= -|\mathbf{k}_j|^2 \frac{\delta F}{\delta A_j^*} \\ &= -|\mathbf{k}_j|^2 \left[ \left[ \Delta B_0 + B_0^x \mathcal{G}_j^2 + 3v (A^2 - |A_j|^2) \right] A_j + \frac{\partial f^s(\{A_j\})}{\partial A_j^*} \right], \end{aligned} \quad (5.8)$$

if an long wavelength limit is assumed [88].

In fig. 5.1 the relation of density, amplitudes and  $A^2$  are shown. Fig. 5.1 a) is a 2-D example. A circular grain is constructed by cutting and rotating a circular domain in a perfect triangular crystal and relaxing according eq. 5.8 until a proper grain boundary is achieved. The density peaks represent the particles and defect can be identified. The reference structure of the amplitude expansion is chosen to conform to the initial triangular crystal. Thus, there is no rotation outside of the grain w.r.t. reference structure and the amplitudes are constant and real. Rotation w.r.t. the reference structure leads to periodically varying

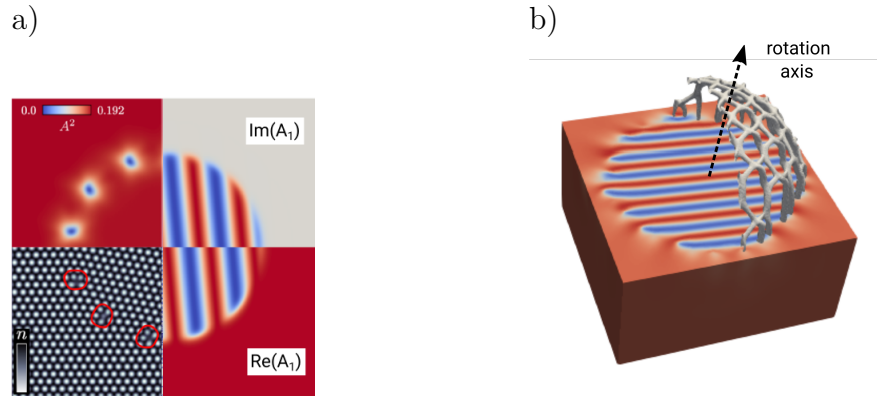


Figure 5.1: Crystal and defect representation in APFC. a) A circular grain in the center rotated w.r.t. the surrounding matrix (2-D). b) A spherical grain (3-D). The defect network is identified by  $A^2$ .

amplitudes inside the grain. However, additional deformations are located near the defects. The defects easily located in the density representation are not easily identified in the amplitudes representation. But  $A^2$  varies strongly at the defects, as there the ordering changes rapidly. Away from the defects the deformation and, thus,  $A^2$  becomes constant. The minima in  $A^2$  are used to identify the defects in the amplitude expansion. The defects form defect networks in 3-D, see Fig. 5.1 b), and define the grain boundary.

A spherical grain is not stable and will shrink in order to minimize grain boundary energy. Fig. 5.2 shows the shrinkage of a spherical grain [69]. FCC and BCC crystals are considered with different axis of rotation. The defect network depends on crystal structure and axis of rotation. The defect structure along top view resembles the defect network of the corresponding planar twist grain boundary. We showed in [69], that the amplitude expansion predicts the defect network expected by PFC simulations, energy considerations and other simulation methods. The shrinkage of the grain is not isotropic. It shrinks faster along the axis of rotation as predicted by PFC simulations [87]. In Chapter 5.2 we will examine the shrinkage of a spherical grain with and without magneto-structural coupling in greater detail.

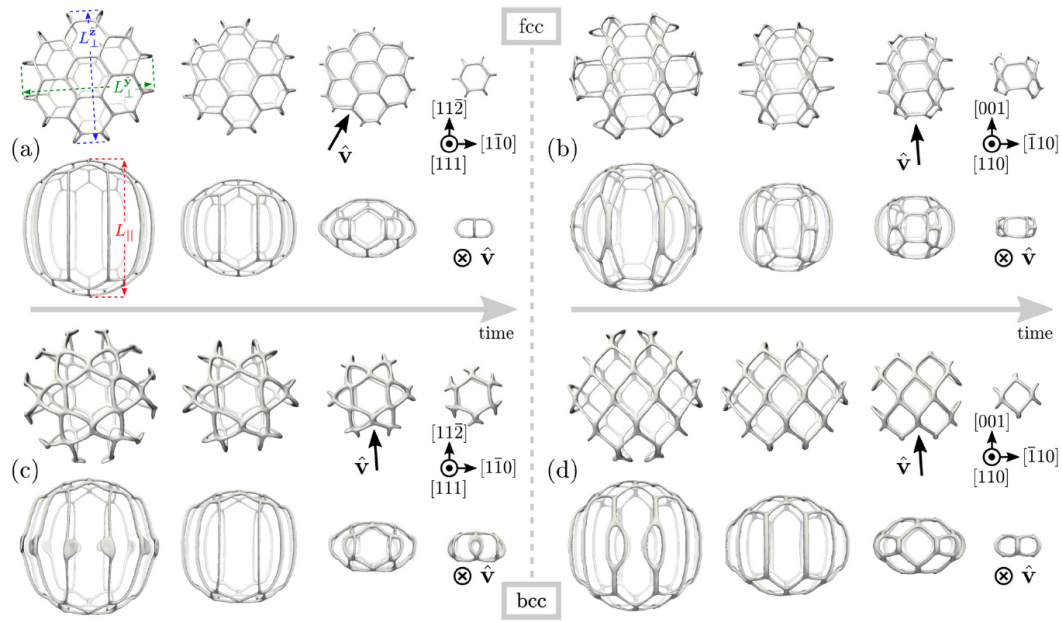


Figure 5.2: Shrinkage of spherical GBs for different symmetries with  $\theta = 5^\circ$ . The views aligned (top) and perpendicular (bottom) to the rotation axis are shown (as also illustrated by  $\hat{v}$ ). (a) fcc symmetry, rotation about the  $[111]$  direction. (b) fcc symmetry, rotation about the  $[110]$  direction. (c) bcc symmetry, rotation about the  $[111]$  direction. (d) bcc symmetry, rotation about the  $[110]$  direction. Panel (a) illustrates also the width of the embedded crystal along different directions. Image from [69].

APFC replaces the density wave defined on atomistic scale in PFC by a set of complex amplitudes,  $\{A_j\}$ , encoding the deviation of the crystal to its reference. This amplitudes varies in space on a length scale dependent on the deviation to the reference structure. Defects are still resolved at atomistic scale, but strained or rotated single crystals are described by a set of slowly varying amplitudes. That is, only at defects, resp. grain boundaries, the amplitudes have to be resolved on the atomic scale. Although it is assumed that the amplitudes vary on a length scale larger than a defect, details at defects are surprisingly well handled by APFC [67, 68]. In this work, we apply spatial adaptive finite elements in order to efficiently solve equation eq. 5.8 at defects and bulk using AMDiS [70, 82]. The APFC model is extended to include magneto structural interaction in Chapter 5.2.

### 5.3 Magneto-structural coupling and minimum energy surface (MES)

In this section we analyze the influence of homogeneous magnetization on a single crystal. That is, the crystal does not have any defects and may only homogeneously be deformed. This simple set up can be analyzed by a simplified amplitude expansion. The density wave is parameterized by real constant Amplitudes,  $A_j$ , and  $\mathbf{k}_j$ :

$$\varphi(\mathbf{r}) = \bar{\varphi} + \sum_j A_j e^{i\mathbf{k}_j \cdot \mathbf{r}} + c.c. =: \varphi(\{A_j\}, \{\mathbf{k}_j\}), \quad (5.9)$$

where  $\{\mathbf{k}_j\}$  is a set of k-space vectors representing the deformed crystalline structure,  $\mathbf{k}_j = \mathbf{D}_k \mathbf{k}_{ref,j}$ .  $\mathbf{k}_{ref,j}$  defines an undeformed crystal structure, e.g. BCC. Every pair  $(A_j, \mathbf{k}_j)$  defines a single mode used to approximate the density wave  $\varphi$ .  $\bar{\varphi}$  is the mean density and is set by rescaling to zero as in APFC:  $\bar{\varphi} = 0$ . Further on we will refer to this ansatz as the few mode approximation (FMA). The FMA is exact solution to APFC for homogeneous deformed single crystals and a very good approximation to PFC solutions [49].  $A_j$  as well as  $\mathbf{k}_j$  are constant in space. Thus, the free energy, eq. 5.4, greatly simplifies to :

$$\frac{\mathcal{F}(\{A_j\}, \{\mathbf{k}_j\})}{\Omega} = \sum_j A_j (q_0^2 - \mathbf{k}_j^2)^2 A_j + g^S(\{A_j\}), \quad (5.10)$$

and w.l.o.g.  $\Omega = 1$ . The last term,  $g^S(\{A_j\})$  is a polynomial in  $A_j$ 's. It depends on the structure S and is defined with eq. 5.4:

$$g^S(\{A_j\}) = - \sum_j \frac{3v}{2} |A_j|^4 + \frac{\Delta B_0}{2} A^2 + \frac{3v}{4} A^4 + f^S(\{A_j\}) \quad (5.11)$$

In [70, 88]  $f^S(\{A_j\})$  is shown for S='BCC' or 'FCC' crystals.  $g^S(\{A_j\})$  is independent on  $\mathbf{k}_j$  and, thus, on deformation of the crystal. The first term in eq. 5.21 depends on  $A_j$  and  $\mathbf{k}_j$ , but does not mix contributions of different k-vectors. It is due to the excess free energy of PFC [32, 77]. The operator acting on  $A_j$  resembles the approximation of a correlation function in k-space. It is invariant



on the orientation of  $\mathbf{k}_j$  and, thus, on rotation of the crystal represented by the density wave.

An external magnetic field breaks the rotational symmetry of a crystal by inducing local magnetization,  $\mathbf{m}$ . Here,  $\mathbf{m}$  is assumed to be constant in magnitude and orientation. Thus, the energy of the crystal may depend on the relative orientation of the crystal w.r.t. the magnetization. The simplest ansatz to include symmetry breaking due to  $\mathbf{m}$  in PFC is [72] and used in Chapter 3 and 4:

$$\mathcal{F}_{\text{coup}}(\varphi) = - \int_{\Omega} d\mathbf{r} \alpha_2 \varphi (\mathbf{m} \nabla)^2 \varphi. \quad (5.12)$$

We assume that  $\mathbf{m}$  is the normalized local magnetization,  $|\mathbf{m}|=1$ . The FMA leads to:

$$\frac{\mathcal{F}_{\text{coup}}(\{A_j\}, \{\mathbf{k}_j\})}{\Omega} = \sum_j \alpha_2 A_j^* (\mathbf{m} \mathbf{k}_j)^2 A_j, \quad (5.13)$$

where  $\alpha_2$  controls the strength of the magnetic interaction and the size of integration domain is w.l.o.g.  $\Omega = 1$ . The total free energy is then:

$$\mathcal{F}(\{A_j\}, \{\mathbf{k}_j\}) = \sum_j A_j^* \left[ (q_0^2 - \mathbf{k}_j^2)^2 + \alpha_2 (\mathbf{m} \mathbf{k}_j)^2 \right] A_j + g^S(\{A_j\}) \quad (5.14)$$

For  $\alpha_2 > 0$  and a single  $\mathbf{k}_j$ , this is minimized when  $\mathbf{k}_j = q_0$  and  $\mathbf{k}_j \perp \mathbf{m}$ . For  $\alpha_2 < 0$  the energy is minimized by  $\mathbf{k}_j \parallel \mathbf{m}$  and  $\mathbf{k}_j^2 = q_0^2 - \alpha_2/2$ . Thus, the  $\mathbf{k}_j$  increases in direction of  $\mathbf{m}$ . The magnetic coupling not only favor some directions of  $\mathbf{k}_j$ , which lead to magnetic anisotropy, but also modify the length of  $\mathbf{k}_j$ , which lead to magnetostriction.

In the FMA the energy has to be optimized w.r.t. a set of  $\mathbf{k}_j$ 's, but the  $\mathbf{k}_j$ 's do not vary independently. In order to preserve the crystal structure all  $\mathbf{k}_j$ 's have to transform according the same deformation  $\mathbf{D}_k$ :

$$\mathbf{k}_j \rightarrow \mathbf{D}_k \mathbf{k}_j. \quad (5.15)$$

$\mathbf{D}_k$  is a deformation in k-space independent on  $\mathbf{k}_j$ . The free energy under such a deformation reads:

$$\mathcal{F}(\{A_j\}, \{\mathbf{k}_j\}) = \sum_j A_j \left[ (q_0^2 - (\mathbf{D}_k \mathbf{k}_j)^2)^2 + \alpha_2 (\mathbf{m} \mathbf{D}_k \mathbf{k}_j)^2 \right] A_j + g^S(\{A_j\}). \quad (5.16)$$

$g^S(\{A_j\})$  is independent on  $\mathbf{k}_j$  and, thus, does not change under deformation  $\mathbf{D}_k$ . It's easy to see, that for a pure rotation,  $\mathbf{D}_k = \mathbf{R}$ , follows  $(\mathbf{D}_k \mathbf{k}_j)^2 = (\mathbf{R} \mathbf{k}_j)^2 = \mathbf{k}_j^2$  and the first term in the sum of eq. 5.16 is rotational invariant. The second term is minimized by rotation for a single  $\mathbf{k}_j$  if  $\mathbf{R} \mathbf{k}_j \perp \mathbf{m}$  for  $\alpha_2 > 0$ . But the same deformation may lead to an increase of energy due to another  $\mathbf{k}_j$ . In order to analyze the energy difference between different oriented crystals resp.  $\mathbf{k}_j$ 's, the deformation has to be restricted to deformations without rotations. In real space the deformation of a crystal may deform relatively to the local magnetization. Due to symmetry considerations, we allow independent deformation perpendicular and parallel to the magnetization. Thus, the deformation is:

$$\mathbf{D} = \mathbf{R}^T \tilde{\mathbf{D}} \mathbf{R} \quad \text{with} \quad \tilde{\mathbf{D}} = \begin{pmatrix} d_0 & 0 & 0 \\ 0 & d_1 & 0 \\ 0 & 0 & d_1 \end{pmatrix}. \quad (5.17)$$

The diagonal matrix  $\tilde{\mathbf{D}}$  describes the deformation, if the first eigenvector is aligned to the magnetization  $\mathbf{m}$ .  $d_0$  is the deformation parallel and  $d_1$  in the plane perpendicular to the magnetization. The rotation  $\mathbf{R}$  aligns the magnetization with the first eigenvector of  $\tilde{\mathbf{D}}$ . Under this deformation the  $\mathbf{k}_j$  in k-space transform as:

$$\mathbf{k}_j \rightarrow \mathbf{D}_k^T \mathbf{k}_j = (\mathbf{D}^{-1})^T \mathbf{k}_j = \mathbf{R}^T \tilde{\mathbf{D}}^{-1} \mathbf{R} \mathbf{k}_j. \quad (5.18)$$

The  $A_j$  are nonlinearly coupled in  $g^S(\{A_j\})$  and can be optimized without restriction, as long as they do not vanish.

The  $\mathbf{k}_j$  minimizing the energy are solely defined by the kernel  $(q_0^2 - \mathbf{k}_j^2)^2 + \alpha_2 (\mathbf{m} \mathbf{k}_j)^2$  and are independent on  $\{A_j\}$ . For a single  $\mathbf{k}_j$  the kernel defines a

surface of minimal energy (MES) in  $\mathbf{k}$ -space:

$$S_{\alpha_2} = \{\mathbf{k} : \min_{\mathbf{k} \parallel \mathbf{n}} \{(q_0^2 - \mathbf{k}^2)^2 + \alpha_2(\mathbf{m}\mathbf{k}_j)^2\} \forall \mathbf{n} \in \mathcal{S}^2\}, \quad (5.19)$$

where  $\mathbf{n}$  is an arbitrary vector at the unit sphere. The  $\mathbf{k}$  on the minimum energy surface minimize the free energy constrained to the orientation of  $\mathbf{k}$ . The kernel evaluated at this  $\mathbf{k}$  is proportional to the energy contribution of  $\mathbf{k}$  to the free energy. Without magnetic interaction,  $\alpha_2 = 0$ , the minimal energy surface is the isosurface defined by  $(q_0^2 - \mathbf{k}^2)^2 = 0$ . Thus, every  $\mathbf{k}$  on the sphere with radius  $q_0$  minimize energy and has a vanishing energy contribution, see fig. 5.3. That is, the radius of the MES reflects the particle distance in the crystal. The magnetic

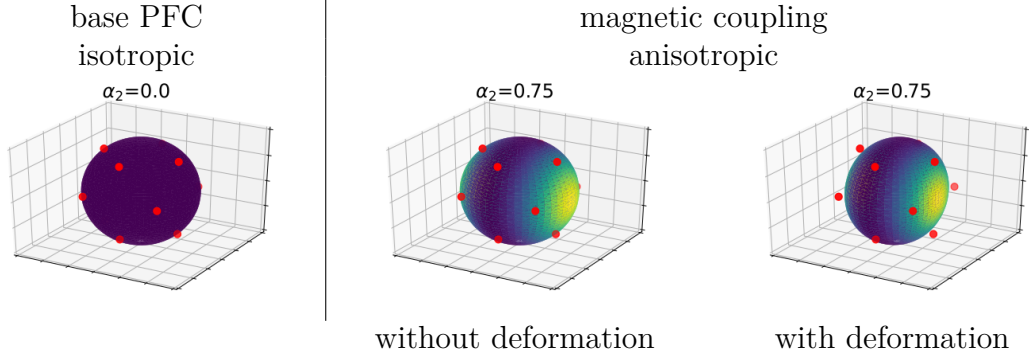


Figure 5.3: Symmetry breaking due to magnetic interaction. Minimum energy surface without (a) and with magnetic coupling according eq. 5.19. The color indicates the energy contribution of a  $\mathbf{k}$  at the minimum energy surface. For  $\alpha > 0$  the energy is increased in direction of  $\mathbf{m}$  and the minimum energy surface is squeezed along  $\mathbf{m}$ .

interaction breaks the rotational symmetry of the minimum energy surface. The shape of the minimum energy surface as well as the energy contribution due to the kernel becomes dependent on orientation of  $\mathbf{k}$ , see fig. 5.3 For a single  $\mathbf{k}$  the energy minimization leads to the  $\mathbf{k}$  on the minimum energy surface with the smallest energy contribution. In a crystalline case the  $\mathbf{k}_j$  are not independent. The same deformation has to be applied to every  $\mathbf{k}_j$ , Eq. 5.18. Thus, the single  $\mathbf{k}_j$  may not lay on the minimum energy surface for the minimum energy state. But, the minimum energy surface visualizes the symmetry breaking due to magnetic

interaction and gives a first hint of the expected anisotropy. It is used in the following to interpret the influence of the magnetic coupling terms.

## 5.4 Magneto-structural interaction in magnetic PFC

In this section we analyze different magnetic coupling terms in PFC. We use FMA, section 5.3, to calculate the free energy of a single crystal with a prescribed magnetization  $\mathbf{m}$ . The magneto-structural interaction is calculated by minimizing the free energy w.r.t  $\{A_j\}$  and deformation along and perpendicular to the magnetization,  $(d_0, d_1)$ . The energy dependence on the direction of  $\mathbf{m}$  defines the magnetic anisotropy. Especially, we find the easy and hard direction of magnetization resp. the low and high energy directions. The magnetostriction is defined by the deformation  $D$ . BCC as well as FCC crystals are considered. Firstly the basic magnetic coupling proposed by Seymour et al [72] is analysed in detail using the MES. With this experience, we propose an extended magnetic coupling. The extended coupling is more flexible and can be qualitatively adapted to the magnetic properties of iron and nickel.

### 5.4.1 Basic model of magnetic coupling

#### The BCC crystal

In section 5.3 the magnetic coupling of Seymour et al. [72] is already discussed. A BCC crystal is defined by a set of  $\mathbf{k}_j$ ,  $\{\mathbf{k}_j\}$ , that describe a FCC structure in k-space. The k-vectors are:

$$\left\{ \frac{\mathbf{k}_j}{k_0} \right\} = \left\{ \begin{pmatrix} 1 \\ 1 \\ 0 \end{pmatrix}, \begin{pmatrix} 1 \\ 0 \\ 1 \end{pmatrix}, \begin{pmatrix} 0 \\ 1 \\ 1 \end{pmatrix}, \begin{pmatrix} 0 \\ 1 \\ -1 \end{pmatrix}, \begin{pmatrix} 1 \\ -1 \\ 0 \end{pmatrix}, \begin{pmatrix} -1 \\ 0 \\ 1 \end{pmatrix} \right\}, \quad (5.20)$$

with  $q_0 = 1$  follows  $k_0 = 1/\sqrt{2}$ . The FMA of the free energy is then:

$$\mathcal{F}(\{A_j\}, \{\mathbf{k}_j\}) = \sum_j A_j \left[ (1 - \mathbf{k}_j^2)^2 + \alpha_2 (\mathbf{m} \mathbf{k}_j)^2 \right] A_j + g^{\text{BCC}}(\{A_j\}), \quad (5.21)$$

setting  $\Omega = 1$ . The first term defines the MES and the deformation independent part is [70]:

$$\begin{aligned}
 g^{\text{BCC}}(\{A_j\}) &= - \sum_j \frac{3v}{2} |A_j|^4 + \frac{\Delta B_0}{2} A^2 + \frac{3v}{4} A^4 + f^{\text{BCC}}(\{A_j\}) \quad \text{and} \\
 f^{\text{BCC}}(\{A_j\}) &= - 2t(A_1^* A_2 A_4 + A_2^* A_3 A_5 + A_3^* A_1 A_6 + A_4^* A_5 A_6 + c.c.) \\
 &\quad + 6v(A_1 A_3^* A_4^* A_5^* + A_2 A_1^* A_5^* A_6^* + A_3 A_2^* A_6^* A_4^* + c.c.). \quad (5.22)
 \end{aligned}$$

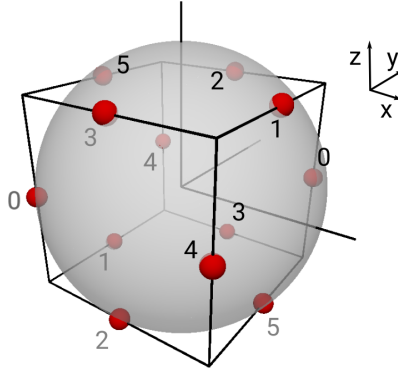


Figure 5.4: The red balls symbolize the  $\mathbf{k}_j \in \{\mathbf{k}_j\}$  defining the BCC crystal. The  $\mathbf{k}_j$  are numbered according eq. 5.20. The energetic equivalent vectors,  $-\mathbf{k}_j$ , are numbered in grey.

The reference structure is chosen, such that all the  $\mathbf{k}_j$  are on the MES for  $\alpha_2 = 0$ . They describe a FCC ordering in k-space, see. Fig. 5.4. All k-vectors are  $[1\ 1\ 0]$  directions on a standard cube. The cube size,  $c = \frac{2\pi}{a}$ , is defined by the particle distance,  $a$ . Thus all  $\mathbf{k}_j \in \{\mathbf{k}_j\}$  are on a sphere, the MES, defined by the standard PFC model. The negative  $\mathbf{k}_j$  are implicit included in the description because of the complex conjugate part in the ansatz for the density wave, eq. 5.9. Due to the symmetry of the crystals and magneto-structural interaction  $\mathbf{k}_j$  and  $-\mathbf{k}_j$  contribute equally to the total energy.

In order to examine influence of the magneto-structural coupling, we firstly consider  $\|\mathbf{m}\|=1$  and three directions for the magnetization:  $[1\ 0\ 0]$ ,  $[1\ 1\ 1]$  and

[110]. It will be shown later in the current section, that this low index directions give a good characterization of the magnetic properties of the model. The strength of magnetic coupling,  $\alpha_2$ , is varied between -0.18 and 0.08.

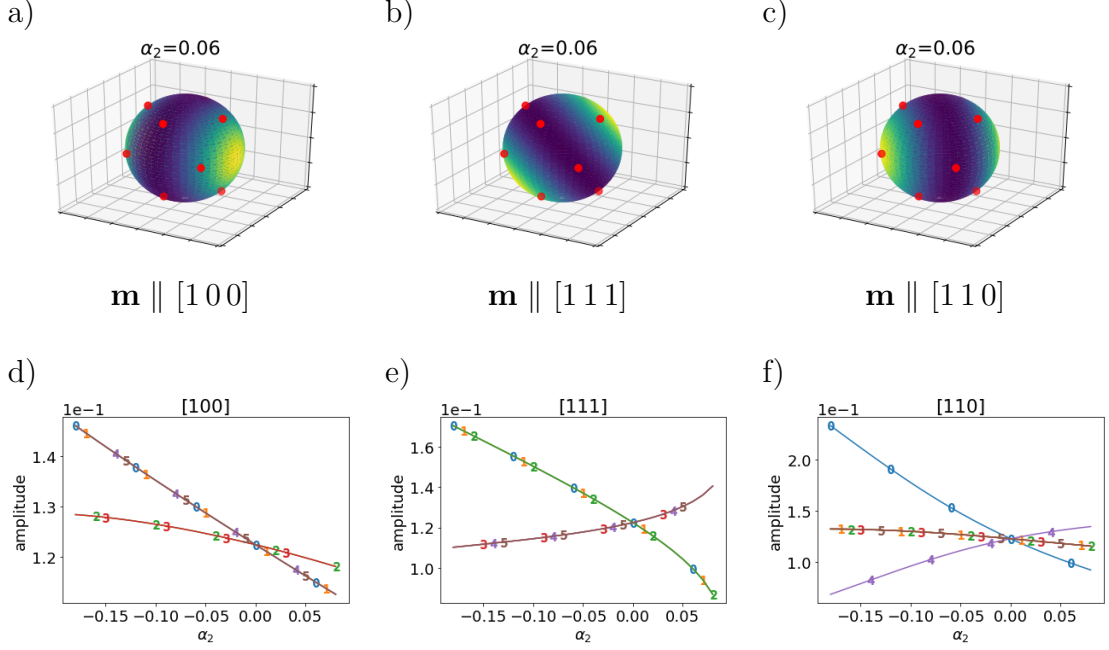


Figure 5.5: Symmetry breaking in the simple magnetic-structural coupling. a)-c): MES of simple magneto-structural coupling for  $\mathbf{m}$  in a) [100], b) [111] and c) [110] direction. The red balls indicate the  $\mathbf{k}_j$  defining the crystal structure in the FMA, eq. 5.20. d)-f) the amplitudes  $A_j$  are shown for varying coupling strength  $\alpha_2$ . Due to symmetry, there are groups of energetically equivalent  $\mathbf{k}_j$ 's. The numbering of  $A_j$  and  $\mathbf{k}_j$  follow fig. 5.4.

For every  $\mathbf{m}$  and  $\alpha_2$  the free energy is minimized w.r.t  $\{A_j\}$  and deformation  $\mathbf{D}$ , see Chapter 5.3. In fig. 5.5 a)-c) the MES for  $\alpha_2 = 0.06$  are shown for the different directions of  $\mathbf{m}$ . The deformation of the MES is very small and not visible. But the energy corresponding to a  $\mathbf{k}_j$  varies clearly at the MES. In the first case, Fig. 5.5 a), is  $\mathbf{m}$  parallel to [100]. Thus energy contribution is maximized for  $\mathbf{k}_j$  parallel to  $\mathbf{m}$ , eq. 5.21. The energy contribution of MES on the  $\mathbf{k}_j$ 's on the yz-plane is lowest. Thus, we get two set of  $\mathbf{k}_j$ 's with different energy contribution to the total energy:  $\mathbf{k}_2$  and  $\mathbf{k}_3$  are on the xy-plane and,

thus, energetically favored (lowest energy).  $\mathbf{k}_0, \mathbf{k}_1, \mathbf{k}_4$  and  $\mathbf{k}_5$  are energetically unfavored. They are symmetrically ordered around the maximum of energy at the MES. If  $\alpha_2 < 0$  then  $\mathbf{k}_2$  and  $\mathbf{k}_3$  are energetically unfavored and  $\mathbf{k}_0, \mathbf{k}_1, \mathbf{k}_4$  and  $\mathbf{k}_5$  are energetically favored.

In order to compensate for the different energetic contribution due to the anisotropic MES, the amplitudes adapt. The corresponding amplitudes of different sets of  $\mathbf{k}_j$ 's react differently. In Fig. 5.5 d)-f), the dependence of the amplitudes  $A_j$  on the coupling strength is shown. Unfavored direction lead to higher energy contributions, this is balanced by smaller amplitudes in this direction. The set of unequal amplitudes leads to anisotropic density peaks, when density is reconstructed, 5.3. An example for elongated peaks is shown in Chapter 3. If the magnetic coupling becomes too strong then some of the amplitudes vanish. Thus, the model does not describe a BCC ordering anymore and the model breaks down for our application. This sets a natural limit for achievable magneto-structural interaction in this model.

If  $\mathbf{m}$  is oriented along  $[1\ 1\ 1]$  and  $\alpha_2 > 0$ , the unfavored set of  $\mathbf{k}_j$ 's are  $\mathbf{k}_0, \mathbf{k}_1$  and  $\mathbf{k}_2$ , Fig. 5.5 b). The three  $\mathbf{k}_j$ 's are placed symmetrically around the energetic maximum at the MES. The favored set of  $\mathbf{k}_j$ 's,  $\mathbf{k}_3, \mathbf{k}_4$  and  $\mathbf{k}_5$ , are at the energetic minimum.  $\mathbf{m}$  is in direction of  $[1\ 1\ 0]$  in the last set up, Fig. 5.5 c) and f). In this case, there are three sets of energetically equivalent  $\mathbf{k}_j$ .  $\mathbf{k}_4$  is at the energetic maximum,  $\mathbf{k}_0$  is at the energetic minimum and the remaining  $\mathbf{k}_j$ 's are energetically equivalent in between. In all cases, the amplitudes for high energy directions become smaller than for high energy directions.

In Fig. 5.6 the free energy of the different set ups shown in Fig. 5.5 are compared dependent on the coupling strength. Without any coupling,  $\alpha_2 = 0$ , there is no symmetry breaking and the total energy is independent on the orientation of  $\mathbf{m}$ . For  $\alpha_2 > 0$  the coupling term is a positive contribution to the free energy. Thus, for all directions of  $\mathbf{m}$  the total energy increases with increasing  $\alpha_2$ . Negative  $\alpha_2$  leads to decreasing energies, Fig. 5.6 a).  $\mathbf{m}$  in  $[1\ 0\ 0]$  direction has the highest energy for all  $\alpha_2$  and, thus, is the hard direction of magnetization. The easy axis depends on the sign of  $\alpha_2$ , Fig. 5.6 b).  $\mathbf{m}$  parallel to  $[1\ 1\ 0]$  has lowest energy for  $\alpha_2 < 0$ . The energy difference between  $\mathbf{m} \parallel [1\ 1\ 1]$  and  $\mathbf{m} \parallel [1\ 1\ 0]$  is small compared to the difference to the hard direction of magnetization. For  $\alpha_2 > 0$



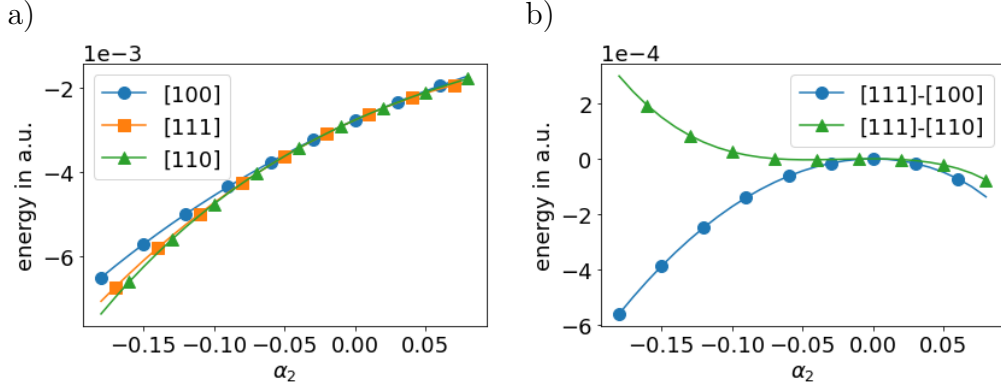


Figure 5.6: Total energy (a) and magnetic anisotropy (b) dependence on strength of magnetic coupling. [100] is always the hard (highest energy) direction of magnetization. The easy (lowest energy) direction is [110] for  $\alpha_2 < 0$  and [111] for  $\alpha_2 > 0$ .

$\mathbf{m}$  in [111] direction has lowest energy.

In Fig. 5.7 a) the free energy for all orientations of  $\mathbf{m}$  are shown at a sphere. The crystal is fixed and its  $\langle 100 \rangle$  directions are aligned with the x-,y- and z-axis. The direction of highest energy and lowest energy reflect the cubic symmetry of the BCC crystal. Here,  $\alpha_2 > 0$ ,  $\langle 100 \rangle$  are the hard directions of magnetization (high energy). The easy direction are  $\langle 111 \rangle$ . The  $\langle 110 \rangle$  directions are saddle points in the energy landscape. Thus all basic features of the energy landscapes are located at the low index directions.

Due to the cubic symmetry, it is enough to study the energy in the triangle defined by [100],[110] and [111], see Fig. 5.7 b). The characteristic directions are in the low index directions. Thus, energy along the bound of this triangle gives a good view of the magnetic anisotropy.

Fig. 5.7 c) shows the energy surface. The distance of the surface to center scales with the energy in this direction. Thus, the hard direction of magnetization are the highest spikes at the energy surface. The easy directions of magnetization correspond to the deepest holes.

In Fig. 5.8 the magnetic anisotropies for  $\alpha_2 = 0.06, -0.04$  and  $-0.08$  are compared. The free energy is plotted along the edges of the triangle defined by

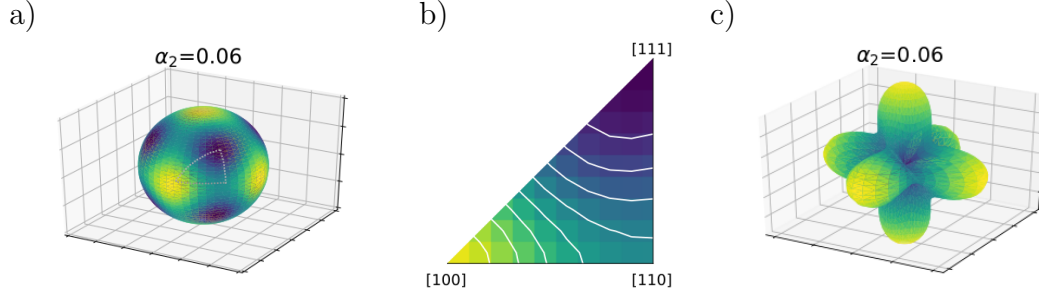


Figure 5.7: Free energy of BCC crystal dependent on  $\mathbf{m}$  with fixed coupling strength  $\alpha_2 = 0.06$ . The  $\langle 100 \rangle$  directions of the crystal are aligned with the  $x$ -,  $y$ - and  $z$ -axis. Yellow correspond to high and blue to low energy directions of  $\mathbf{m}$ . a) free energy on the sphere representing the orientation of  $\mathbf{m}$ . b) free energy in the triangle  $[100]$ ,  $[110]$  and  $[111]$ . c) energy surface. The easy (low energy) and hard (high energy) directions of magnetization are  $\langle 111 \rangle$  resp.  $\langle 100 \rangle$ .

$[100]$ ,  $[110]$  and  $[111]$ , see Fig. 5.8 a). This shows the basic features of magnetic anisotropy, as all extrema of the free energy are located at this edges, see Fig. 5.7. The energy is measured relative to the energy of easy direction (minimum energy). In all cases there is a maximum at  $[100]$ . The height of the maximum increases with increasing coupling strength  $|\alpha_2|^2$ . That is, the magnetic anisotropy increases with coupling strength. For  $\alpha_2 = -0.08$  the energetic minima are in the  $\langle 110 \rangle$  directions. In the other cases they are in the  $\langle 111 \rangle$  directions. For  $\alpha_2 < 0$  the difference between the  $\langle 111 \rangle$  and  $\langle 110 \rangle$  directions is quite small compared to the hard directions,  $\langle 100 \rangle$ . Thus, the easy direction is not very distinguished.

The magnetic coupling does not only lead to magnetic anisotropy, but also leads to a deformation of the crystal. In Fig. 5.9 the deformation of the crystal is shown for  $\mathbf{m}$  in  $[111]$  direction. The length of the  $\mathbf{k}_j$  in the optimized state is shown in Fig. 5.9 a). All  $\mathbf{k}_j$  transform according to the same deformation  $\mathbf{D}_k$ . The deformation leads to the same length in each set of energetically equivalent  $\mathbf{k}_j$ 's due to symmetry. The length of  $\mathbf{k}_j$  in the favored set,  $\mathbf{k}_0$ ,  $\mathbf{k}_1$  and

---

<sup>2</sup> $\alpha_2 > 0$  and  $\alpha_2 < 0$  has to be considered separately.

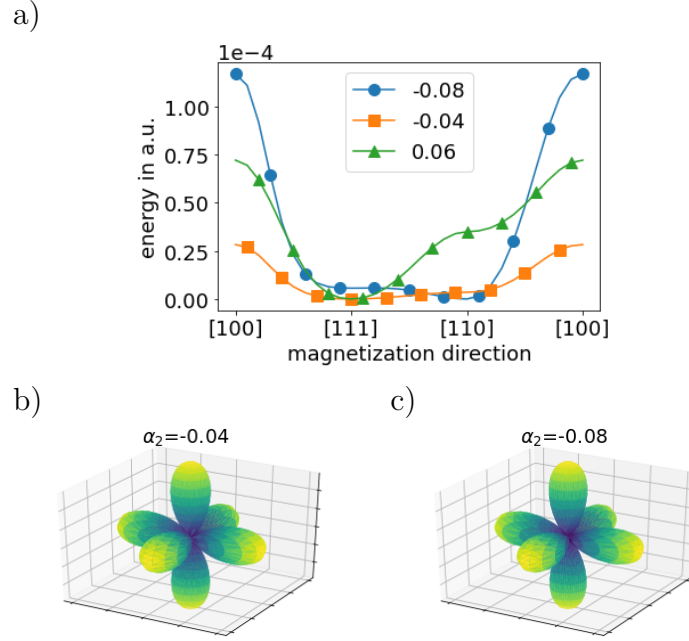


Figure 5.8: Comparing magnetic anisotropy for  $\alpha_2 = 0.06, -0.04$  and  $-0.08$ . a) energy along the edges of the triangle defined by  $[100]$ ,  $[111]$  and  $[110]$ , Fig. 5.7 c). Maximum defines the hard direction and minimum the easy direction of magnetization. The energy is plotted relative to the minimum energy (easy direction). b) and c) energy surface for  $\alpha_2 = -0.04$  and  $-0.06$ . (energy surface for  $\alpha_2 = 0.06$  in Fig. 5.7 b). The easy direction is  $[111]$  or  $[110]$  depending on  $\alpha_2$ . The energy difference between  $[111]$  and  $[100]$  is small for  $\alpha_2 < 0$ .

$\mathbf{k}_2$ , decreases for increasing  $\alpha_2$ . For  $\alpha_2 > 0$  the energy is increased in  $[111]$  direction. Thus, the energetic minimum is shifted towards the center. That is, the MES is compressed along  $\mathbf{m}$ . The  $\mathbf{k}_j$  tend to follow this deformation and its length shrinks, Chapter 5.3. As all  $\mathbf{k}_j$ 's deform due to the same deformation the unfavored  $\mathbf{k}_j$ 's also change. In Fig. 5.9 b) the two independent values of the deformation tensor in  $\mathbf{m}$  direction,  $d_0$ , and perpendicular to  $\mathbf{m}$ ,  $d_1$ , are shown. Thus, for  $\alpha_2 > 0$  the crystal expands in  $\mathbf{m}$  direction and slightly shrinks perpendicular to  $\mathbf{m}$ .

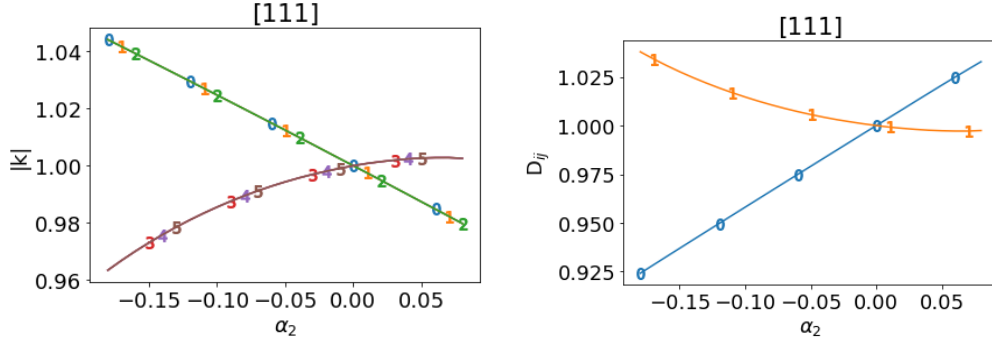


Figure 5.9: Deformation of the crystal due to magnetic coupling.  $\mathbf{m}$  is in  $[1\ 1\ 1]$  direction. Due to deformation of the MES the crystal shrinks in  $[1\ 1\ 1]$  direction and expands slightly perpendicular to  $\mathbf{m}$ .

### The FCC crystal

A similar analysis can be done for FCC crystals. A FCC crystal is described by two sets of k-vectors with different length scale, [70]:

$$\left\{ \frac{\mathbf{k}_j}{k_0} \right\} = \left\{ \begin{pmatrix} -1 \\ 1 \\ 1 \end{pmatrix}, \begin{pmatrix} 1 \\ -1 \\ 1 \end{pmatrix}, \begin{pmatrix} 1 \\ 1 \\ -1 \end{pmatrix}, \begin{pmatrix} -1 \\ -1 \\ -1 \end{pmatrix}, \begin{pmatrix} 2 \\ 0 \\ 0 \end{pmatrix}, \begin{pmatrix} 0 \\ 2 \\ 0 \end{pmatrix}, \begin{pmatrix} 0 \\ 0 \\ 2 \end{pmatrix} \right\} \quad (5.23)$$

The  $\mathbf{k}_j$ 's define a BCC lattice in k-space, Fig. 5.10. There are two sets of k-vectors.  $\mathbf{k}_{0-3}$  and  $\mathbf{k}_{4-6}$  differing by their length. The free energy in the amplitude expansion for the FCC crystal is often modified in order to account for the two length scales, [27, 86]:

$$\begin{aligned} \mathcal{F}[\{A_j\}] = & \int_{\Omega} \sum_{j=0}^3 B_0^x A_j^* \mathcal{G}_{0,j}^2 A_j + \sum_{j=4}^6 B_0^x A_j^* \mathcal{G}_{1,j}^2 A_j \\ & - \sum_{j=0}^6 \frac{3v}{2} |A_j|^4 + \frac{\Delta B_0}{2} A^2 + \frac{3v}{4} A^4 + f^s(\{A_j\}) \mathrm{d}\mathbf{r}, \end{aligned} \quad (5.24)$$

with  $\mathcal{G}_{m,j} \equiv \mathbf{q}_{m,j}^2 - \mathbf{k}_j^2 + \nabla^2 + 2i\mathbf{k}_j \cdot \nabla$  and  $q_{m,j}$  is the length of the related  $\mathbf{k}_j$ . This amplitude expansion is derived from PFC models with two or more

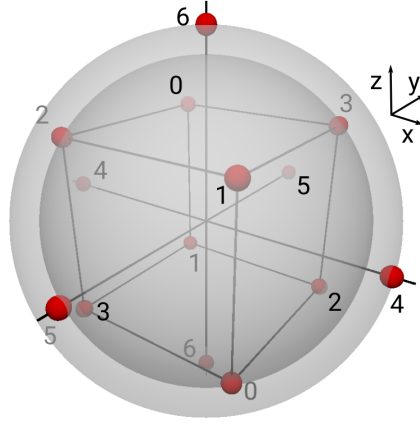


Figure 5.10: The numbered red balls symbolize the  $\mathbf{k}_j \in \{\mathbf{k}_j\}$  defining the FCC crystal. The  $\mathbf{k}_j$  are numbered according eq. 5.20. The energetic equivalent vectors,  $-\mathbf{k}_j$ , are numbered in grey. Due to symmetry of the crystals and magneto-structural interaction  $\mathbf{k}_j$  and  $-\mathbf{k}_j$  contribute equally to the total energy. The two length scales represented by  $\mathbf{k}_{0-3}$  and  $\mathbf{k}_{4-6}$  leads to two separate MES.

modes, e.g. [39, 53, 86, 88]. Here we assume  $\mathbf{q}_{0,j} = 1$  and  $\mathbf{q}_{1,j} = 2/\sqrt{3}$ . Thus, a FCC crystal with  $\mathbf{k}_0 = 1/\sqrt{3}$  will minimize the energy. Then the few mode approximation to the free energy including the simple magnetic coupling is:

$$\begin{aligned} \mathcal{F}(\{A_j\}, \{\mathbf{k}_j\}) &= \sum_{j=0}^3 A_j \left( (1 - \mathbf{k}_j^2)^2 + \alpha_2 (\mathbf{m}\mathbf{k})^2 \right) A_j \\ &+ \sum_{j=4}^6 A_j \left( \left(\frac{4}{3} - \mathbf{k}_j^2\right)^2 + \alpha_2 (\mathbf{m}\mathbf{k})^2 \right) A_j + g^{\text{FCC}}(\{A_j\}). \end{aligned} \quad (5.25)$$

$g^{\text{FCC}}(\{A_j\})$  is a structure dependent polynomial in  $\{A_j\}$  [70]:

$$\begin{aligned} g^{\text{FCC}}(\{A_j\}) &= - \sum_j \frac{3v}{2} |A_j|^4 + \frac{\Delta B_0}{2} A^2 + \frac{3v}{4} A^4 + f^{\text{FCC}}(\{A_j\}) \quad \text{and} \\ f^{\text{FCC}}(\{A_j\}) &= -2t[A_1^*(A_2^*A_5 + A_3^*A_7 + A_4^*A_6^*) + A_2^*(A_3^*A_6 + A_4^*A_7^*) \\ &+ A_3^*A_4^*A_5^* + c.c.] + 6v[A_1^*(A_2^*A_3^*A_4^* + A_2A_6^*A_7 + A_3A_5A_6^* \\ &+ A_4A_5A_7) + A_2^*A_5(A_3A_7^* + A_4A_6) + A_3^*A_4A_6A_7 + c.c.]. \end{aligned} \quad (5.26)$$

The coupling term is same for both length scales. Thus, every set of  $\mathbf{k}_j$  is controlled by a separate MES, see fig. 5.10. In fig. 5.11 a) and b) the MES for  $\mathbf{m}$

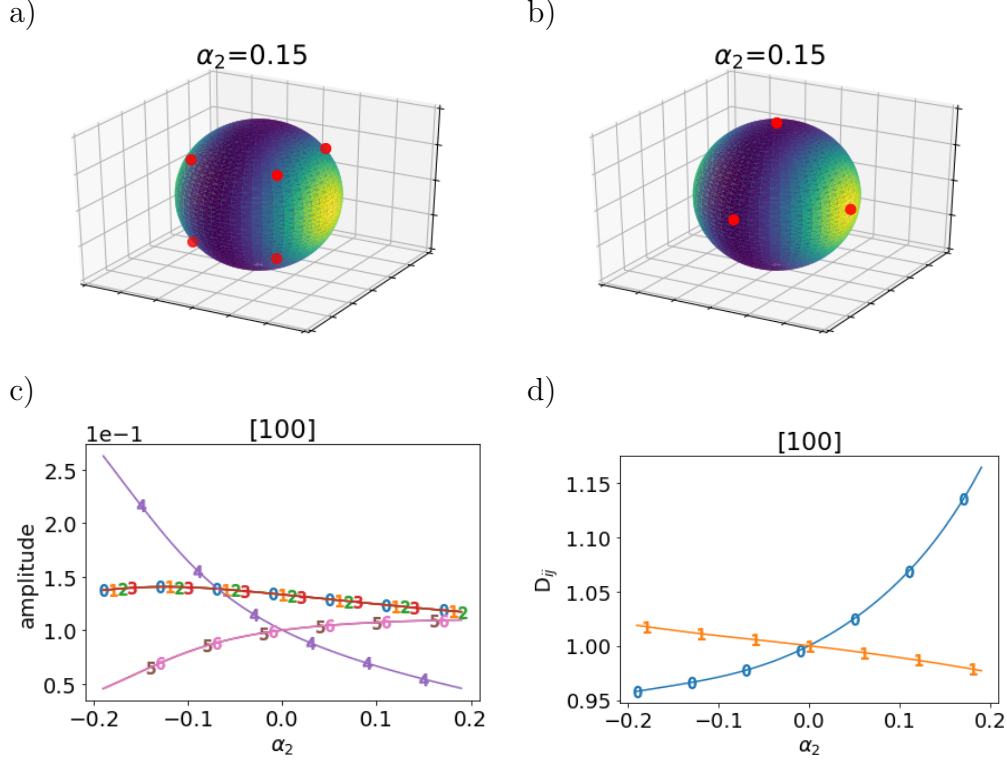


Figure 5.11: Symmetry breaking in the simple magnetic-structural coupling for a FCC crystal with  $\mathbf{m} \parallel [100]$ . a) MES of simple magneto-structural coupling for  $\mathbf{k}_{0-3}$ . a) MES of simple magneto-structural coupling for  $\mathbf{k}_{4-6}$ . The red balls indicate the  $\mathbf{k}_j$  defining the crystal structure in the FMA, eq. 5.23. c) Amplitudes  $A_j$  are shown for varying coupling strength  $\alpha_2$ . b) Deformation along and perpendicular of  $\mathbf{m}$ . Due to symmetry, there are groups of energetically equivalent  $\mathbf{k}_j$ 's. The numbering of  $A_j$  and  $\mathbf{k}_j$  follow fig. 5.10.

in  $[100]$  and  $\alpha_2 = 0.15$  is shown. The deformation of the MES is small and not visualized. The  $\langle 100 \rangle$  directions of the crystal are aligned with the x-,y- and z-axis.  $\mathbf{k}_{0-3}$  are on the corner of a cube. They are equally placed around the energetic maximum at the MES. That is, they are energetically equivalent. The MES of the other  $\mathbf{k}_j$ 's,  $\mathbf{k}_{4-6}$ , is similar, only the radius of the MES is adjusted, see fig. 5.11 b). The  $\mathbf{k}_j$ 's are at the x-,y- and z-axis. The minimum energetic

contribution is at the y-z-plane. Thus,  $\mathbf{k}_5$  and  $\mathbf{k}_6$  are energetically equivalent and have a minimum energy contribution.  $\mathbf{k}_4$  is a the energetic maximum at the MES. In fig. 5.11 c) the dependence of the amplitudes on the coupling strength are shown. Analogous to BCC, the amplitudes corresponding to energetically equivalent sets of  $\mathbf{k}_j$ 's are equal. Sets with larger energy contribution due to the MES have smaller amplitudes. The crystal expands in  $[100]$  direction for  $\alpha_2 > 0$  just as a BCC crystal. For BCC and FCC the MES is compressed in  $\mathbf{m}$  direction for  $\alpha_2 > 0$ . Thus,  $\mathbf{k}_j$ 's near the  $\mathbf{m}$  direction tend to shrink. The magnetic anisotropy is harder to predict a priori as there are more energetically sets of  $\mathbf{k}_j$  are involved in FCC and BCC.

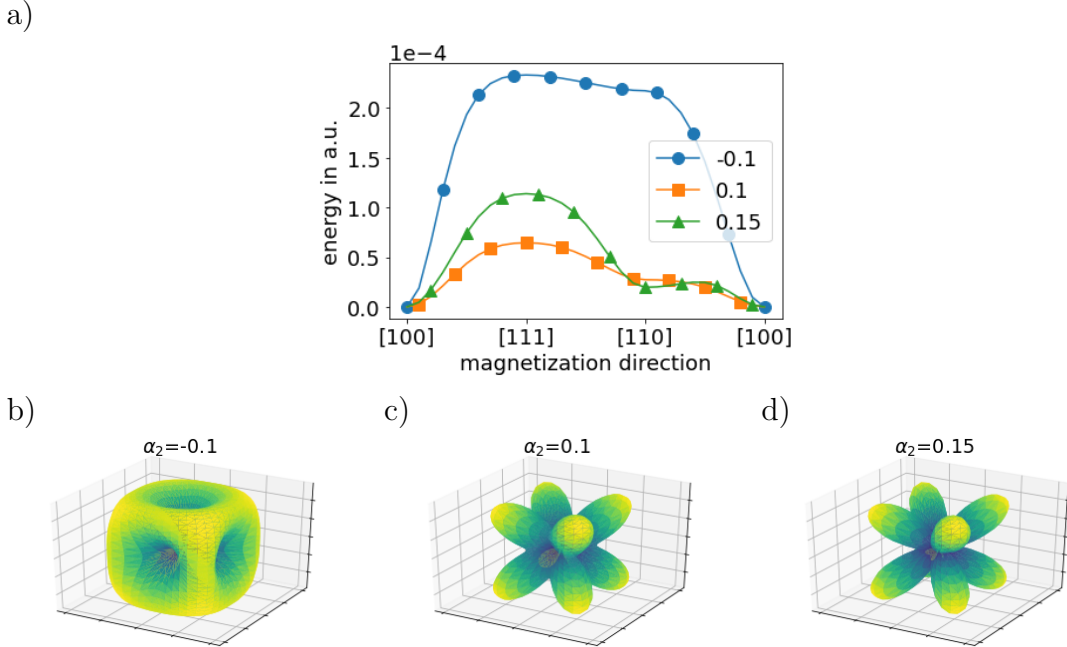


Figure 5.12: Comparing magnetic anisotropy for  $\alpha_2 = -0.1, 0.1$  and  $0.15$ . a) energy along the edges of the triangle defined by  $[100]$ ,  $[111]$  and  $[110]$ , Fig. 5.7 c). Maximum defines the hard direction and minimum the easy direction of magnetization. The energy is plotted relative to the minimum energy (easy direction). b)-d) magnetic anisotropy for FCC crystal.

In fig. 5.12 the influence of simplest magnetic coupling for  $\mathbf{m}$  in  $[100]$ ,  $[111]$

and  $[110]$  direction is shown for various coupling strength,  $\alpha_2$ . In all cases the  $\langle 100 \rangle$  direction is the easy direction. The hard direction is  $\langle 111 \rangle$ . For highly negative  $\alpha_2$  the  $\langle 110 \rangle$  becomes energetically comparable to  $\langle 111 \rangle$ . The magnetostriction and magnetic anisotropy increases with increasing  $|\alpha_2|$ . Thus, For FCC and simple magnetic coupling, the easy direction of magnetization can not be controlled. It is always  $\langle 100 \rangle$  for FCC structures.

### Limits of the simple coupling approach

In this chapter we showed that the MES can be used to analyze the magnetic coupling in PFC. The simplest magnetic coupling in PFC leads to a deformation of the MES and energetically preferred direction for single  $\mathbf{k}_j$ 's. The energy kernel defining the MES in PFC is an approximation to the  $C_2$  correlation function. It is rotational invariant in shape and energy contribution. The magnetic coupling breaks the rotational symmetry. Thus, the magnetic interaction can be interpreted as the breaking of symmetry of the correlation function due to magnetization. This breaking of symmetry leads to magnetic anisotropy and magnetostriction. In this simplest coupling magnetic anisotropy and magnetostriction are controlled by a single parameter and cannot be adapted independently. Also easy and hard direction of magnetization cannot be chosen freely. In BCC only  $\langle 111 \rangle$  and  $\langle 110 \rangle$  are possible easy directions, while in FCC only possible easy direction is  $\langle 100 \rangle$ . In the following we will extend the idea of an modified  $C_2$  correlation function and, thus, the MES, in order to get more independent control on magnetic anisotropy, on magnetostriction and on easy direction of magnetization.



### 5.4.2 Extended model

In the last chapter we showed that already the simple magnetic coupling leads to magnetic anisotropy and magnetostriction. Unfortunately, the easy or hard direction of magnetization in this model can not be controlled for BCC and FCC crystals. Thus, it is not possible to model two typical magnetic materials: iron and nickel. Iron is BCC and its easy(hard) direction of magnetization is  $[100]$  ( $[111]$ ). Nickel is FCC and its easy(hard) direction of magnetization is  $[111]$  ( $[100]$ ). Additionally, strength of magnetic anisotropy and magnetostriction is controlled by the same parameter. Thus, both properties can not be controlled independently. Larger magnetic anisotropy always leads to larger magnetostriction.

In this Chapter we extend the magneto structural coupling interaction in order to get a better control of the magnetic properties. An ideally controllable magnetic coupling without magnetostriction would not alter the shape of the MES. There are localized energetic minima at the MES for every  $\mathbf{k}_j$ . Then, if  $\mathbf{m}$  is in easy direction of magnetization every  $\mathbf{k}_j$  would be in an energetic minimum at the MES. In k-space this can be done by introducing localized gaussians reducing the energy at the appropriate positions at the MES. But this leads to non local PFC models with an integral Kernel analogous to the XMPFC model of Greenwood et al. [39]. In order to get better control and do not increase the complexity of the model, we propose an extended magnetic term:

$$\mathcal{F}_c(\varphi) = \int_{\Omega} \alpha_2 \varphi \left( \left( (q_m^2 + (m\nabla)^2)^2 + s \right) \varphi \right) \mathbf{dr}. \quad (5.27)$$

Thus, the free energy in few mode approximation for BCC crystals then reads:

$$\begin{aligned} \mathcal{F}(\{A_j\}, \{\mathbf{k}_j\}) &= \sum_j A_j \left[ (1 - \mathbf{k}_j^2)^2 + \alpha_2 (q_m^2 - (\mathbf{m}\mathbf{k}_j)^2)^2 + s \right] A_j \\ &+ g^{\text{BCC}}(\{A_j\}), \end{aligned} \quad (5.28)$$

The coupling term defines a double well in the direction of  $\mathbf{m}$ . At least at the cut of the planes defined by the extrema of this double well with the MES of PFC, the combined MES of magnetic PFC is not deformed. Thus there is no

magnetostriction due to  $\mathbf{k}_j$ 's there. The distance of this planes to the origin is controlled by  $\mathbf{q}_m$ . The mean impact of the extended coupling is controlled by the additional parameter  $s$ . In Fig. 5.13 we show the MES for  $\mathbf{q}_m =$  and  $\mathbf{m}$

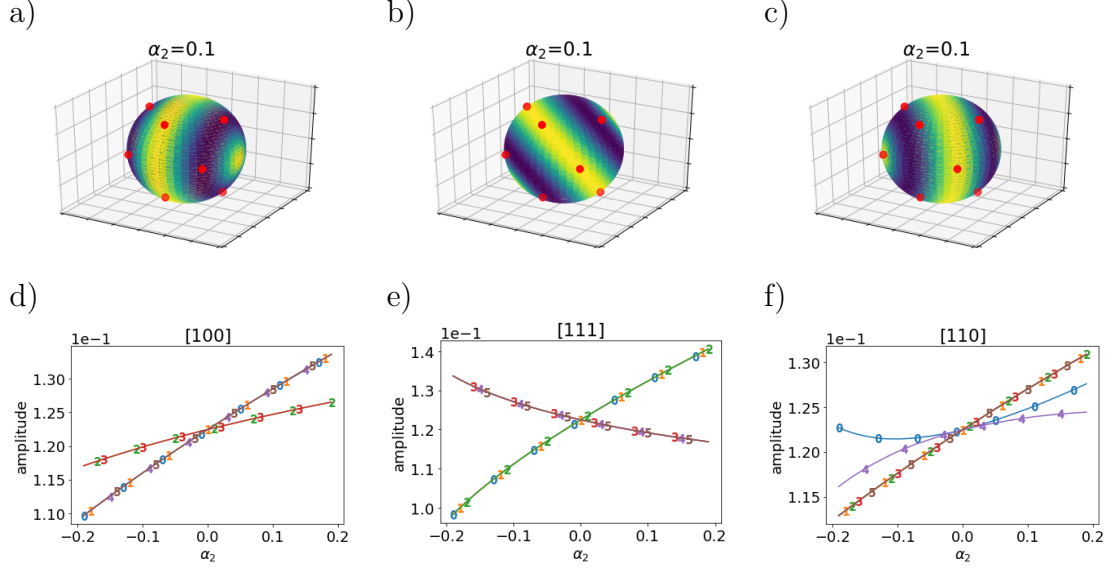


Figure 5.13: Symmetry breaking in the extended magnetic-structural coupling for BCC crystals.

in  $[100]$ ,  $[111]$  and  $[110]$  direction. The double well structure of the coupling leads to maximum energy contribution at a plane at the origin perpendicular to  $\mathbf{m}$ . A minimum energy contribution are at parallel planes also perpendicular  $\mathbf{m}$  at a distance of  $\mathbf{q}_m$  from the origin. At the point where  $\mathbf{m}$  cuts the MES a second energetic maximum occurs. Here  $\mathbf{q}_m$  is chosen to have the minimum energy contribution at the position of  $\mathbf{k}_0, \mathbf{k}_3, \mathbf{k}_4$  and  $\mathbf{k}_5$  for  $\mathbf{m}$  in  $[100]$  direction, Fig. 5.13 a). That is, the minimum energy at the MES is at the  $(100)$  plane of the FCC crystal in  $k$ -space defined by  $\{\mathbf{k}_j\}$ . The remaining  $\mathbf{k}_j$ 's are at the energetic maximum at the MES. If  $\mathbf{m}$  is in  $[111]$  direction,  $\mathbf{k}_{3-5}$  are at energetic maximum and  $\mathbf{k}_{0-2}$  are placed equally around the second energetic maximum in  $[111]$  direction. There are three sets of energetically equivalent  $\mathbf{k}_j$ 's for  $\mathbf{m}$  in  $[110]$  direction, see Fig. 5.13 c). In all cases, the amplitude corresponding to energetically  $\mathbf{k}_j$ 's are equal and shrink for larger energy contribution.

In Fig. 5.14 the deformation due to the extended magneto structural coupling

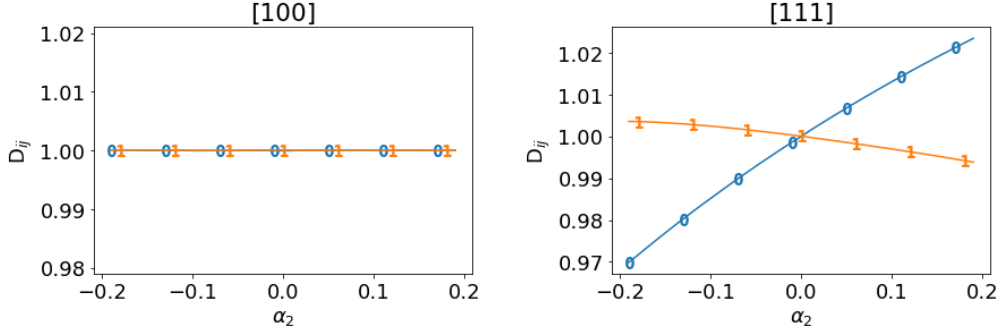


Figure 5.14: Deformation of the crystal due to magnetic coupling.  $\mathbf{m}$  is in  $[1\ 1\ 1]$  direction. Due to deformation of the MES the crystal shrinks in  $[1\ 1\ 1]$  direction and expands slightly perpendicular to  $\mathbf{m}$ .

is shown. For  $\mathbf{m}$  in  $[1\ 0\ 0]$  direction there is no deformation. That is, there is no magnetostriction. The coupling is especially constructed in a way, that all  $\mathbf{k}_j$ 's are on some energetic extrema on the MES. At this extrema there is no deformation to the spherical MES. Thus, there is no driving force for a single  $\mathbf{k}_j$  to change direction or length and no deformation occurs. This clearly holds only for  $\mathbf{m}$  in  $[1\ 0\ 0]$  direction. If  $\mathbf{m}$  is in  $[1\ 1\ 1]$  direction, see Fig. 5.14 b),  $\mathbf{k}_{0-2}$  are not at an energetic extrema. There is a force toward the energetic minimum. Thus, an expansion of the crystal along  $\mathbf{m}$  is expected for  $\alpha_2 > 0$  and shown in Fig. 5.14 b). Variation of  $\mathbf{q}_m$  can be used to control magnetostriction. Increasing  $\mathbf{q}_m$  may increase magnetostriction in  $[1\ 0\ 0]$  direction and decrease magnetostriction in  $[1\ 1\ 1]$  direction.

In Fig. 5.15 the magnetic anisotropy for different coupling strength are shown. The easy direction of magnetization is  $[1\ 0\ 0]$  for  $\alpha_2 > 0$ . The hard direction is  $[1\ 1\ 1]$ . The magnetic anisotropy increases with increasing  $\alpha_2$ .  $\alpha_2 < 0$  reverses the situation.  $[1\ 0\ 0]$  becomes the easy direction and  $[1\ 1\ 1]$  the hard direction. Thus, the total energy is dominated by  $\mathbf{k}_{0-3}$ . For  $\alpha_2 > 0$  and  $\mathbf{m}$  in  $[1\ 0\ 0]$  direction  $\mathbf{k}_{0-3}$  are at an energetic minimum at the MES. For  $\alpha_2 < 0$  they are at an energetic maximum.

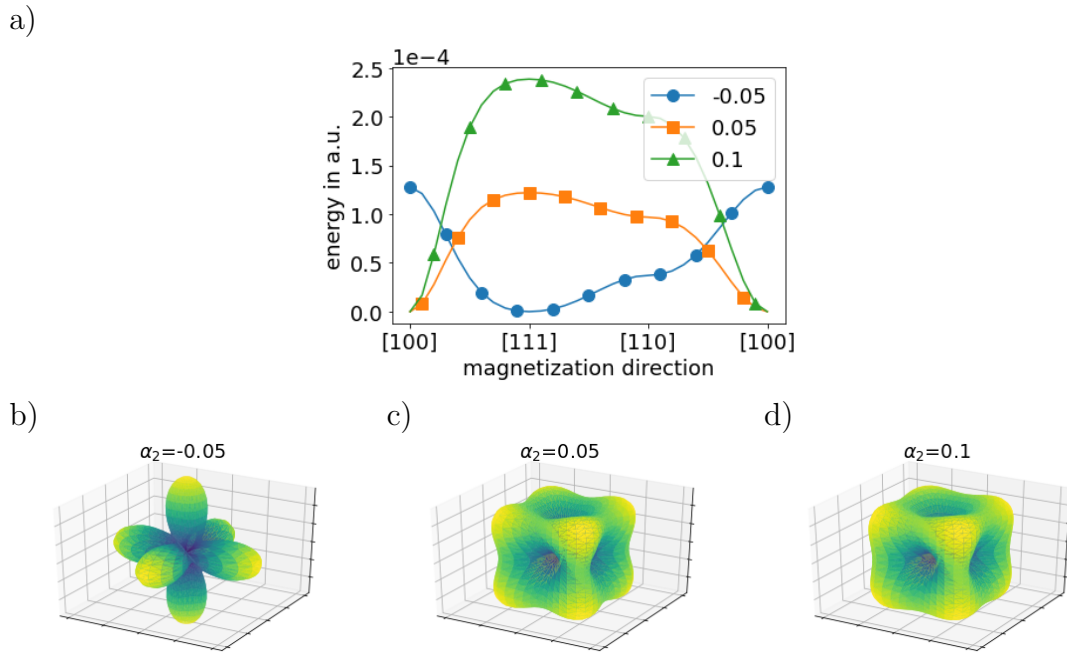


Figure 5.15: Comparing magnetic anisotropy for  $\alpha_2 = -0.05$ ,  $0.05$  and  $0.1$  and a BCC crystal. a) energy along the edges of the triangle defined by  $[100]$ ,  $[111]$  and  $[110]$ , Fig. 5.7 c). Maximum defines the hard direction and minimum the easy direction of magnetization. The energy is plotted relative to the minimum energy (easy direction). b)-d) energy surface for  $\alpha_2 = -0.05$ ,  $0.05$  and  $0.1$ . The easy direction is  $[111]$  for  $\alpha_2 = -0.05$  and  $[100]$  otherwise.

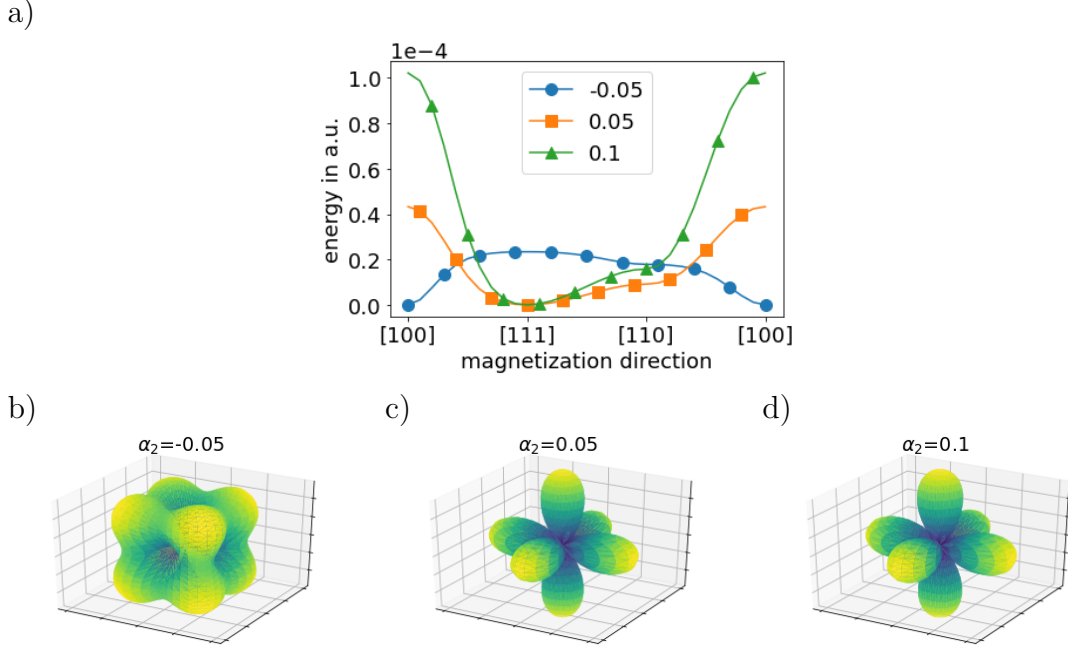


Figure 5.16: Comparing magnetic anisotropy for  $\alpha_2 = -0.05, 0.05$  and  $0.1$  and a FCC crystal. a) energy along the edges of the triangle defined by  $[100]$ ,  $[111]$  and  $[110]$ , Fig. 5.7 c). Maximum defines the hard direction and minimum the easy direction of magnetization. The energy is plotted relative to the minimum energy (easy direction). b)-d) energy surface for  $\alpha_2 = -0.05, 0.05$  and  $0.1$ . The easy direction is  $[100]$  for  $\alpha_2 = -0.05$  and  $[111]$  otherwise.

For FCC crystals there is no such easy way to choose  $\mathbf{q}_m$  due to the two involved length scales in  $\{\mathbf{k}_j\}$ . We adapt the extended coupling model to the two length scales involved in the modeling of FCC crystals. We choose for  $\mathbf{q}_{0,m} = 1/\sqrt{3}$  for  $\mathbf{k}_{0-3}$  and  $\mathbf{q}_{1,m} = 1/\sqrt{2}$  for  $\mathbf{k}_{4-6}$ . In Fig. 5.16 the magnetic anisotropy is shown for various  $\alpha_2$ . With this set of parameters it is possible to control the hard and easy direction of magnetization. For  $\alpha_2 > 0$  the easy axis of magnetization is  $[111]$  and the hard direction is  $[100]$ .

Here we introduced the extended magnetic coupling for PFC. Our proposed extension does the complexity of the magnetic PFC model significantly. That is, the order of the PDE defining the evolution of the density wave is not increased.

The energy contribution due to the extended coupling term describes a double well in k-space perpendicular to magnetization. That is, the local extrema of the energy contribution are on planes perpendicular to magnetization,  $\mathbf{m}$ , and a distance dependent on  $\mathbf{q}_m$ . With this model the easy direction of FCC and BCC crystals can be controlled. The easy direction can be switched between  $\langle 100 \rangle$  and  $\langle 111 \rangle$ . Thus, a magnetic model for basic magnetic materials, Iron (BCC) and Nickel (FCC), can be formulated, which was not possible in the simple coupling model.

Additionally,  $\mathbf{q}_m$  is directly connected to the magnetostriction.  $\mathbf{q}_m$  defines the position of the local extrema of the energy contributions due to the coupling in k-space. If this is chosen, such that all  $\mathbf{k}_j$  of the undisturbed crystal are at this extrema, then the MES at this position does not deform and there is no magnetostriction induced in this situation. Small changes in  $\mathbf{q}_m$  will induce a force on the  $\mathbf{k}_j$  and lead to magnetostriction.

### 5.4.3 Summary

The simple and extended magnetic coupling has analyzed with the help of the MES. The MES visualize the minimum energy contribution of a single  $\mathbf{k}_j$  defining the crystal. The magnetic coupling break the rotational symmetry of MES and, thus, leads to magnetic anisotropy and magnetostriction. Using simple magnetic coupling the hard direction of magnetization is always  $\langle 111 \rangle$  for BCC crystals and  $\langle 111 \rangle$  FCC crystals. Thus, it is not possible to model the basic magnetic materials Iron (BCC) and Nickel (FCC) with the simple magnetic coupling. Additionally, the magnetic anisotropy and magnetostriction are controlled both by the coupling strength,  $\alpha_2$ . They are strongly correlated and can not be controlled independently.

The extended magnetic coupling model overcome this restrictions without increasing the complexity significantly. It describes a double well in direction of magnetization in k-space. Thus, the local extrema of the double well can be chosen freely and the energy contribution at the MES is changed without deformation of its shape. This property of the extended magnetic coupling gives additional flexibility to adapt the magnetostriction. In some cases, when all  $\mathbf{k}_j$ 's

are at local extrema of the extended magnetic coupling, the magnetostriction vanishes.

The extended magnetic coupling only introduces directional derivatives of order four and thus does not increase the order of the model. Thus, an implementation does not increase complexity of the numerical model. The expansion in directional derivatives gives us the possibility to define a MES. The anisotropy in energy and shape of the MES can be used to understand the impact of the magneto structural coupling and develop further magnetic coupling terms in order to fit your needs.

## 5.5 Magneto-structural coupling in APFC

In the preceding chapters magneto-structural interaction was introduced in PFC modeling. We analyzed the simplest approach proposed by Seymour et al. [72] and the extension proposed section 5.4.2. In the following, the magneto-structural interaction is introduced in the amplitude expansion of PFC. We still assume the limit of strong external magnetic fields, Chapter 3. That is, the magnetization  $\mathbf{m}$  is perfectly aligned by the external magnetic field and constant in space. The developed magnetic APFC model is applied to study the influence of strong magnetic fields on grain shrinkage in 3-D at the end of this chapter.

The considered coupling terms of the simple and extended model are both quadratic in the density. Thus, the amplitude is easily done equivalently to the other quadratic terms. It leads to additional terms independent on the reference structure of the amplitude expansion, chap. 5.2. Assuming the PFC energy eq. 5.1, the APFC with magneto-structural coupling is:

$$\mathcal{F}[\{A_j\}] = \int d\mathbf{r} \sum_j A_j^* B_0^x [\mathcal{G}_j^2 + \alpha_2 (\mathcal{M}_j^2 + s)] A_j + g^S(\{A_j\}) \quad (5.29)$$

with

$$\begin{aligned} \mathcal{M}_j &= \mathbf{i} \mathbf{m} \cdot \mathbf{k}_j + \mathbf{m} \cdot \nabla \quad \text{and } s = 0 \quad \text{for simple model and} & (5.30) \\ \mathcal{M}_j &= q_m^2 + (\mathbf{i} \mathbf{m} \cdot \mathbf{k}_j + \mathbf{m} \cdot \nabla)^2 \quad \text{and } s = \mathbf{q}_m^4 \quad \text{for extended model.} \end{aligned}$$

$q_m$  is an additional parameters in the extended magnetic coupling in order to have better control of the magneto-structural interaction, chap. 5.4.2. The coupling terms have the same structure as the first term in the energy eq. 5.29 due to the approximation of the correlation function in PFC.  $g^S$  is again the structure dependent and deformation independent part of the energy and does not change by introducing the magnetic coupling. For BCC and FCC it is listed in eq. 5.22 and eq. 5.26. Then, assuming a long wave length limit [88], the dynamic



equation is written as:

$$\frac{\partial A_j}{\partial t} = -|\mathbf{k}_j|^2 \frac{\delta \mathcal{F}[\{A_j\}]}{\delta A_j^*} = -|\mathbf{k}_j|^2 \left[ B_0^x (\mathcal{G}_j^2 + \alpha_2 \mathcal{M}_j^2) A_j + \hat{s} A_j + \frac{\partial g^S(\{A_j\})}{\partial A_j^*} \right], \quad (5.31)$$

with  $\hat{s} = B_0^x \alpha_2 s$ . The proposed magnetic coupling does not increase the order of the partial differential equation. That is, the magnetic coupling does not increase the complexity of the equation significantly. This property was a key idea in the development of the extended magnetic coupling. The coupling terms and the first terms in energy eq. 5.29 have a similar structure. This is exploited in the discretization scheme by using operator splitting to avoid differential operators of degree four or higher [70]. The differential operator  $(\mathcal{G}_j^2 + \alpha_2 \mathcal{M}_j^2)$  is written as a product of two linear second order operators:

$$(\mathcal{G}_j^2 + \alpha_2 \mathcal{M}_j^2) = (\mathcal{G}_j - \mathbf{i}\sqrt{\alpha_2} \mathcal{M}_j)(\mathcal{G}_j + \mathbf{i}\sqrt{\alpha_2} \mathcal{M}_j) =: \mathcal{N}_j^+ \mathcal{N}_j^-. \quad (5.32)$$

Thus the operator splitting reads:

$$\begin{aligned} \frac{\partial A_j}{\partial t} &= -|\mathbf{k}_j|^2 \left[ B_0^x \mathcal{N}_j^+ \mu_j + \hat{s} A_j + \frac{\partial f^S(\{A_j\})}{\partial A_j^*} \right], \\ \mu_j &= \mathcal{N}_j^- A_j. \end{aligned} \quad (5.33)$$

The linear operators  $\mathcal{N}_j^+$  and  $\mathcal{N}_j^-$  are of second order and can be easily implemented with FEM in AMDiS [70, 82]. A semi-implicite time discretisation scheme is used.

We examine the influence of magnetization on the shrinkage of a initially spherical grain. A spherical region is cut from a otherwise perfect BCC crystal, the matrix, Fig. 5.17. The spherical region is rotated by  $5^\circ$  around the  $[101]$  direction of crystal in the matrix. That is, the rotation axis is the z-axis in our frame. Fig. 5.17 b) visualize the cubic unit cell of crystal in the matrix. When the magnetization direction varies along the line defined by  $[0\bar{1}1]$ ,  $[001]$  and  $[011]$ , the free energy of the matrix and grain varies, Fig. 5.17 c). For the matrix there are energetic maxima for  $\mathbf{m}$  in  $\langle 011 \rangle$  directions and an energetic minima for

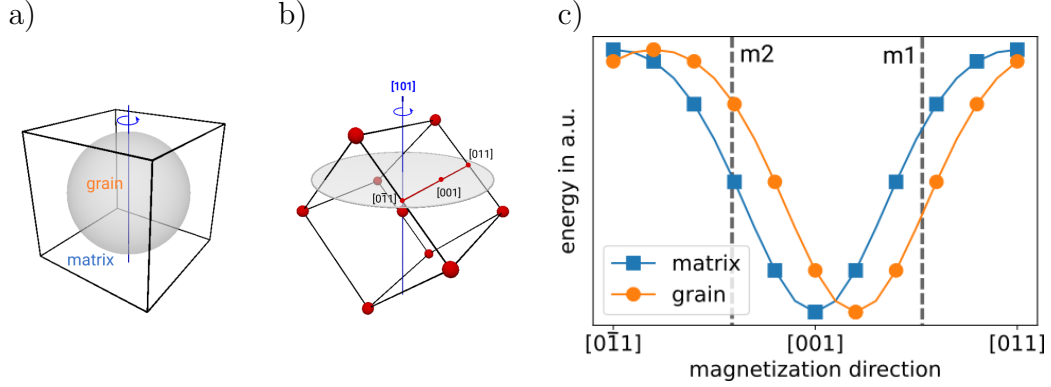


Figure 5.17: Set up for magnetic APFC simulation. a) A spherical grain is constructed by cutting a sphere in a BCC crystal (matrix) and rotating the sphere by  $5^\circ$ . b) The  $[101]$  direction of the grain and matrix is aligned with the axis of rotation. The direction of magnetization is defined w.r.t the matrix. c) Sketch of magnetic anisotropy of matrix and grain along the line defined by  $[0\bar{1}1]$ ,  $[001]$  and  $[011]$ . For small rotations the magnetic anisotropy in grain and matrix are similar. But magnetic anisotropy of the grain is shifted due to rotation. Maximum energy difference between grain and matrix is achieved for magnetization between easy and hard directions (m1,m2). Additionally a set up with magnetization in  $[101]$  direction is used (m0), which does not prefer grain or matrix.

$\langle 001 \rangle$  direction, Fig. 5.17 c). The grain is rotated and the same magnetization leads to an slightly shifted easy direction. Thus, dependent on the direction of  $\mathbf{m}$  the energy difference of grain and matrix varies. In order to maximize the energy difference  $\mathbf{m}$  is chosen between the energetic extrema. The matrix is energetically preferred for  $\mathbf{m}$  between  $[0\bar{1}1]$  and  $[001]$ , (m2). The grain is energetically preferred for  $\mathbf{m}$  between  $[001]$  and  $[011]$ , (m1). No preference of grain or matrix is achieved by choosing  $\mathbf{m}$  along the axis of rotation of the grain,  $[101]$ , (m0).

Fig. 5.18 shows the grain shrinkage for the case m0. The grain shrinks anisotropically as already discussed in section 5.2 or in [69] in more detail. In all three simulations the grain structure does not vary significantly. That is, the defect network for grains of the same size are nearly independent on the orientation of  $\mathbf{m}$ . But the speed of shrinkage is greatly influenced by  $\mathbf{m}$ .

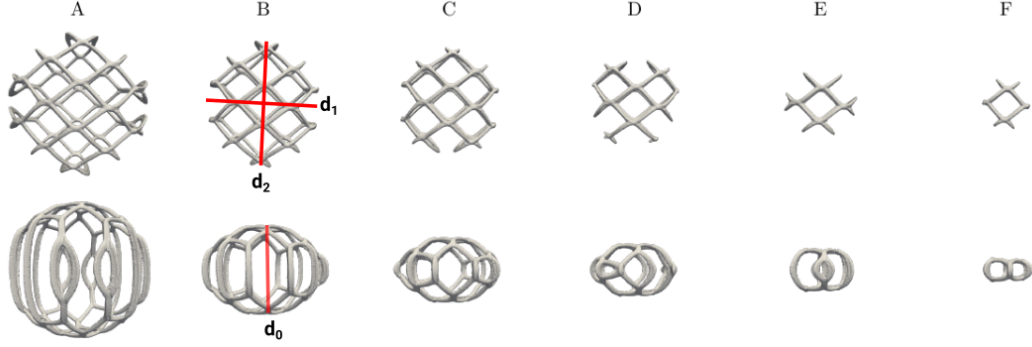


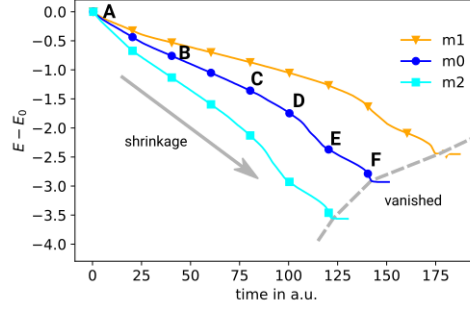
Figure 5.18: Defect network of an initially spherical grain in a BCC crystal, Fig. 5.17. A-E) are snapshots taken at times indicated in Fig. 5.19. The magnetization is aligned with the axis of rotation ( $m_0$ ). The diameter  $d_{0-2}$  are introduced to define the shape of the grain.

In Fig. 5.19 a) the energy decay during shrinkage of the grain is shown. The energy decay is shown relative to the initial energy. When the grain vanished the energy becomes constant. This defines the vanishing time  $t_v$ . The slowest shrinkage is achieved if the grain is energetically preferred. The energy gain during shrinkage is the lowest as the grain has lower energy than the matrix. The highest shrinkage speed and energy gain is observed when the grain has higher energy than the matrix. If matrix and grain are energetically equivalent, the vanishing time is between the other two cases. Thus, the magnetization enhance or hinder the grain shrinkage. In order to study the grain evolution in more detail the area of the grain and the different diameters,  $d_{0-2}$ , are shown in Fig. 5.19 b) and c). The area of the grain boundary is approximated by the Knud-Thomsen formular:

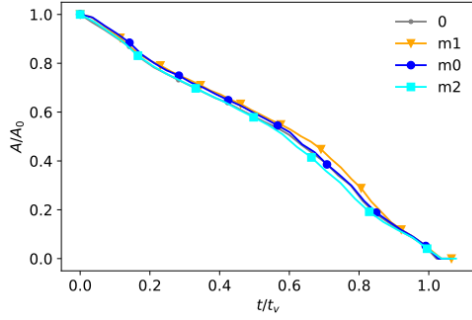
$$A = \frac{\pi}{3^{1/p}} ((d_0 d_1)^p + (d_1 d_2)^p + (d_0 d_2)^p)^{1/p} \quad (5.34)$$

with  $p=1.6075$  and  $d_{0-2}$  the extension of the grain in x,y and z-direction. Fig. 5.19 b) shows the decay of the grain boundary area over time. The time is scaled by the vanishing time and the area with the initial area. In all simulations the area decreases nearly linear. A linear decrease in energy was predicted by classical theory of grain shrinkage [25] and reproduced by PFC and APFC

a)



b)



c)

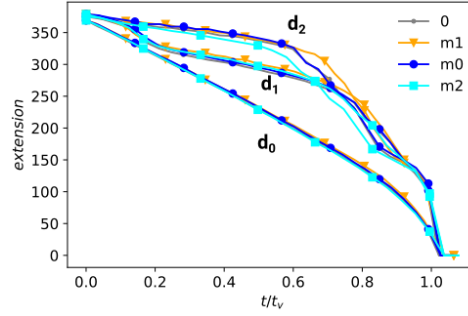


Figure 5.19: Influence of magnetization on grain shrinkage. For  $m_0$  there is no difference in bulk energy of grain and matrix.  $m_1$  leads to lower energy of the grain and  $m_2$  leads to lower energy of the matrix. a) Energy decay during shrinkage. Dependent on magnetization the grain vanishes at different times  $t_v$ . b) Area shrinkage normalized by the initial area and vanishing time  $t_v$ . c) Shape evolution shown by the shrinkage of the different diameters  $d_{0-2}$ , see Fig. 5.18.

without magnetic interaction [69, 87]. This indicates that the evolution is still mainly governed by the minimization of grain boundary energy. Nevertheless, the magnetic anisotropy may enhance or hinder the evolution. A closer look of the shape evolution is shown in Fig. 5.19 c). Here, the evolution of the diameters  $d_{0-2}$  are shown.  $d_0$  shrinks nearly linear at the beginning. The shrinkage speeds up at the end,  $t/t_v > 0.9$ . The evolution  $d_1$  and  $d_2$  is not as simple. There are some steps and intervals of different shrinkage rate. This steps can be connected to vanishing defect lines, which greatly influence the grain boundary. That is, in the interval  $0.6 < t/t_v < 0.8$  indicated by C-E in Fig. 5.18 dislocation lines

defining the grain vanishes and change structure of the grain boundary. This leads to an increased shrinkage rate in this directions. This can also be identified in the decay of energy and grain boundary surface. The rate of decay changes slightly in this interval. The evolution of  $d_{0-2}$  is nearly the same for all three cases. This also shows, that the shape of the grain depends on size but not on the magnetization.

## 5.6 Summary

In APFC the density wave is expanded in its most important modes. The amplitudes of the modes encode the deviation to a priori chosen reference crystal. This deviations varies mostly on a much larger length scale than the particle distance defining the density wave of PFC. Thus, the amplitudes can be discretized on a much coarser grid and computation of much larger domains and three dimensional set ups become numerically feasible. The amplitudes vary at a length scale comparable to the particle distance only at defects. This is treated by adaptively refined grids in our FEM discretization.

We define the MES in order to analyze the magneto structural coupling. The MES represent the energy contribution due to the isotropic correlation function and the magnetic coupling in k-space. The magnetic coupling term breaks the rotational symmetry of the MES, which leads to magnetic anisotropy and magnetostriction in the PFC model. In order to adapt a magnetic PFC model for iron (BCC) or nickel (BCC) the extended magnetic coupling model is developed. With this new model the easy and hard direction of magnetization in BCC and FCC crystals can be chosen freely. Furthermore, it introduces larger flexibility to adapt magnetic anisotropy and magnetostriction.

The proposed magneto structural coupling does not increase the complexity of the model significantly. The amplitude expansion of the magnetic PFC is used to show the impact of magnetic anisotropy on the shrinkage of an initially spherical grain. The shrinkage of the grain can be hindered or enhanced dependent on the direction of the magnetization.

Thus, the extended magnetic coupling paves the way to modeling of different magnetic materials in PFC. The MES visualizes the impact of the magneto

structural coupling and is a tool to develop further extensions of the magneto structural coupling.

## 6 | Conclusion

Electromagnetic fields can be used to tailor microstructures and, thus, properties of materials, by controlling grain growth. Grain growth in multicrystalline thin films is quite complex and not fully understood. Simple models merely based on grain boundary energies can not explain the grain size and shape distribution found in experiment. In this work we use phase field crystal (PFC) models to study the influence of magnetic fields on grain growth and coarsening. PFC is based on an energy dependent on the local ordering in the crystal. It defines the ordering on an atomic scale. The time evolution is treated on diffusive time scales. Thus, long time simulation of coarsening is feasible. PFC naturally includes grain boundaries, defects and elastic effects. In Chapter 2 we showed that PFC can reproduce the grain size distribution and stagnation of coarsening in thin films. Large scale simulations are done using pseudo spectral discretization of the PFC model.

In Chapter 3 and 4 we used an extension of PFC to include magneto-structural interaction. A strong external magnetic field and magnetic anisotropy of the model leads to grain selection during coarsening. Grains with their easy direction aligned preferably to the external magnetic field grow preferably. This expected result was also seen in experiment. In our simulation we also see, that growing crystals often elongate perpendicular to the magnetization. This unexpected result can be explained by an anisotropic mobility of grain boundaries due to the local magnetization in our model. Long time simulations showed different coarsening regimes, Chapter 4. We identified a coarsening regime, where the scaling exponent is dependent the magnetic driving force. Additionally, stagnation can be prevented by a high magnetic driving force. This effects are most likely due to kinetic effects. the local magnetization may increase the mobility of the defect in the magnetic PFC model.

In the last chapter we introduce the magneto-structural coupling in the amplitude expansion of PFC (APFC). This approach tackles two problems of the magnetic PFC model used in Chapter 2-4.

Firstly, APFC depends on fields (amplitudes) mostly varying on a much larger length scale than PFC. Variations on the length scale of particles only occur at defects. We use a finite element discretization using adaptive grids. Thus, large scale simulations in three dimensions become feasible at least for small angle grain boundaries.

Secondly, magneto-structural coupling is extended in order to adapt the model to typical magnetic materials, e.g. iron or nickel. The simple magneto-structural coupling used in Chapter 2-4 has not the flexibility to adapt qualitatively to this materials. We developed an extended magneto-structural coupling, which can be adapted to iron and nickel. The extension is specifically constructed to not increase the complexity of the numerical model. This extension is introduced also in the APFC model. With the magnetic APFC model we study the influence of magnetic fields on the shrinkage of a single grain. The shrinkage is enhanced or hindered depending on the direction of the magnetization.

In summary, we believe that PFC models are a versatile tool to examine grain growth and coarsening. The classical PFC model is easily solved with spectral methods. But as more complex PFC models become necessary, efficient real space methods are needed. APFC models can be seen as a method to solve PFC on a larger length scale. This models have great potential to close the gap between atomistic and continuum simulations in nanotechnology. However, the properties of PFC and APFC are not easily analysed and adapted to a material. Our proposed magneto-structural coupling is the simplest approach to adapt the magnetic properties of PFC and APFC to real materials. Large scale simulation depend on efficient numerical models. Finite elements on adaptive grids are well suited to exploit the properties of APFC.



# References

- [1] A. Adland, Y. Xu, and A. Karma. “Unified theoretical framework for polycrystalline pattern evolution”. In: *Phys. Rev. Lett.* 110 (2013), p. 265504.
- [2] J. B. Allen. “Simulations of Anisotropic Texture Evolution on Paramagnetic and Diamagnetic Materials Subject to a Magnetic Field Using Q-State Monte Carlo”. In: *Journal of Engineering Materials and Technology* 138.4 (2016), p. 041012.
- [3] S. Angenent and M. E. Gurtin. “Multiphase thermomechanics with interfacial structure 2. Evolution of an isothermal interface”. In: *Arch. Rat. Mech. Anal.* 108.3 (1989), pp. 323–391.
- [4] B. P. Athreya, N. Goldenfeld, and J. A. Dantzig. “Renormalization-group theory for the phase-field crystal equation”. In: *Phys. Rev. E* 74.1 (2006), p. 011601.
- [5] B. P. Athreya, N. Goldenfeld, J. A. Dantzig, M. Greenwood, and N. Provatas. “Adaptive mesh computation of polycrystalline pattern formation using a renormalization-group reduction of the phase-field crystal model”. In: *Phys. Rev. E* 76 (2007), p. 056706.
- [6] R. Backofen, K. Barmak, K. R. Elder, and A. Voigt. “Capturing the complex physics behind universal grain size distributions in thin metallic films”. In: *Acta Mater.* 64 (2014), p. 72.
- [7] R. Backofen, K. R. Elder, and A. Voigt. “Controlling Grain Boundaries by Magnetic Fields”. In: *Physical Review Letters* 122.12 (2019), p. 126103.
- [8] R. Backofen, A. Rätz, and A. Voigt. In: *Phil. Mag. Lett.* 87 (2007), p. 813.
- [9] R. Backofen and A. Voigt. “Magnetically induced/enhanced coarsening in thin films”. In: *Physical Review Materials* 4.2 (2020), pp. 1–7.

- [10] R. Backofen and A. Voigt. “Solid–liquid interfacial energies and equilibrium shapes of nanocrystals”. In: *Journal of Physics: Condensed Matter* 21.46 (2009), p. 464109.
- [11] R. Backofen, M. Gräf, D. Potts, S. Praetorius, A. Voigt, and T. Witkowski. “A continuous approach to discrete ordering on  $S^2$ ”. In: *Multiscale Modeling & Simulation* 9.1 (2011), pp. 314–334.
- [12] R. Backofen and A. Voigt. “A Phase Field Crystal Study of Heterogeneous Nucleation-Application of the String Method”. In: *Eur. Phys. J. Special Topics* 223 (2014), pp. 497–509.
- [13] R. Backofen and A. Voigt. “A phase-field-crystal approach to critical nuclei”. In: *Journal of Physics: Condensed Matter* 22.36 (2010), p. 364104.
- [14] R. Backofen, A. Voigt, and T. Witkowski. “Particles on curved surfaces: A dynamic approach by a phase-field-crystal model”. In: *Physical Review E* 81.2 (2010), p. 025701.
- [15] K. Barmak, E. Eggeling, D. Kinderlehrer, R. Sharp, S. Ta’asan, A. Rollett, and K. Coffey. “Grain growth and the puzzle of its stagnation in thin films: The curious tale of a tail and an ear”. In: *Prog. Mat. Sci.* (<http://dx.doi.org/10.1016/j.pmatsci.2013.03.004>).
- [16] K. Barmak, J. Kim, C. Kim, W. Archibald, G. Rohrer, A. Rollett, D. Kinderlehrer, S. Ta’Asan, H. Zhang, and D. Srolovitz. “Grain boundary energy and grain growth in Al films: Comparison of experiments and simulations”. In: *Scr. Mater.* 54 (2006), p. 1059.
- [17] L. A. Barrales-Mora, V. Mohles, P. J. Konijnenberg, and D. A. Molodov. “A novel implementation for the simulation of 2-D grain growth with consideration to external energetic fields”. In: *Computational Materials Science* 39.1 SPEC. ISS. (2007), pp. 160–165.
- [18] J. Berry, M. Grant, and K. R. Elder. “Diffusive atomistic dynamics of edge dislocations in two dimensions”. In: *Physical Review E - Statistical, Nonlinear, and Soft Matter Physics* 73.3 (2006), pp. 1–12.

- 
- [19] J. Berry, N. Provatas, J. Rottler, and C. W. Sinclair. “Defect stability in phase-field crystal models: Stacking faults and partial dislocations”. In: *Physical Review B - Condensed Matter and Materials Physics* 86.22 (2012), pp. 1–12.
- [20] J. Berry, N. Provatas, J. Rottler, and C. W. Sinclair. “Phase field crystal modeling as a unified atomistic approach to defect dynamics”. In: *Phys. Rev. B* 89.21 (June 2014), p. 214117.
- [21] M. Bjerre, J. Tarp, L. Angheluta, and J. Mathiesen. “Rotation induced grain growth and stagnation in phase-field crystal models”. In: *Phys. Rev. E* 88 (2013), p. 020401.
- [22] D. Boyer and J. Vinals. “Weakly nonlinear theory of grain boundary motion in patterns with crystalline symmetry”. In: *Phys. Rev. Lett.* 89 (2002), p. 055501.
- [23] J. Cahn and J. Taylor. “A unified approach to motion of grain boundaries, relative tangential translation along grain boundaries and grain rotation”. In: *Acta Mater.* 52 (2004), p. 4887.
- [24] S. Chiu. “Aboav-Weaire’s and Lewis’ laws - a review”. In: *Material Characterization* 34 (1995), pp. 149–165.
- [25] R. Doherty, D. Hughes, F. Humphreys, J. Jonas, D. Jensen, M. Kassner, W. King, T. McNelley, H. McQueen, and A. Rollett. “Current issues in recrystallization: a review”. In: *Mater. Sci. Eng. A* 238.2 (Nov. 1997), pp. 219–274.
- [26] K. R. Elder and Z.-F. Huang. “A phase field crystal study of epitaxial island formation on nanomembranes”. In: *J. Phys. Condens. Matter* 22 (2010), p. 364103.
- [27] K. R. Elder, Z.-F. Huang, and N. Provatas. “Amplitude expansion of the binary phase-field-crystal model”. In: *Phys. Rev. E* 81 (2010), p. 011602.
- [28] K. R. Elder, G. Rossi, P. Kanerva, F. Sanches, S.-C. Ying, E. Granato, C. V. Achim, and T. Ala-Nissila. “Modeling self-organization of thin strained metallic overlayers from atomic to micron scales”. In: *Phys. Rev. B.* 88 (2013), p. 075423.
-

- [29] K. R. Elder, G. Rossi, P. Kanerva, F. Sanches, S.-C. Ying, E. Granato, C. V. Achim, and T. Ala-Nissila. “Patterning of heteroepitaxial overlayers from nano to micron scales”. In: *Phys. Rev. Lett.* 108 (2012), p. 226102.
- [30] K. Elder and M. Grant. “Modeling elastic and plastic deformations in nonequilibrium processing using phase field crystals”. In: *Phys. Rev. E*. 70 (2004), p. 051605.
- [31] K. Elder, M. Katakowski, M. Haataja, and M. Grant. “Modeling elasticity in crystal growth”. In: *Phys. Rev. Lett.* 88 (2002), p. 245701.
- [32] K. Elder, N. Provatas, J. Berry, P. Stefanovic, and M. Grant. “Phase-field crystal modeling and classical density functional theory of freezing”. In: *Phys. Rev. E* 75 (2007), p. 064107.
- [33] M. Elsey, S. Esedoglu, and P. Smereka. “Large-scale simulation of normal grain growth via diffusion-generated motion”. In: *Proc. Roy. Soc. A* 467 (2011), p. 381.
- [34] H. Emmerich, H. Lowen, R. Wittkowski, T. Gruhn, G. I. Toth, G. Tegze, and L. Granasy. “Phase-field-crystal models for condensed matter dynamics on atomic length and diffusive time scales: an overview”. In: *Adv. Phys.* 61 (2012), p. 665.
- [35] N. Faghihi, N. Provatas, K. R. Elder, M. Grant, and M. Karttunen. “Phase-field-crystal model for magnetocrystalline interactions in isotropic ferromagnetic solids”. In: *Phys. Rev. E* 88 (2013), p. 032407.
- [36] P. E. Goins, H. A. Murdoch, E. Hernández-Rivera, and M. A. Tschopp. “Effect of magnetic fields on microstructure evolution”. In: *Computational Materials Science* 150.March (2018), pp. 464–474.
- [37] N. Goldenfeld, B. P. Athreya, and J. A. Dantzig. “Renormalization Group Approach to Multiscale Modelling in Materials Science”. In: *J. Stat. Phys.* 125 (2006), pp. 1015–1023.
- [38] N. Goldenfeld, B. P. Athreya, and J. A. Dantzig. “Renormalization group approach to multiscale simulation of polycrystalline materials using the phase field crystal model”. In: *Phys. Rev. E* 72 (2005), p. 020601.

- 
- [39] M. Greenwood, N. Provatas, and J. Rottler. “Free energy functionals for efficient phase field crystal modeling of structural phase transformations”. In: *Phys. Rev. Lett.* 105 (2010), p. 045702.
- [40] O. Guillon, C. Elsässer, O. Gutfleisch, J. Janek, S. Korte-Kerzel, D. Raabe, and C. A. Volkert. “Manipulation of matter by electric and magnetic fields: Toward novel synthesis and processing routes of inorganic materials”. In: *Materials Today* 21.5 (2018), pp. 527–536.
- [41] C. Günster, D. A. Molodov, and G. Gottstein. “Magnetically driven migration of specific planar grain boundaries in Zn bicrystals”. In: *Scr. Mater.* 63 (2010), p. 300.
- [42] J. Han, S. Thomas, and D. Srolovitz. “Grain-boundary kinetics: An unified approach”. In: *Prog. Mater. Sci.* 98 (2018), p. 386.
- [43] V. Heinonen, C. V. Achim, K. R. Elder, S. Buyukdagli, and T. Ala-Nissila. In: *Phys. Rev. E* 89 (2014), p. 032411.
- [44] C. Herring. “Surface tension as a motivation for sintering”. In: *The Physics of Powder Metallurgy*. Ed. by W. Kingston. 1951, p. 143.
- [45] G. Herzer. “Modern soft magnets: Amorphous and nanocrystalline materials”. In: *Acta Mater.* 61 (2013), p. 718.
- [46] P. Hirvonen, M. M. Ervasti, Z. Fan, M. Jalalvand, M. Seymour, S. M. Vaez Allaei, N. Provatas, A. Harju, K. R. Elder, and T. Ala-Nissila. “Multiscale modeling of polycrystalline graphene: A comparison of structure and defect energies of realistic samples from phase field crystal models”. In: *Phys. Rev. B* 94 (2016), p. 035414.
- [47] E. Holm and S. Foiles. “How grain growth stops: A mechanism for grain-growth stagnation in pure materials”. In: *Science* 328 (2010), p. 1138.
- [48] A. Jaatinen, C. Achim, K. Elder, and T. Ala-Nissila. “Thermodynamics of bcc metals in phase-field-crystal models”. In: *Phys. Rev. E* 80 (2009), p. 031602.

- [49] A. Jaatinen and T. Ala-Nissila. “Extended phase diagram of the three-dimensional phase field crystal model”. In: *Journal of Physics Condensed Matter* 22.20 (2010).
- [50] C. Köhler, R. Backofen, and A. Voigt. “Stress Induced Branching of Growing Crystals on Curved Surfaces”. In: *Phys. Rev. Lett.* 116.13 (2016), pp. 1–5.
- [51] H. C. Lei, X. B. Zhu, Y. P. Sun, L. Hu, and W. H. Song. “Effects of magnetic field on grain growth of non-ferromagnetic metals: a Monte Carlo simulation”. In: *Europhys. Lett.* 85.3 (2009), p. 38004.
- [52] Y. Mishin, M. Asta, and J. Li. “Atomistic modeling of interfaces and their impact on microstructure and properties”. In: *Acta Mater.* 58 (2010), p. 1117.
- [53] S. K. Mkhonta, K. R. Elder, and Z.-F. Huang. “Exploring the Complex World of Two-Dimensional Ordering with Three Modes”. In: *Phys. Rev. Lett.* 111 (2013), p. 035501.
- [54] D. A. Molodov, C. Bollmann, P. J. Konijnenberg, L. A. Barrales-Mora, and V. Mohles. “Annealing Texture and Microstructure Evolution in Titanium during Grain Growth in an External Magnetic Field”. In: *Materials Transactions* 48.11 (2007), pp. 2800–2808.
- [55] D. A. Molodov and N. Bozzolo. “Observations on the effect of a magnetic field on the annealing texture and microstructure evolution in zirconium”. In: *Acta Materialia* 58.10 (2010), pp. 3568–3581.
- [56] D. A. Molodov and P. J. Konijnenberg. “Grain boundary and grain structure control through application of a high magnetic field”. In: *Scr. Mater.* 54 (2006), p. 977.
- [57] D. A. Molodov, P. J. Konijnenberg, L. A. Barrales-Mora, and V. Mohles. “Magnetically controlled microstructure evolution in non-ferromagnetic metals”. In: *Journal of Materials Science* 41.23 (2006), pp. 7853–7861.
- [58] W. W. Mullins. “Grain growth of uniform boundaries with scaling”. In: *Acta Materialia* 46.17 (1998), pp. 6219–6226.

- 
- [59] W. Mullins. “Two-dimensional motion of idealized grain boundaries”. In: *J. Appl. Phys.* 27 (1956), p. 900.
- [60] N. Ofori-Opoku, J. Stolle, Z.-F. Huang, and N. Provatas. “Complex order parameter phase-field models derived from structural phase-field-crystal models”. In: *Phys. Rev. B* 88 (2013), p. 104106.
- [61] H. Ohnogi and Y. Shiwa. “Effect of noise on ordering of hexagonal grains in a phase-field-crystal model”. In: *Phys. Rev. E* 84 (2011), p. 051603.
- [62] Y. Oono and Y. Shiwa. “Reductive renormalization of the phase-field crystal equation”. In: *Physical Review E - Statistical, Nonlinear, and Soft Matter Physics* 86.6 (2012), pp. 1–12.
- [63] S. Praetorius, M. Salvalaglio, and A. Voigt. “An efficient numerical framework for the amplitude expansion of the phase-field crystal model”. In: *Modelling and Simulation in Materials Science and Engineering* 27.4 (Apr. 2019), p. 044004.
- [64] S. Praetorius and A. Voigt. In: *SIAM J. Sci. Comput.* 37 (2015), B425.
- [65] R. Ristau, K. Barmak, K. Coffey, and J. Howard. “Grain growth in ultra-thin films of CoPt and FePt”. In: *J. Mater. Res.* 14 (1999), p. 3263.
- [66] S. Rivoirard. “High steady magnetic field processing of functional magnetic materials”. In: *JOM* 65.7 (2013), pp. 901–909.
- [67] M. Salvalaglio, L. Angheluta, Z. Huang, A. Voigt, K. Elder, and J. Viñals. “A coarse-grained phase-field crystal model of plastic motion”. In: *Journal of the Mechanics and Physics of Solids* 137.103856 (2020).
- [68] M. Salvalaglio, A. Voigt, and K. Elder. “Closing the gap between atomic-scale lattice deformations and continuum elasticity”. In: *npj Computational Materials* 5.1 (2019), pp. 1–9.
- [69] M. Salvalaglio, R. Backofen, K. R. Elder, and A. Voigt. “Defects at grain boundaries: A coarse-grained, three-dimensional description by the amplitude expansion of the phase-field crystal model”. In: *Physical Review Materials* 2.5 (2018).

- [70] M. Salvalaglio, R. Backofen, A. Voigt, and K. R. Elder. “Controlling the energy of defects and interfaces in the amplitude expansion of the phase-field crystal model”. In: *Phys. Rev. E* 96.2 (2017), p. 023301.
- [71] R. F. Sekerka. “Equilibrium and growth shapes of crystals: how do they differ and why should we care?”. In: *Cryst. Res. Technol.* 40.4-5 (Apr. 2005), pp. 291–306.
- [72] M. Seymour, F. Sanches, K. Elder, and N. Provatas. “Phase-field crystal approach for modeling the role of microstructure in multiferroic composite materials”. In: *Phys. Rev. B* 92.18 (2015), p. 184109.
- [73] Z. Shan, E. Stach, J. Wieszorek, J. Knapp, D. Follstaadt, and S. Mao. “Grain boundary-mediated plasticity in nanocrystalline nickel”. In: *Science* 305 (2004), p. 654.
- [74] S. Srinivasan, J. Cahn, H. Jonsson, and G. Kalonji. “Excess energy of grain-boundary triple junctions: An atomistic simulation study”. In: *Acta Mater.* 47 (1999), p. 2821.
- [75] S. Tang, R. Backofen, J. Wang, Y. Zhou, A. Voigt, and Y.-M. Yu. “Three-dimensional phase-field crystal modeling of fcc and bcc dendritic crystal growth”. In: *Journal of Crystal Growth* 334.1 (Nov. 2011), pp. 146–152.
- [76] J. E. Taylor and J. W. Cahn. “Linking anisotropic sharp and diffuse surface motion laws via gradient flows”. In: *J. Stat. Phys.* 77.1-2 (1994), pp. 183–197.
- [77] S. van Teeffelen, R. Backofen, A. Voigt, and H. Löwen. “Derivation of the phase-field-crystal model for colloidal solidification”. In: *Phys. Rev. E* 79 (5 2009), p. 051404.
- [78] G. I. Tóth, G. Tegze, T. Pusztai, G. Tóth, and L. Gránásy. “Polymorphism, crystal nucleation and growth in the phase-field crystal model in 2D and 3D”. In: *Journal of Physics Condensed Matter* 22.36 (2010).
- [79] Z. Trautt and Y. Mishin. “Grain boundary migration and grain rotation studied by molecular dynamics”. In: *Acta Mater.* 60 (2012), p. 2407.



- [80] M. Upmanyu, D. Srolovitz, A. Lobkovsky, J. Warren, and W. Carter. “Simultaneous grain boundary migration and grain rotation”. In: *Acta Mater.* 54 (2006), p. 1707.
- [81] M. Upmanyu, D. Srolovitz, L. Shvindlerman, and G. Gottstein. “Molecular dynamics simulation of triple junction migration”. In: *Acta Mater.* 50 (2002), p. 1405.
- [82] S. Vey and A. Voigt. “AMDiS: adaptive multidimensional simulations”. English. In: *Comput. Visual. Sci.* 10.1 (2007), pp. 57–67.
- [83] M. Winning, G. Gottstein, and L. Shvindlerman. “Stress induced grain boundary motion”. In: *Acta Mater.* 49 (2001), p. 211.
- [84] K.-A. Wu and A. Karma. “Phase-field crystal modeling of equilibrium bcc-liquid interfaces”. In: *Phys. Rev. B* 76 (2007), p. 184107.
- [85] K.-A. Wu and P. Voorhees. “Phase field crystal simulations of nanocrystalline grain growth in two dimensions”. In: *Acta Mater.* 60 (2012), p. 407.
- [86] K.-A. Wu, A. Adland, and A. Karma. “Phase-field-crystal model for fcc ordering”. In: *Physical Review E* 81.6 (June 2010), p. 061601.
- [87] A. Yamanaka, K. McReynolds, and P. W. Voorhees. “Phase field crystal simulation of grain boundary motion, grain rotation and dislocation reactions in a BCC bicrystal”. In: *Acta Mater.* 133 (2017), pp. 160–171.
- [88] D.-H. Yeon, Z.-F. Huang, K. Elder, and K. Thornton. “Density-amplitude formulation of the phase-field crystal model for two-phase coexistence in two and three dimensions”. In: *Philos. Mag.* 90.1-4 (2010), pp. 237–263.

## Erklärung des Promovierenden zum Antrag auf Eröffnung des Promotionsverfahrens

1. Die folgende Promotionsordnung in ihrer gültigen Fassung erkenne ich an:

Bereich Mathematik und Naturwissenschaften - Promotionsordnung vom 23.02.2011

2. Die Promotion wurde an folgendem Institut/an folgender Professur durchgeführt:

Institut für Wissenschaftliches Rechnen /  
Professur für Wissenschaftliches Rechnen und Angewandte Mathematik

---

3. Folgende Personen haben die Promotion wissenschaftlich betreut und/oder mich bei der Auswahl und Auswertung des Materials sowie bei der Herstellung des Manuskripts unterstützt:

Prof. Dr. rer. nat. habil. Axel Voigt

---

---

---

---

4. Ich bestätige, dass für meine Person bisher keine früheren, erfolglosen Promotionsverfahren stattgefunden haben. Andernfalls habe ich diesem Antrag eine Erklärung bzw. Nachweise beigelegt, in dem ersichtlich ist, wo, wann, mit welchem Thema und mit welchem Bescheid diese Promotionsversuche stattgefunden haben

5. Ich versichere weiterhin, dass

(a) ich die vorliegende Arbeit mit dem Titel „Influencing the microstructure of polycrystalline materials by magnetic fields - A phase field crystal approach " ohne unzulässige Hilfe Dritter und ohne Benutzung anderer als der angegebenen Hilfsmittel selbst angefertigt habe. Hilfe Dritter wurde nur in wissenschaftlich vertretbarem und prüfungsrechtlich zulässigem Ausmaß in Anspruch genommen. Es sind keine unzulässigen geldwerten Leistungen, weder unmittelbar noch mittelbar, im Zusammenhang mit dem Inhalt der vorliegenden Dissertation an Dritte erfolgt.

(b) die aus fremden Quellen direkt oder indirekt übernommenen Gedanken als solche kenntlich gemacht sind.

(c) ich die vorliegende Arbeit bisher weder im Inland noch im Ausland in gleicher oder ähnlicher Form einer anderen Prüfungsbehörde zum Zwecke einer Promotion oder eines anderen Prüfungsverfahrens vorgelegt habe.

6. Mir ist bekannt, dass die Nichteinhaltung dieser Erklärung oder unrichtige Angaben zum Verfahrensabbruch oder zum nachträglichen Entzug des Dokortitels führen können.

Dresden, 30. September 2021

Ort, Datum



---

Unterschrift Antragsteller/in